BAND MODEL CALCULATIONS OF ATMOSPHERIC TRANSMITTANCE FOR HOT GAS LINE EMISSION SOURCES

Stephen J. Young

Aerospace Corporation

Prepared for:

Space and Missile Systems Organization

31 December 1974

REPORT SAMSO-TR-74-248

Band Model Calculations of Atmospheric Transmittance for Hot Gas Line Emission Sources

S. J. YOUNG
Chemistry and Physics Laboratory
Laboratory Operations
The Aerospace Corporation
El Segundo, Calif. 90245

31 December 1974

Interim Report

Sponsored by
DEFENSE ADVANCED RESEARCH PROJECTS AGENCY
1400 Wilson Boulevard
Arlington, Va. 22209

DARPA Order No. 2843

SPACE AND MISSILE SYSTEMS ORGANIZATION
AIR FORCE SYSTEMS COMMAND
Los Angeles Air Force Station
Los Angeles, Calif. 90045

Approved

Seymour Siegel

S. Siegel, Director
Chemistry and Physics Laboratory
Laboratory Operations

Publication of this report does not constitute Air Force approval of the report's findings or conclusions. It is published only for the exchange and stimulation of ideas.

Gerhard E. Aichinger
Technical Advisor
Contracts Management Office

UNCLASSIFIED

SECURITY CLASSIFICATION OF THIS PAGE (When Data Entered)

REPORT DOCUMENTATION PAGE		READ INSTRUCTIONS BEFORE COMPLETING FORM
1. REPORT NUMBER SAMSO-TR-74-248	2. GOVT ACCESSION NO.	3. RECIPIENT'S CATALOG NUMBER
4. TITLE (and Subtitle) BAND MODEL CALCULATIONS OF ATMOSPHERIC TRANSMITTANCE FOR HOT GAS LINE EMISSION SOURCES		5. TYPE OF REPORT & PERIOD COVERED Interim 6. PERFORMING ORG. REPORT NUMBER TR-0075(5647)-1
7. AUTHOR(s) Stephen J. Young		8. CONTRACT OR GRANT NUMBER(s) F04701-74-C-0075
9. PERFORMING ORGANIZATION NAME AND ADDRESS The Aerospace Corporation El Segundo, Calif. 90245		10. PROGRAM ELEMENT, PROJECT, TASK AREA & WORK UNIT NUMBERS
11. CONTROLLING OFFICE NAME AND ADDRESS Defense Advanced Research Projects Agency 1400 Wilson Boulevard Arlington, Va. 22209		12. REPORT DATE 31 December 1974 13. NUMBER OF PAGES 103
14. MONITORING AGENCY NAME & ADDRESS(if different from Controlling Office) Space and Missile Systems Organization Air Force Systems Command Los Angeles Air Force Station Los Angeles, Calif. 90045		15. SECURITY CLASS. (of this report) Unclassified 15a. DECLASSIFICATION/DOWNGRADING SCHEDULE

16. DISTRIBUTION STATEMENT (of this Report)

Approved for public release; distribution unlimited

17. DISTRIBUTION STATEMENT (of the abstract entered in Block 20, if different from Report)

18. SUPPLEMENTARY NOTES

19. KEY WORDS (Continue on reverse side if necessary and identify by block number)

Band model formulation
Atmospheric transmittance
High temperature emission sources
Exhaust plume emission

20. ABSTRACT (Continue on reverse side if necessary and identify by block number)

A discussion and application of band model techniques to the calculation of the effective transmittance of the atmosphere to hot gas line emission sources is presented. These types of calculations are relevant to the analysis of satellite surveillance systems and field measurements data obtained from missile and aircraft sightings in which the primary target radiation is hot gas plume infrared emission. The band model formulation designed for these calculations accounts for line correlation effects that

DD FORM 1473 (FACSIMILE)

PRICES SUBJECT TO CHANGE

UNCLASSIFIED

SECURITY CLASSIFICATION OF THIS PAGE (When Data Entered)

19. KEY WORDS (Continued)

20. ABSTRACT (Continued)

occur when the primary radiating species of the plume source and the primary absorbing species of the atmosphere are the same species (i.e., H_2O and CO_2). This correlation effect is handled correctly by treating the entire line of sight from the sensor, through the intervening atmosphere and the hot source region of the plume, as a single highly inhomogeneous and nonisothermal optical path. A detailed investigation is made of the ability of the standard Curtis-Godson and the newly formulated Lindquist-Simmons approximations to handle correctly the high degree of inhomogeneity of this optical path, and the conditions under which the Curtis-Godson approximation is likely to fail are determined. For these conditions, the Lindquist-Simmons approximation must be used, and procedures for the efficient application of this approximation are derived.

A discussion of band model parameters used for calculations within the band model is presented. The General Dynamics high-temperature band model parameters and parameters derived from the Air Force Cambridge Research Laboratories (AFCRL) line data compilation for atmospheric absorbing species are compared and analyzed to determine the spectral and temperature regions for which they are most applicable.

A brief description is given of the computer code (ATLES) that handles the band model computations. In addition, a detailed analysis is made of the radiative transfer properties of two atmospheric paths. The slant path originating at an altitude of 20 km and extending to space at a 75-deg zenith angle is typical of viewing geometries for satellite surveillance systems. The 100-km-long horizontal path at 20-km altitude is representative of the viewing geometry used in on-going field measurements programs employing sensor-equipped aircraft. An equivalent isothermal H_2O/CO_2 cylindrical plume model is used as the 20-km altitude target. Results for this source over the two atmospheric paths indicate that the effective transmittance of the atmosphere to hot gas emission sources may be several times smaller than transmittance values that are calculated ignoring the line correlation effects.

CONTENTS

TABLES

FIGURES

FIGURES (Continued)

I. INTRODUCTION

Consideration of the infrared transmittance of the atmosphere is of fundamental importance to the analysis of the spectral characteristics of missile and aircraft plumes viewed through long atmospheric paths. For example, in order to design surveillance system sensors, a priori knowledge is required of the expected radiance that would be presented to such sensors. Similarly, methods are required for correcting the apparent radiance measured by operating systems to arrive at the unattenuated target signals. The solution of both of these problems hinges on the ability to compute appropriate atmospheric transmittance factors.

Quasi-empirical methods developed for computing atmospheric attenuation within the framework of band model approximations have been used for a number of years. An extensive review of many of these models is given by Anding.[1] Although the exact procedure used in developing these various models differs from model to model, the underlying approach is the same. Basically, a transmittance function $\bar{\tau}[\bar{k}(\nu), u]$ is determined for a particular atmospheric absorbing species from laboratory data measured for homogeneous absorbing paths of this same species. The variable u is a measure of the optical depth of the path, and $\bar{k}(\nu)$ is a measure of the mean absorption in an interval $\Delta\nu$ about the spectral position ν. Either a theoretically based functional dependence of $\bar{\tau}$ on u and $\bar{k}(\nu)$ is assumed and $\bar{k}(\nu)$ is adjusted for a best fit with the laboratory data within each $\Delta\nu$ region, or the dependence actually displayed by the data is determined and tabulated. With either approach, the end result is a transmittance model, which can reasonably predict the transmittance spectrum that would be experimentally

[1] D. Anding, Band-Model Methods for Computing Atmospheric Slant-Path Molecular Absorption, 7142-21-T, Willow Run Laboratories, Ann Arbor, Mich. (February 1967)(reprinted January 1969).

obtained for homogeneous paths of arbitrary optical thickness. In order to apply these models to general atmospheric slant paths, a means is required of reducing the nonhomogeneous slant path absorbing properties to those of an equivalent homogeneous path. This reduction is usually performed by an application of the Curtis-Godson approximation. The resulting equivalent homogeneous properties are then inserted into the band model to yield the transmittance of the atmospheric path.

Anding[1] has made a detailed comparison of the predictions of the most prominent of these band models and the limited amount of actual field measurements that exist for atmospheric slant paths. In general, when appropriate band models are chosen with regard to specific species and spectral region, a reasonably accurate representation of atmospheric transmittance can be obtained.

Despite the reasonable accuracy of these models, however, two severe limitations preclude their application to the present problem. First, the models are applicable only for optical paths over which the temperature is near atmospheric temperatures, and second, they are appropriate only for predicting the attenuation of continuum radiation (e.g., blackbody radiation). For a great number of targets of interest, the source radiation is not continuum radiation, but is, in fact, highly structured (spectrally speaking) molecular band emission. The temperature limitation imposed on existing models prevents their application to the computation of transmission/absorption properties within the hot gaseous plumes of a missile or jet aircraft. Moreover, the limitation to continuum radiation sources prevents the use of these models in computing the transmission of radiation emitted from a particular species in the plume when this same species is present as an atmospheric absorber (e.g., H_2O). The high degree of correlation between the line positions of the hot gaseous emission spectrum and the cool atmospheric absorption spectrum results in a greater amount of absorption than would be effected for continuum source radiation.

The inapplicability of existing atmospheric transmittance models for computing hot gaseous radiation characteristics is not a serious problem since other transmittance models explicitly designed for hot combustion gas calculations have been formulated.[2] However, the inapplicability of current atmospheric transmittance models to calculations involving non-continuum source radiation is not so easily remedied.

One of the fundamental objectives of the present work is to assess the degree of error inherent in the use of present atmospheric transmittance calculations when they are applied to the problem of deattenuating radiance data obtained for targets whose primary radiation is due to hot gas emission. At present, this work is concerned exclusively with missile and jet aircraft plumes containing hot CO_2 and H_2O as the only infrared-active species. Similarly, the only atmospheric attenuating species considered are CO_2 and H_2O. No consideration is given to particulate emission within the plume or particulate extinction (absorption or scattering) in the atmosphere. The primary combustion products for hydrocarbon-fueled missiles and aircraft are H_2O and CO_2, and these are the radiating species for which the line correlation effect would render the most inaccurate calculations using present transmittance models.

The line correlation effect will be most significant for the attenuation of hot H_2O emission by cool atmospheric H_2O absorption and for the attenuation of hot CO_2 emission by cool atmospheric CO_2 absorption. Since the line positions between H_2O and CO_2 are uncorrelated, however, this effect is not present for the attenuation of hot H_2O emission by atmospheric CO_2 absorption or vice versa. For these latter conditions, the atmospheric transmittance computed using present band models would, in principle, be correct. Similarly, present band models would be applicable for calculating the atmospheric attenuation of radiation emitted from particulate matter in

[2] C. B. Ludwig, W. Malkmus, J. E. Reardon, and J. A. L. Thompson, Handbook of Infrared Radiation from Combustion Gases, NASA SP-3080, ed. R. Goulard and J. A. L. Thompson (1973).

plumes (e.g., carbon) or from engine hot parts since this radiation would be continuum in nature. It should be emphasized that this line correlation effect exists only within the concept of a band model formulation, i.e., for the case where the average transmittance effects in a nonzero spectral region $\Delta\nu$ containing many individual vibration-rotation lines are considered. On a strictly monochromatic basis, the transmittance of the atmosphere is a function of the atmospheric properties alone and is not influenced by the source spectral characteristics.

The present work is concerned with the design and application of a band modeling technique that includes the effects of line correlation between the emitting and absorbing species. This is accomplished by treating the entire line of sight extending from the sensor position through the intervening atmosphere to the far boundary of the hot gas emission source as a single radiating/absorbing path. Thus, the atmospheric and source paths are treated in a coupled manner. The effective transmittance of the atmosphere to the line emission source is derived by dividing the radiance computed for this total path by the radiance computed for the source portion of the path alone. This procedure will always yield a transmittance factor smaller than the atmospheric transmittance computed for a continuum source. The penalty for treating the problem in this manner is the generation of a highly inhomogeneous line of sight. Although the atmospheric path portion of the total path is itself inhomogeneous, the degree of inhomogeneity can be adequately handled within the Curtis-Godson approximation. Coupling a hot gas emission source to the end of the atmospheric path, however, can generate a high degree of inhomogeneity. The principal region of discontinuity occurs at the boundary of the atmospheric and source portions of the path. As will be shown in this discussion, the degree of inhomogeneity generated in this region can easily exceed the limitations of the Curtis-Godson approximation. To circumvent the failings of the Curtis-Godson

approximation in these areas, a recently developed formulation,[3] the Lindquist-Simmons approximation, is invoked. Results derived using the latter approximation show significant improvement over those obtained using the Curtis-Godson approximation.

Section II of this report is devoted to the formulation of the band model used in the present work and to a detailed investigation of both the Curtis-Godson and Lindquist-Simmons approximations. A discussion of the band model parameters used within the model is presented in Section III, and a brief account of the computer code ATLES (Atmospheric Transmittance to Line Emission Sources) used to perform the transmittance calculations is given in Section IV. Results obtained for hypothetical missile plume sources for two typical viewing geometries are presented in Section V. A summary and recommendations for future work are given in Section VI.

[3] G. H. Lindquist and F. S. Simmons, "A Band Model Formulation for Very Nonuniform Paths," J. Quant. Spectrosc. Radiat. Trans. 12, 807 (1972).

II. BAND MODEL FORMULATION

A. RADIANCE EQUATIONS

The exact solution for the radiance at position s = 0 of a general line of sight extending to s = S at a specific wave number and for a single optically active gas is

$$L(\nu) = \int_0^S L^*(\nu, s)\, k(\nu, s)\, c(s)\, p(s) \left[e^{-\int_0^s k(\nu, s')\, c(s')\, p(s')\, ds'} \right] ds \qquad (1)$$

where $L^*(\nu, s)$ is the Planck radiation function, $k(\nu, s)$ is the spectral absorption coefficient of the active gas, $p(s)$ is the total gas pressure, $c(s)$ is the mole fraction of the active gas, s is the geometric path length variable, and S is the total geometric path length. This formulation of the equation assumes that there is no source of radiation (background) beyond s = S. The variables entering into this equation are written explicitly as functions of the path variable s to emphasize the fact that they may change with path position.

The monochromatic treatment of radiance with the use of Eq. (1) for an entire vibration-rotation band of an active molecule might require radiance calculations for several thousand individual lines. In addition, a number of calculations would be required over the profile of each line to account for its spectral shape. If high spectral resolution results are not required, a considerable reduction in calculation effort can be effected by considering the average radiation effects in a small interval $\Delta\nu$ containing a band of several tens or hundreds of lines.

The average radiance in a spectral interval $\Delta\nu$ centered around ν is

$$\overline{L}(\nu) = \frac{1}{\Delta\nu} \int_{\Delta\nu} L(\nu')\, d\nu' \qquad (2)$$

If $\Delta\nu$ is small enough so that $L^*(\nu, s)$ is sensibly constant over $\Delta\nu$, Eqs. (1) and (2) can be made to yield

$$\bar{L}(\nu) = -\int_0^S L^*(\nu, s) \frac{d\bar{\tau}(\nu, s)}{ds} ds \tag{3}$$

where $\bar{\tau}(\nu, s)$ is the average transmittance in $\Delta\nu$

$$\bar{\tau}(\nu, s) = \frac{1}{\Delta\nu} \int_{\Delta\nu} \tau(\nu', s) \, d\nu' \tag{4}$$

and $\tau(\nu, s)$ is the spectral transmittance

$$\tau(\nu, s) = e^{-\int_0^s k(\nu, s') c(s') p(s') \, ds'} \tag{5}$$

Equation (3) is the basis of radiance calculations using band model approximations. Rather than attempting to characterize the radiation transfer for all wave numbers of interest through the use of Eq. (1), band model approximations attempt to characterize the average transfer effects in a small interval $\Delta\nu$. The main effort in band modeling is the characterization of the transmittance term $\bar{\tau}(\nu, s)$ entering into Eq. (3) without, of course, resorting to its calculation via Eqs. (4) and (5).

The generalization of Eq. (3) to the case of several active species is made by writing the average total transmittance $\bar{\tau}$ as a product of the individual average transmittances of each species

$$\bar{\tau}(\nu, s) = \prod_{i=1}^{m} \bar{\tau}_i(\nu, s) \tag{6}$$

where m is the number of species. This relation requires the assumption that there exists a complete lack of correlation between the line strengths and, particularly, the line positions of any two species in the interval $\Delta\nu$. This lack of correlation has been demonstrated to be true for H_2O and CO_2.[4]

Substitution of Eq. (6) into Eq. (3) yields the following form of the radiance equation used in the present work:

$$\bar{L}(\nu) = -\int_0^S L^*(\nu, s)\, \bar{\tau}(\nu, s) \sum_{i=1}^{m} \frac{1}{\bar{\tau}_i(\nu, s)} \frac{d\bar{\tau}_i(\nu, s)}{ds}\, ds \qquad (7)$$

To compute the transmittance of an atmospheric path to a line-emission source, radiance calculations using Eq. (7) are made over two paths. The first path is the source path alone, and the second path is the entire line of sight consisting of the atmosphere and the source path combined. Calculation over the first path yields the radiance of the source at the source boundary, while calculation over the second path yields the total radiance at the sensor (s = 0) position, taking into account the absorption/emission effects presented by the intervening atmosphere. The true transmittance of the atmosphere to the source is computed by dividing the total path radiance by the source path radiance. This true transmittance can then be compared to the transmittance $\bar{\tau}$ given by Eq. (6). The latter transmittance is the normally computed atmospheric transmittance and is appropriate to a source that emits continuum radiation (e.g., a blackbody) with approximately constant intensity across $\Delta\nu$. The effect of a high degree of correlation between the line positions of the emitting source and those of the absorbing atmosphere results in the true transmittance being less than the transmittance to a constant continuum source.

---

[4] R. M. Goody, Atmospheric Radiation, I: Theoretical Basis, Clarendon Press, Oxford (1964).

B. BAND MODEL

Equation (7) is the relation used to compute radiance in the band model approximation. The aim of the band model proper is to characterize the average transmittance $\bar{\tau}$ to be used in this relation. The present work is carried out within the framework of the statistical band model. In this model, the arrangement of lines (i.e., the line positions) within a spectral interval is assumed to be completely random. Within this approximation, the average transmittance for a single species is given by

$$\bar{\tau} = \exp\left(-\frac{\overline{W}}{\delta}\right) = \exp\left[-\frac{1}{N\delta}\sum_{i=1}^{N} W(i)\right] \tag{8}$$

where $\overline{W}$ is the mean equivalent width for all the lines in the spectral region $\Delta\nu$, δ is the mean line spacing in $\Delta\nu$, and N is the number of lines in $\Delta\nu$. To provide a working model when the individual W(i) are not all known, some analytic intensity distribution is generally assumed and applied to Eq. (8). Commonly used distribution functions include: (1) a constant line intensity distribution wherein all lines in $\Delta\nu$ are assumed to have the same strength, (2) an exponential line intensity distribution, and (3) an inverse line-strength distribution function. For reasons to be discussed later, the present work has been carried out for a random array of pressure-broadened Lorentzian lines of constant line intensity. When this distribution is assumed, the mean transmittance for a random array of pressure-broadened Lorentzian lines is given by

$$\bar{\tau} = e^{-\beta f(x)} \tag{9}$$

where f(x) is the Ladenburg-Reiche function, x is the dimensionless optical depth parameter, and β is the mean line width/spacing band model parameter.

A discussion of x and β is presented in paragraph II.C. An equivalent way to write Eq. (9) is

$$\bar{\tau} = e^{\bar{\tau}'} - 1 \tag{10}$$

where

$$\bar{\tau}' = 1 - \beta f(x) \tag{11}$$

The term $\bar{\tau}'$ is interpreted to represent the mean transmittance in $\Delta\nu$ for a band of randomly arranged but well-isolated lines. The functional form of Eq. (10) then allows one to write the transmittance for general overlapping conditions in terms of $\bar{\tau}'$. Note that, in this interpretation, it is entirely possible for $\bar{\tau}'$ to be a negative number. This occurs when the condition of nonoverlapping of lines no longer holds, and, under these conditions, it is best not to think of $\bar{\tau}'$ as a transmittance, but simply as an intermediate function needed to compute $\bar{\tau}$. Note also that negative values of $\bar{\tau}'$ are, in fact, required to allow $\bar{\tau}$ to assume values of less than $e^{-1} \simeq 0.368$.

In addition to $\bar{\tau}$, the derivative $d\bar{\tau}/ds$ is required in the application of Eq. (7). From Eqs. (10 and (11),

$$\frac{d\bar{\tau}}{ds} = \bar{\tau} \frac{d\bar{\tau}'}{ds} \tag{12}$$

$$\frac{d\bar{\tau}'}{ds} = -\beta \frac{df(x)}{dx} \frac{dx}{ds} - f(x) \frac{d\beta}{ds} \tag{13}$$

C. INHOMOGENEOUS PATH CONSIDERATIONS

For a homogeneous path, the dimensionless optical depth parameter x is given by

$$x(s) = \frac{\bar{k}u}{\beta} \tag{14}$$

where $u = cps$ is the optical depth of the path, and $\bar{k}$ and β are the basic band model parameters. The term $\bar{k}$ is the mean absorption coefficient for the interval $\Delta\nu$, and β is a measure of the ratio of the mean line width to the mean line spacing in $\Delta\nu$

$$\beta = 2\pi \frac{\bar{\gamma}}{\delta} \tag{15}$$

For an inhomogeneous path, appropriate path-averaged values for $\bar{k}$ (or x) and β must be used. In the present work, two methods of accounting for path inhomogeneities are used: In addition to the standard Curtis-Godson approximation, the recently developed Lindquist-Simmons approximation is considered.[3] The latter approximation was developed to correct some of the failings of the Curtis-Godson approximation when applied to highly inhomogeneous paths. In either of these approximations, the following path-averaged quantities are used for x and β:

$$x_e(s) = \frac{1}{\beta_e(s)} \int_0^s \bar{k}(s')\, c(s')\, p(s')\, ds' \tag{16}$$

$$\beta_e(s) = \int_0^s \bar{k}(s')\, c(s')\, p(s')\, \beta(s')\, ds \Big/ \int_0^s \bar{k}(s')\, c(s')\, p(s')\, ds' \tag{17}$$

In the Curtis-Godson approximation, these path-averaged values are used directly for x and β in Eqs. (11) and (13) to give the nonoverlapping transmittance and transmittance derivative

$$\bar{\tau}' = 1 - \beta_e\, f(x_e) \tag{18}$$

$$\frac{d\bar{\tau}'}{ds} = -\beta_e \frac{df(x_e)}{dx_e} \frac{dx_e}{ds} - f(x_e) \frac{d\beta_e}{ds} \tag{19}$$

Differentiation of Eqs. (16) and (17) allows Eq. (19) to be written in the convenient form

$$\frac{d\bar{\tau}'}{ds} = -\bar{k}\, cp\, y(x_e, \rho) \tag{20}$$

where

$$y(x, \rho) = (2 - \rho) \frac{df(x)}{dx} + (\rho - 1) \frac{f(x)}{x} \tag{21}$$

and where $\rho = \beta/\beta_e$ is the ratio of the local β to the path-averaged value up to that point.

In effect, the Curtis-Godson approximation simply replaces the inhomogeneous path by an equivalent homogeneous path whose x and β variables are the path-averaged variables x_e and β_e. The Lindquist-Simmons approximation also uses the path-averaged variables x_e and β_e, but in a lesser degree of approximation. Rather than making approximations in the expression for the transmittance, the Lindquist-Simmons approach is to make approximations in the expression for the transmittance derivative. The rationale for this approach is that the radiance equations, i.e., Eq. (3) or (7), are formulated basically in terms of the transmittance derivative rather than the transmittance itself. Thus, an approximation to the former should be inherently more accurate than an approximation to the latter. For a single, isolated Lorentzian line, the transmittance derivative is

$$\frac{d\tau}{ds} = -\frac{1}{\pi} \int_{-\infty}^{\infty} \frac{S(s)\, \gamma(s)}{\gamma^2(s) + \Delta\nu^2} c(s)\, p(s) \exp\left[-\frac{1}{\pi} \int_0^s \frac{S(s')\, \gamma(s')}{\gamma^2(s') + \Delta\nu^2} c(s')\, p(s')\, ds' \right] d(\Delta\nu) \tag{22}$$

where S and γ are the line strength and width, respectively. For a band of nonoverlapping Lorentzian lines of equal strength and width, the corresponding band model average transmittance can be written

$$\frac{d\bar{\tau}'}{ds} = -\frac{1}{\pi}\int_{-\infty}^{\infty} \frac{\bar{k}(s)\,\beta(s)}{\beta^2(s) + Z^2}\, c(s)\, p(s) \exp\left[-\frac{1}{\pi}\int_0^s \frac{\bar{k}(s')\,\beta(s')}{\beta^2(s') + Z^2}\, c(s')\, p(s')\, ds'\right] dZ \tag{23}$$

where $Z = 2\pi\Delta\nu/\delta$. The necessity of assuming a band of equal-strength lines to arrive at Eq. (23) is one of the reasons that the constant line intensity distribution form of the statistical band model has been assumed throughout. The need for this restriction will be the subject of future work. In the Curtis-Godson approximation, the path-dependent parameter $\beta(s)$ occurring in Eq. (23) is replaced by the path-averaged value β_e. This has the effect of performing a separation between the path integration and spectral integration operations and results, after performing the spectral integration, in Eqs. (18) and (19). In the Lindquist-Simmons approximation, the replacement of β by β_e is made only in the exponential term of Eq. (23), which can then be simplified to

$$\frac{d\bar{\tau}'}{ds} = -\bar{k}\, cp\, y(x_e, \rho) \tag{24}$$

where

$$y(x, \rho) = \frac{2\rho}{\pi}\int_0^{\pi} \frac{e^{-x(1 + \cos\theta)}}{(\rho^2 + 1) + (\rho^2 - 1)\cos\theta}\, d\theta \tag{25}$$

where, $\theta = 2\tan^{-1}(2\pi\Delta\nu/\beta_e\delta)$ and, again, $\rho = \beta/\beta_e$. Thus, a complete separation of spatial and spectral integrations is not effected in the Lindquist-Simmons approximation. A detailed analysis of the function y is given in

paragraph II. D. Note also that, in the Lindquist-Simmons approximation, no analytical solution is given for $\bar{\tau}$; and, hence, this function must be integrated numerically after $d\bar{\tau}'/ds$ is evaluated along the path, i.e.,

$$\bar{\tau}'(s) = 1 - \int_0^s \frac{d\bar{\tau}'(s)}{ds}\, ds \tag{26}$$

A summary of formulas required for implementing the band model calculations in both the Curtis-Godson and Lindquist-Simmons approximations is given in Table 1. The Ladenburg-Reiche function f(x) is approximated by

$$f(x) = \frac{x}{\left[1 + \left(\frac{\pi x}{2}\right)^{\alpha}\right]^{1/2\alpha}} \tag{27}$$

$$\frac{df(x)}{dx} = \left[1 + \frac{1}{2}\left(\frac{\pi x}{2}\right)^{\alpha}\right]\left[1 + \left(\frac{\pi x}{2}\right)\right]^{-(1 + 1/2\alpha)} \tag{28}$$

where $\alpha = 5/4$. This approximation has been stated to be accurate to less than 1 percent for all x.[5]

The Planck radiation function used in Eq. (7) is

$$L^*(\nu, s) = 1.192 \times 10^{-12} \nu^3 \left[e^{1.439\nu/T(s)} - 1\right]^{-1} \tag{29}$$

and gives $L^*(\nu, s)$ in units of $W/cm^2 sr\ cm^{-1}$ for ν in units of cm^{-1} and T(s) in units of °K.

---

[5] A. Goldman, "On Simple Approximations to the Equivalent Width of a Lorentz Line," J. Quant. Spectrosc. Radiat. Trans. 8, 829 (1968).

Table 1. Summary of Band Model Computation Formulas

Radiance

$$\bar{L}_\nu = -\int_0^S L_\nu^*(s)\,\frac{d\bar{\tau}(s)}{ds}\,ds$$

Total Transmittance

$$\bar{\tau}(s) = \prod_{i=1}^{m} \bar{\tau}_i(s)$$

$$\frac{d\bar{\tau}(s)}{ds} = \bar{\tau}(s) \sum_{i=1}^{m} \frac{1}{\bar{\tau}_i(s)}\,\frac{d\bar{\tau}_i(s)}{ds}$$

Individual Species Transmittance

$$\bar{\tau}_i(s) = \exp[\bar{\tau}_i'(s) - 1]$$

$$\frac{d\bar{\tau}_i(s)}{ds} = \bar{\tau}_i(s)\,\frac{d\bar{\tau}_i'(s)}{ds}$$

Nonoverlapping Band Model Transmittance

$$\frac{d\bar{\tau}_i'(s)}{ds} = -\bar{k}_i(s)\,c_i(s)\,p(s)\,y\left[x_e^i(s),\ \rho_i(s)\right]$$

$$\bar{\tau}_i'(s) = 1 - \beta_e^i(s)\,f\left[x_e^i(s)\right] \quad \text{. . . . . Curtis-Godson}$$

$$\bar{\tau}_i'(s) = 1 - \int_0^s \frac{d\bar{\tau}_i'(s)}{ds}\,ds \quad \text{. . . . Lindquis-Simmons}$$

Table 1. Summary of Band Model Computation Formulas (Continued)

Path Averages

$$x_e^i(s) = \frac{1}{\beta_e^i(s)} \int_0^s \bar{k}_i(s')\, c_i(s')\, p(s')\, ds'$$

$$\beta_e^i(s) = \int_0^s \bar{k}_i(s)\, \beta_i(s')\, c_i(s')\, p(s')\, ds' \Big/ \int_0^s \bar{k}_i(s')\, c_i(s')\, p(s')\, ds'$$

$$\rho_i(s) = \beta_i(s)/\beta_e^i(s)$$

y-Function

$$y(x,\rho) = (2-\rho)\frac{df(x)}{dx} + (\rho - 1)\frac{f(x)}{x} \quad \text{. . . . Curtis-Godson}$$

$$y(x,\rho) = \frac{2\rho}{\pi}\int_0^{\pi} \frac{e^{-x(1+\cos\theta)}}{(\rho^2+1) + (\rho^2-1)\cos\theta}\, d\theta \quad \text{. . . . Lindquist-Simmons}$$

Ladenburg-Reiche Function

$$f(x) = \frac{x}{\left[1 + \left(\frac{\pi x}{2}\right)^{\alpha}\right]^{1/2\alpha}}$$

$$\frac{df(x)}{dx} = \left[1 + \frac{1}{2}\left(\frac{\pi x}{2}\right)^{\alpha}\right]\left[1 + \left(\frac{\pi x}{2}\right)^{\alpha}\right]^{-(1+1/2\alpha)}$$

$$\alpha = 5/4$$

Planck Function

$$L^*(\nu, T) = 1.192 \times 10^{-12}\nu^3\left[e^{1.439\nu/T} - 1\right]^{-1}$$

D. ANALYSIS OF $y(x, \rho)$

The essential difference between the standard Curtis-Godson (CG) and Lindquist-Simmons (LS) approximations is the formulation for the function y. A greater degree of approximation characterizes the CG than the LS approximation and allows for a complete separation of the spatial and spectral variables of integration. The LS approximation does not yield a complete separation of spatial and spectral variables and, thus, requires a new spectral integration for each new spatial coordinate considered along the inhomogeneous path. An analysis of the function y has been made for both the CG and LS approximations with the intent of showing under what conditions the CG approximation can be expected to fail, how the LS approximation succeeds under these same conditions, and how the calculation of y in the LS approximation is effected in practice.

The function y is dependent on the two parameters x and ρ (the subscript on x_e is suppressed). The term x is a measure of the optical depth from the beginning of a line of sight to a point along the line of sight, and ρ is the ratio of the local band model parameter β to the average value of β over the path up to that point. The parameter x is zero at the beginning (sensor position) of any optical line of sight and generally becomes larger as the distance along the line of sight increases. There are conditions, however, under which x can decrease as the distance into the optical path increases. If the defining expression for x(s) in Eq. (16) is differentiated with respect to the path variable s, it can be derived that

$$\frac{dx(s)}{ds} = \frac{\overline{k}(s)\, c(s)\, p(s)}{\beta_e(s)} [2 - \rho(s)] \tag{30}$$

Thus, at any point where ρ is greater than 2, dx(s)/ds is negative and x(s) decreases with increasing distance into the path. The largest value of x encountered in any calculation to date has been ~2000.

The parameter ρ has the value of unity at the beginning of any line of sight, and the variation of ρ along the line of sight then depends on the path type and the strength of the inhomogeneities along the path. For atmospheric paths, two conditions prevail. If a line of sight originates at a high altitude and progresses deeper into the atmosphere, ρ increases gradually and generally approaches a final value of ~2. However, if a line of sight originates low in the atmosphere and progresses upward to low pressure regions, ρ may obtain values as small as 10^{-7}. For a line of sight that proceeds from a cool region into a hot region, β may increase substantially near the boundary of the region and result in a local increase in ρ up to values of 100 or more. The largest value encountered in calculations to date has been ~200. Thus, it is evident that there is a large range over which the parameters x and ρ can vary and this range has important implications in the calculation of y, particularly within the LS approximation.

Regardless of the extent of the variation of x and ρ, however, certain physical restraints can be placed on the functional form of a realistic y-function. These restraints are: $y \to 1$ as $x \to 0$ (weak line or linear limit); $dy/dx \to 0$ as $x \to 0$; $y \sim x^{-1/2}$ as $x \to \infty$ (strong line or square root limit); $y \to 1$ as $\rho \to \infty$; and y remains less than or equal to unity for all x and ρ.

1. CURTIS-GODSON APPROXIMATION

In the CG approximation, $y(x, \rho)$ is given by Eq. (21) where f(x) is approximated by Eq. (27). From these two equations,

$$y(x, \rho) \simeq \left[1 + \frac{\rho}{2}\left(\frac{\pi x}{2}\right)^{\alpha}\right]\left[1 + \left(\frac{\pi x}{2}\right)^{\alpha}\right]^{-(1 + 1/2\alpha)} \tag{31}$$

Differentiation of this function with respect to x and solving for the extrema yield the conclusion that y will have an extremum (maximum) for $x \geq 0$ whenever $\rho \geq 2 + 1/\alpha = 2.80$. The position of the maximum is

$$x = \frac{2}{\pi}\left\{\frac{4\alpha}{\rho}\left[\frac{\rho}{2} - \left(1 + \frac{1}{2\alpha}\right)\right]\right\}^{1/\alpha} \tag{32}$$

and the value of y at this maximum is

$$y_{max} = \frac{\alpha(\rho - 2)}{\left\{1 + \frac{2}{\rho}\left[\alpha(\rho - 2) - 1\right]\right\}^{-1 + 1/2\alpha}} \tag{33}$$

Since $y(x = 0)$ is unity, y must therefore become greater than unity for $x > 0$ whenever $\rho > 2 + 1/\alpha$. The position at which y again becomes less than unity can be obtained by solving the equation $y(x, \rho) = 1$. One solution is obviously $x = 0$, and the other solution is contained in the expression

$$\left(1 + \frac{\rho\pi x}{4}\right) = \left(1 + \frac{\pi x}{2}\right)^{3/2} \tag{34}$$

For $\rho \gtrsim 10$, this condition requires $x \gtrsim \rho^2/2\pi$ before y is again less than unity. Some curves for $y(x, \rho)$ in the Curtis-Godson approximation are shown in Fig. 1.

The failing of the CG approximation can thus be seen to occur primarily under conditions where a strong inhomogeneity gives rise to a large increase in β (large ρ) near the beginning of a line of sight (small or medium x). This is the condition that obtains, for example, for a calculation on a line of sight originating on the boundary of a rarified missile plume or flame. If no large increase in β occurs until far into the path where x is large, no inaccuracy is immediately apparent in the CG approximation. However, under these conditions, the region of large inhomogeneity contributes little to the line-of-sight radiance because of the small transmittance of the previous portions of the path. The result of Eq. (30) is important here also. If ρ is large enough to make the CG approximation inaccurate, it is also large

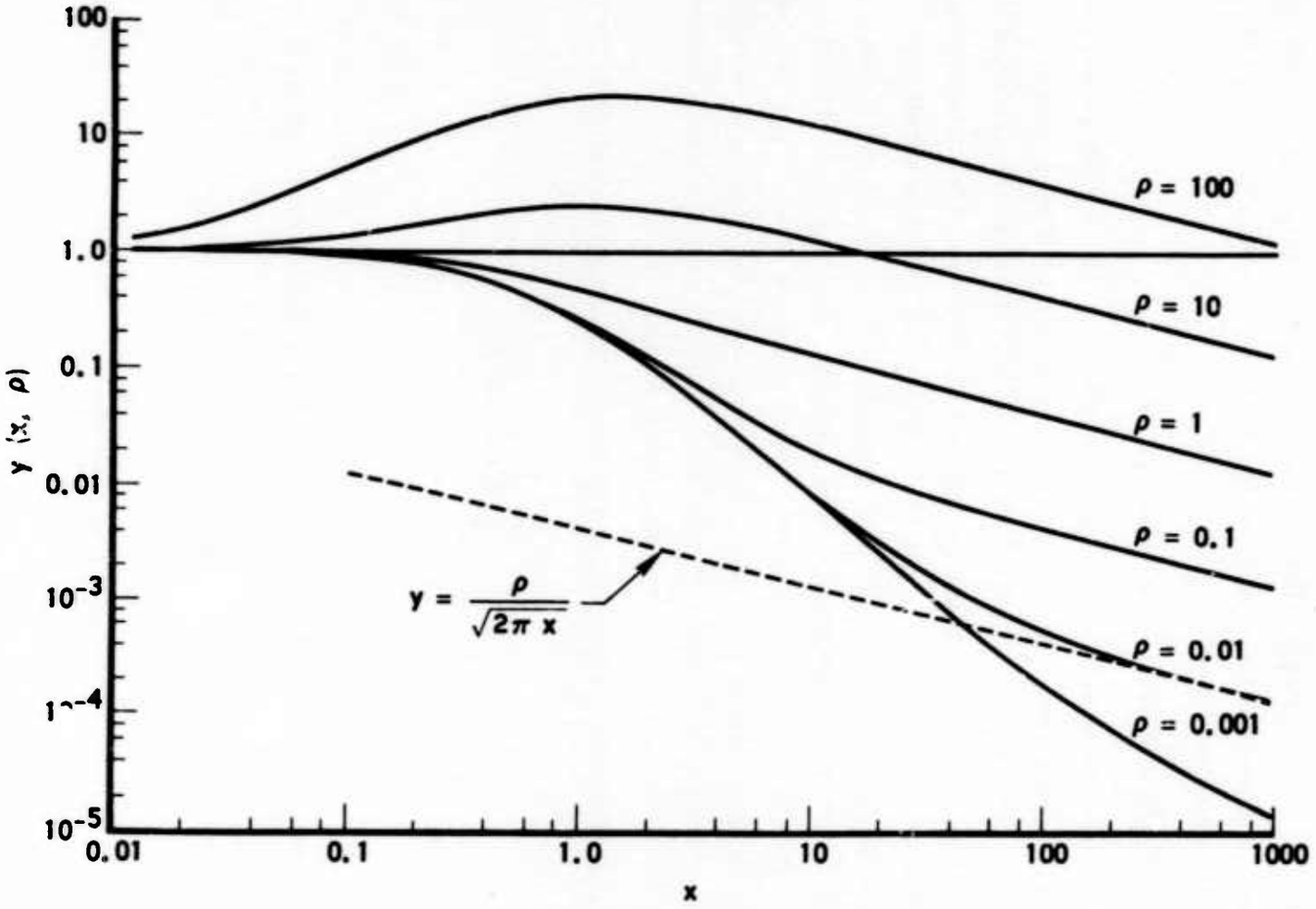

Fig. 1. The Function y(x, ρ) for the Curtis-Godson Approximation

enough to make dx/ds negative. Thus, even with increasing depth along the geometric path, x does not increase and the path calculations become trapped in the region of maximum error.

2. LINDQUIST-SIMMONS APPROXIMATION

A distinct advantage of the CG approximation is that y is expressible in terms of f(x) and the latter function can be approximated by a rather simple, but quite accurate, analytical expression. The y-function in the LS approximation, however, cannot be written so simply. The calculation of y in the LS approximation by a new numerical spectral integration for each path interval position is highly inefficient if accuracy of better than approximately 1 percent is required. The approach to the use of the LS approximation has been to compute y numerically over a grid of x, ρ values, and then to perform a two-dimensional, log-log, second-order interpolation on the table to obtain y at specific x, ρ points. In addition, analytic approximations have been found for certain conditions of x and ρ.

The exact expression for y(x, ρ) in the LS approximation is

$$y(x,\rho) = \frac{2\rho}{\pi}\int_0^{\pi} \frac{e^{-x(1+\cos\theta)}}{(1+\rho^2)+(1-\rho^2)\cos\theta}\,d\theta \qquad (35)$$

No analytic solution for this integral has been discovered. An analysis of the integrand of this integral shows that, in addition to the extrema that always occur at θ = 0 and θ = π, the integrand has an extremum between θ = 0 and θ = π for ρ < 1 only and then only for

$$\frac{1-\rho^2}{2} < x < \frac{1-\rho^2}{2\rho^2} \qquad (36)$$

This extremum is a minimum and only one extremum exists. These conditions delineate the three cases for the positive x, ρ quadrant shown in Fig. 2(a). The form of the integrand between θ = 0 and θ = π for each case is shown in Fig. 2(b). Note that the condition of very large x in cases I and III leads to the formation of a very sharply peaked function around θ = π, while the condition of very small ρ in cases II and III leads to a very sharply peaked function around θ = 0. These conditions result in the ability to find analytic asymptotic solutions for the extreme conditions of these cases. The asymptotic solution for very large x has been obtained using a standard analysis procedure, which results in the correct square root form

$$y(x, \rho) \rightarrow \frac{\rho}{\sqrt{2\pi\left[x + \frac{(\rho^2 - 1)}{2}\right]}} \tag{37}$$

The conditions for accuracy of this asymptotic expression have been determined by comparison to numerical calculations and are given in Table 2.

Table 2. Conditions for Accuracy of the Large-x Asymptotic Solution for y(x, ρ) in the Lindquist-Simmons Approximation

% Accuracy	Minimum Allowed x
0.01	$x \gtrsim 1300$ and $x \gtrsim 85\,\rho^2$
0.10	130 $\quad$ $8.7\,\rho^2$
1.0	14 $\quad$ $2.5\,\rho^2$
10.	5.3 $\quad$ $0.33\,\rho^2$

For very large ρ also, the integrand is sharply peaked about θ = π. However, the asymptotic solution obtained for large ρ is neither realistic nor accurate, and the solution is, in fact, the same as that for large x.

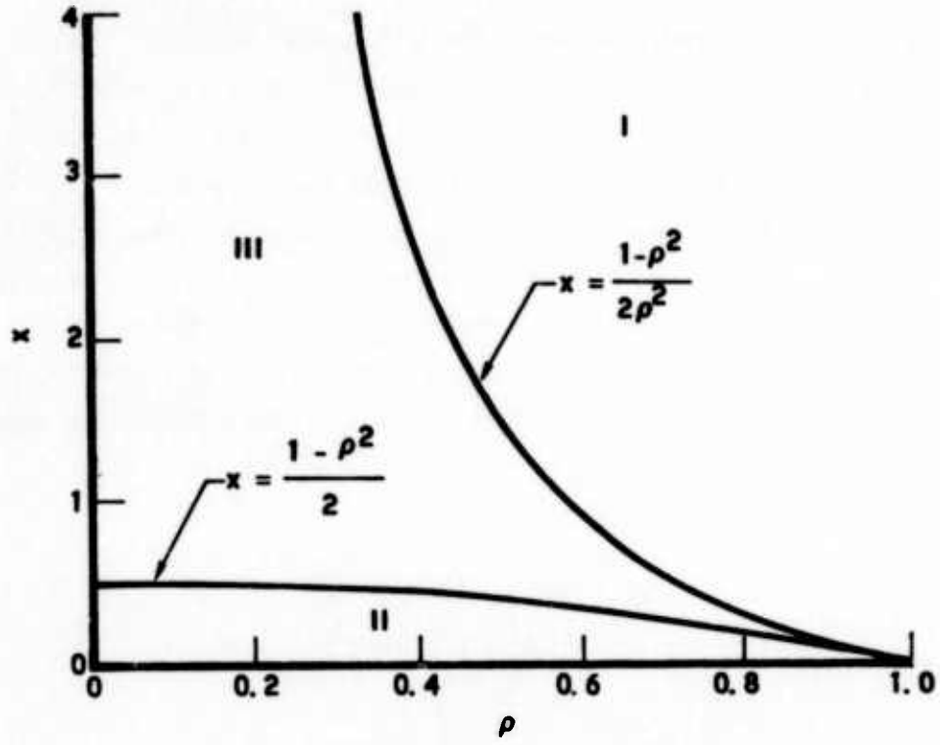

(a) REGIONS OF DISTINCT INTEGRAND FORM

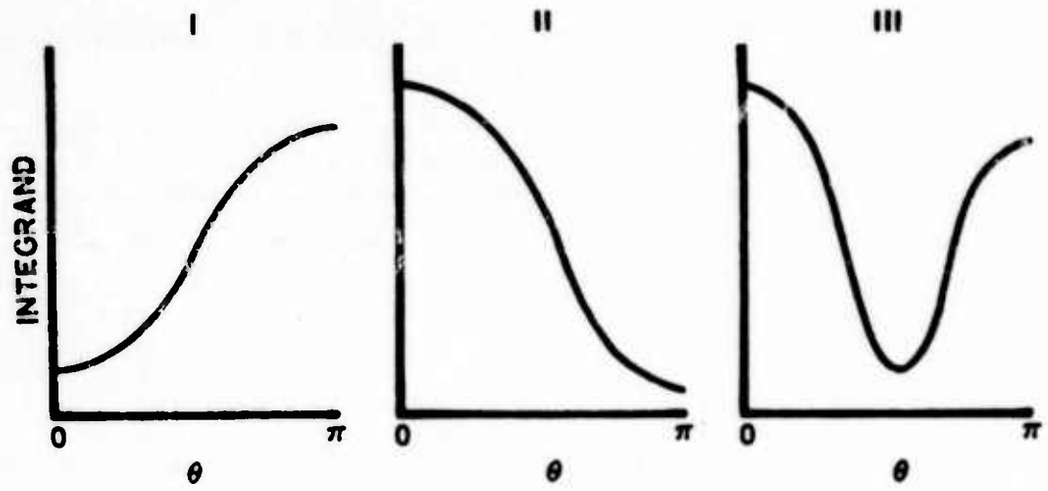

(b) FORMS OF THE INTEGRAND

Fig. 2. Integrand of $y(x, \rho)$ Integral in the Lindquist-Simmons Approximation

For large ρ and small x, ideally y should approach unity whereas the solution obtained approaches $1/\sqrt{\pi}$. This effect is probably due to the fact that the integrand is not a strongly enough varying function with ρ around $\theta = \pi$ to render the asymptotic technique valid.

A similar condition was found when attempting to extract an asymptotic solution for small ρ. In this case, a sharply peaked function occurs around $\theta = 0$. The asymptotic solution obtained is

$$y \rightarrow \frac{e^{-2x}}{\sqrt{\pi}} \tag{38}$$

Although this result is independent of ρ, it is unrealistic in that it also approaches $1/\sqrt{\pi}$ rather than unity as $x \rightarrow 0$. However, it was discovered that, by neglecting the factor $1/\sqrt{\pi}$, the remaining function, namely, e^{-2x}, provides an extremely good approximation to y for small ρ and small x. This approximation can be obtained also by approximating the numerator of the integrand for small x and small ρ by e^{-2x}, i.e., its value at $\theta = 0$ where most of the contribution to the integral is concentrated. For small ρ and large x, a sharp peak occurs around both $\theta = 0$ and $\theta = \pi$ (case III), and an accurate solution can be obtained by adding the two asymptotic solutions for these two conditions together.

$$y \rightarrow e^{-2x} + \frac{\rho}{\sqrt{2\pi\left(x - \frac{1}{2}\right)}} \qquad \text{as } \rho \rightarrow 0 \tag{39}$$

The upper limit on ρ, for which this solution is accurate to a given percentage error, has not been considered in detail. A comparison with exact numerical calculations at $\rho = 10^{-4}$, however, has shown the maximum error to be of the order of 1 percent with this maximum error occurring at $x \simeq 5$.

For $\rho = 10^{-4}$, this value of x is the region where the two contributions to the asymptotic solution are of the same magnitude (Fig. 3). Attempts to adjust the asymptotic solution obtained for large ρ by factors of π or $\sqrt{\pi}$ applied at various places in the equation did not lead to any improved form for an asymptotic solution.

For $10^{-4} \leq x \leq 10^{4}$ and $10^{-4} \leq \rho \leq 10^{4}$, numerical calculations of $y(x, \rho)$ were performed and the results used to form an interpolation table as discussed earlier. Calculations were performed for both x and ρ at the 25 values: 1×10^{-4}, 2×10^{-4}, 5×10^{-4}, 1×10^{-3}, 2×10^{-3}, ... , 5×10^{3}, and 10^{4}. The accuracy of the calculations was set at 1 part in 10^{4} although some entries may be more accurate. The upper limit on x and the upper and lower limits on ρ were set by the fact that the number of $\Delta\theta$ intervals required for accurate numerical integration increased extremely rapidly beyond these limits. The numerical integration was performed using the Wedle approximation with the number of intervals between 0 and π equal to 12n where n is an integer. The limiting value of $n \leq 200$ set the x and ρ limits given above. The calculated y values are listed in Table 3 and illustrated in Fig. 3. A summary of the calculational procedure for all x and ρ is given in Fig. 4.

A comparison of the y-functions appropriate to the CG and LS approximations reveals the following:

a. In both cases, $y(x, \rho)$ is well behaved for very large x and approaches the correct asymptotic form $y \to \rho/\sqrt{2\pi x}$.

b. The functions $y(x, \rho)$ are identical for the case $\rho = 1$ (as they should be since this value reflects the conditions for a homogeneous path).

c. In the CG approximation, y can exceed unity for path conditions where $\rho \gtrsim 2 + 1/\alpha$. In the LS approximation, y never exceeds unity.

d. The transition from the small-x behavior to the asymptotic large-x behavior generally occurs very much faster in the LS approximation than in the CG approximation. Except for

very large ρ, x has achieved the asymptotic form between $x \simeq 5 \rightarrow 8$ in the LS approximation. However, for small ρ in the CG approximation, this changeover to the asymptotic form may be prolonged as far as $x \rightarrow 10^2$ or 10^3 or even further.

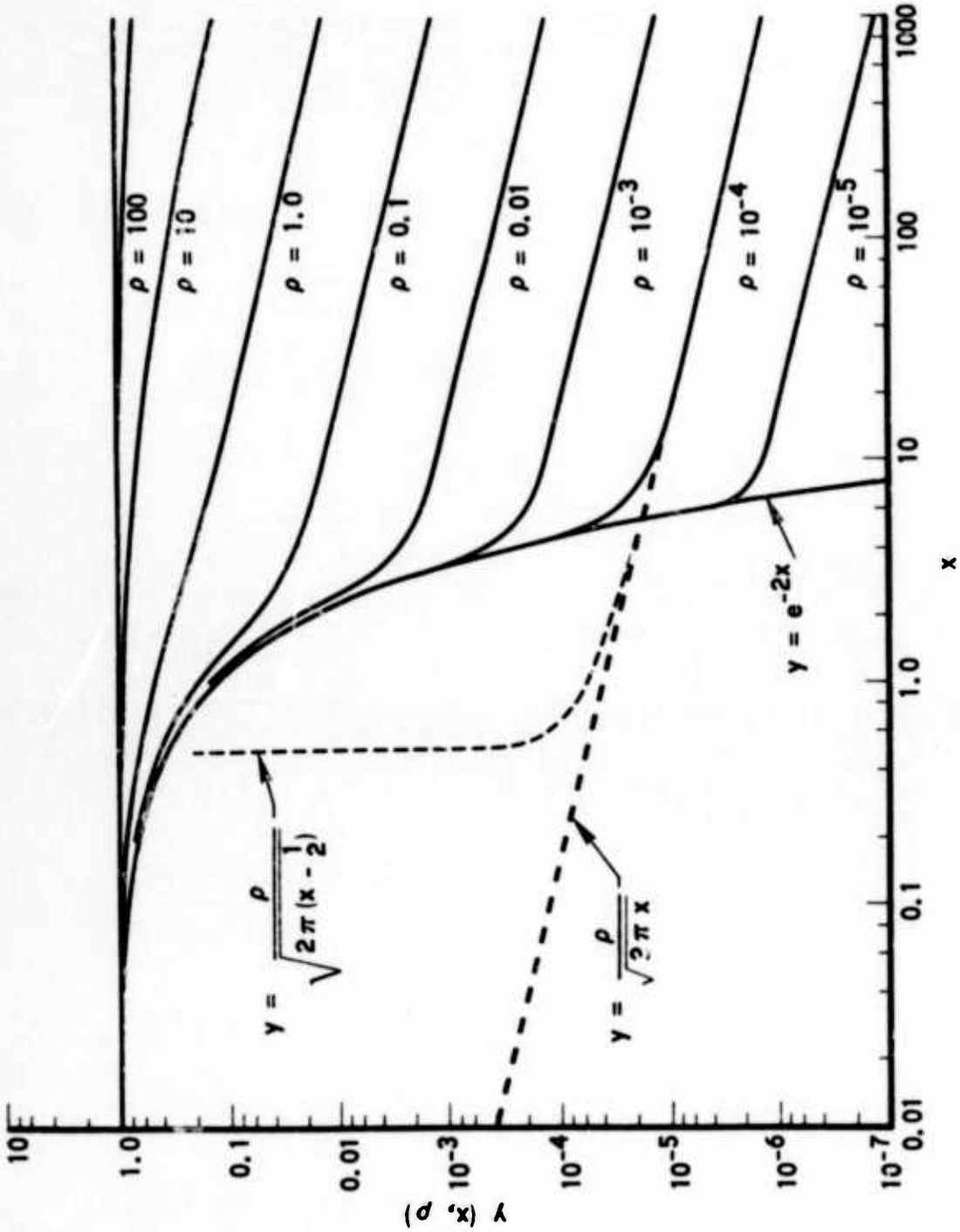

Fig. 3. The Function $\gamma(x, \rho)$ for the Lindquist-Simmons Approximation

Table 3. Tabulation of y(x, ρ) in Lindquist-Simmons Approximation for x and ρ Between 0.0001 and 10,000

X	R= 1.0E-04	R= 2.0E-04	R= 5.0E-04	R= 1.0E-03	R= 2.0E-03	R= 5.0E-03	R= 1.0E-02
1.0E-04	.99980E+00	.99980E+00	.99980E+00	.99980E+00	.99980E+00	.99980E+00	.99980E+00
2.0E-04	.99960E+00	.99960E+00	.99960E+00	.99960E+00	.99960E+00	.99960E+00	.99960E+00
5.0E-04	.99900E+00	.99900E+00	.99900E+00	.99900E+00	.99900E+00	.99901E+00	.99901E+00
1.0E-03	.99801E+00	.99801E+00	.99801E+00	.99801E+00	.99801E+00	.99801E+00	.99802E+00
2.0E-03	.99601E+00	.99601E+00	.99601E+00	.99601E+00	.99602E+00	.99603E+00	.99605E+00
5.0E-03	.99005E+00	.99005E+00	.99005E+00	.99006E+00	.99007E+00	.99010E+00	.99015E+00
1.0E-02	.98020E+00	.98021E+00	.98021E+00	.98022E+00	.98024E+00	.98030E+00	.98039E+00
2.0E-02	.96079E+00	.96081E+00	.96081E+00	.96083E+00	.96087E+00	.96098E+00	.96117E+00
5.0E-02	.90485E+00	.90486E+00	.90486E+00	.90493E+00	.90502E+00	.90530E+00	.90576E+00
1.0E-01	.81875E+00	.81877E+00	.81882E+00	.81890E+00	.81907E+00	.81959E+00	.82044E+00
2.0E-01	.67035E+00	.67036E+00	.67047E+00	.67062E+00	.67091E+00	.67180E+00	.67327E+00
5.0E-01	.36793E+00	.36798E+00	.36812E+00	.36837E+00	.36886E+00	.37031E+00	.37273E+00
1.0E+00	.13539E+00	.13544E+00	.13559E+00	.13585E+00	.13637E+00	.13791E+00	.14047E+00
2.0E+00	.18353E-01	.18390E-01	.18502E-01	.18689E-01	.19061E-01	.20179E-01	.22038E-01
5.0E+00	.67366E-04	.84537E-04	.14324E-03	.24108E-03	.43677E-03	.10238E-02	.20022E-02
1.0E+01	.13143E-04	.26285E-04	.65713E-04	.13143E-03	.26283E-03	.65707E-03	.13141E-02
2.0E+01	.90964E-05	.18193E-04	.45482E-04	.90904E-04	.18193E-03	.45482E-03	.90963E-03
5.0E+01	.56605E-05	.11370E-04	.28425E-04	.56855E-04	.11370E-03	.28425E-03	.56605E-03
1.0E+02	.40045E-05	.80091E-05	.20023E-04	.40045E-04	.80091E-04	.20023E-03	.40045E-03
2.0E+02	.28283E-05	.56625E-05	.14131E-04	.28283E-04	.56525E-04	.14131E-03	.28283E-03
5.0E+02	.17855E-05	.35709E-05	.89273E-05	.17855E-04	.35709E-04	.89273E-04	.17855E-03
1.0E+03	.12620E-05	.25241E-05	.63102E-05	.12620E-04	.25241E-04	.63102E-04	.12620E-03
2.0E+03	.89223E-06	.17845E-05	.44611E-05	.89223E-05	.17845E-04	.44611E-04	.89223E-04
5.0E+03	.56423E-06	.11285E-05	.28212E-05	.56423E-05	.11285E-04	.28212E-04	.56423E-04
1.0E+04	.39896E-06	.79791E-06	.19948E-05	.39896E-05	.79791E-05	.19948E-04	.39896E-04

Table 3. Tabulation of $y(x, \rho)$ in Lindquist-Simmons Approximation for x and ρ Between 0.0001 and 10,000 (Continued)

X	R= 1.0E-02	R= 2.0E-02	R= 5.0E-02	R= 1.0E-01	R= 2.0E-01	R= 5.0E-01	R= 1.0E+00
1.0E-04	.9998uE+00	.9998UE+00	.999A1E+00	.999UUE+00	.99983E+00	.99987E+00	.9959UE+00
2.0E-04	.99960E+00	.99961E+00	.99962E+00	.99964E+00	.99967E+00	.99973E+00	.99980E+00
5.0E-04	.99901E+00	.99902E+00	.99905E+00	.99909E+00	.99917E+00	.99933E+00	.99950E+00
1.0E-03	.99802E+00	.99804E+00	.99810E+00	.99819E+00	.99833E+00	.99867E+00	.99900E+00
2.0E-03	.99605E+00	.99608E+00	.99620E+00	.99637E+00	.99667E+00	.99733E+00	.99800E+00
5.0E-03	.99015E+00	.99025E+00	.99062E+00	.99115E+00	.99170E+00	.99336E+00	.99502E+00
1.0E-02	.98039E+00	.98059E+00	.98114E+00	.98199E+00	.98345E+00	.98678E+00	.99007E+00
2.0E-02	.96117E+00	.96155E+00	.96264E+00	.96432E+00	.96727E+00	.97377E+00	.98030E+00
5.0E-02	.90576E+00	.90666E+00	.90920E+00	.91329E+00	.92037E+00	.93603E+00	.95182E+00
1.0E-01	.82044E+00	.82211E+00	.82696E+00	.83447E+00	.84770E+00	.87715E+00	.90710E+00
2.0E-01	.67327E+00	.67617E+00	.68457E+00	.69708E+00	.72040E+00	.77293E+00	.82594E+00
5.0E-01	.37273E+00	.37751E+00	.39142E+00	.41231E+00	.45276E+00	.54494E+00	.64204E+00
1.0E+00	.14047E+00	.14554E+00	.16044E+00	.18430E+00	.22648E+00	.33767E+00	.46576E+00
2.0E+00	.22030E-01	.25745E-01	.36775E-01	.54838E-01	.89697E-01	.18374E+00	.30621E+00
5.0E+00	.20022E-02	.39580E-02	.98266E-02	.19594E-01	.39043E-01	.96025E-01	.18359E+00
1.0E+01	.13141E-02	.26282E-02	.65702E-02	.13137E-01	.26291E-01	.65228E-01	.12703E+00
2.0E+01	.90963E-03	.18183E-02	.45460E-02	.90951E-02	.18183E-01	.45329E-01	.89780E-01
5.0E+01	.56650E-03	.11370E-02	.28425E-02	.56647E-02	.11366E-01	.28383E-01	.56262E-01
1.0E+02	.40045E-03	.80090E-03	.20022E-02	.40045E-02	.80082E-02	.20010E-01	.39964E-01
2.0E+02	.28263E-03	.56525E-03	.14131E-02	.28262E-02	.56522E-02	.14127E-01	.28227E-01
5.0E+02	.17855E-03	.35709E-03	.89273E-03	.17855E-02	.35709E-02	.89262E-02	.17856E-01
1.0E+03	.12620E-03	.25241E-03	.63102E-03	.12620E-02	.25241E-02	.63098E-02	.12617E-01
2.0E+03	.89223E-04	.17845E-03	.44611E-03	.89223E-03	.17844E-02	.44610E-02	.89212E-02
5.0E+03	.56423E-04	.11285E-03	.28212E-03	.56423E-03	.11285E-02	.28211E-02	.56420E-02
1.0E+04	.39895E-04	.79791E-04	.19948E-03	.39895E-03	.79791E-03	.19948E-02	.39885E-02

Table 3. Tabulation of $y(x, \rho)$ in Lindquist-Simmons Approximation for x and ρ Between 0.0001 and 10,000 (Continued)

X	R= 1.0E+00	R= 2.0E+00	R= 5.0E+00	R= 1.0E+01	R= 2.0E+01	R= 5.0E+01	R= 1.0E+02
1.0E-04	.99996E+00	.99995E+00	.99997E+00	.99996E+00	.99999E+00	.10000E+01	.10000E+01
2.0E-04	.99986E+00	.99987E+00	.99993E+00	.99990E+00	.99998E+00	.99999E+00	.10000E+01
5.0E-04	.99950E+00	.99967E+00	.99983E+00	.99991E+00	.99995E+00	.99998E+00	.99999E+00
1.0E-03	.99900E+00	.99933E+00	.99957E+00	.99982E+00	.99990E+00	.99996E+00	.99998E+00
2.0E-03	.99800E+00	.99867E+00	.99933E+00	.99964E+00	.99981E+00	.99992E+00	.99996E+00
5.0E-03	.99502E+00	.99668E+00	.99834E+00	.99969E+00	.99953E+00	.99980E+00	.99990E+00
1.0E-02	.99007E+00	.99338E+00	.99669E+00	.99819E+00	.99905E+00	.99961E+00	.99980E+00
2.0E-02	.98036E+00	.98684E+00	.99341E+00	.99644E+00	.99811E+00	.99922E+00	.99961E+00
5.0E-02	.95182E+00	.96775E+00	.98381E+00	.99115E+00	.99536E+00	.99803E+00	.99903E+00
1.0E-01	.90710E+00	.93755E+00	.96852E+00	.98276E+00	.99095E+00	.99627E+00	.99812E+00
2.0E-01	.82694E+00	.88272E+00	.94030E+00	.96724E+00	.98276E+00	.99288E+00	.99640E+00
5.0E-01	.64504E+00	.75374E+00	.87179E+00	.92870E+00	.96220E+00	.98435E+00	.99208E+00
1.0E+00	.46576E+00	.61609E+00	.79262E+00	.88275E+00	.93730E+00	.97383E+00	.98672E+00
2.0E+00	.30851E+00	.47505E+00	.69850E+00	.82441E+00	.90443E+00	.95904E+00	.97944E+00
5.0E+00	.18354E+00	.32521E+00	.56686E+00	.73105E+00	.84839E+00	.93430E+00	.96622E+00
1.0E+01	.12783E+00	.23934E+00	.48561E+00	.64300E+00	.79338E+00	.90704E+00	.95211E+00
2.0E+01	.89756E-01	.17540E+00	.38854E+00	.52567E+00	.72557E+00	.87274E+00	.93290E+00
5.0E+01	.56562E-01	.11149E+00	.25678E+00	.39065E+00	.61679E+00	.80955E+00	.89674E+00
1.0E+02	.39944E-01	.79531E-01	.18941E+00	.33695E+00	.52381E+00	.74691E+00	.85867E+00
2.0E+02	.28227E-01	.56245E-01	.13723E+00	.25574E+00	.42795E+00	.67102E+00	.80915E+00
5.0E+02	.17854E-01	.35638E-01	.88194E-01	.17069E+00	.30894E+00	.55373E+00	.72360E+00
1.0E+03	.12617E-01	.25210E-01	.62714E-01	.12326E+00	.23239E+00	.45832E+00	.64384E+00
2.0E+03	.89212E-02	.17836E-01	.44473E-01	.88146E-01	.17000E+00	.36477E+00	.55304E+00
5.0E+03	.56420E-02	.11282E-01	.28176E-01	.56145E-01	.11071E+00	.25541E+00	.42760E+00
1.0E+04	.39895E-02	.79763E-02	.19935E-01	.39797E-01	.79016E-01	.18863E+00	.33621E+00

Table 3. Tabulation of $y(x, \rho)$ in Lindquist-Simmons Approximation for x and ρ Between 0.0001 and 10,000 (Concluded)

X	R= 1.0E+02	R= 2.0E+02	R= 5.0E+02	R= 1.0E+03	R= 2.0E+03	R= 5.0E+03	R= 1.0E+04
1.0E-04	.10000E+01	.10000E+01	.10000E+01	.10000E+01	.10000E+01	.10000E+01	.10000E+01
2.0E-04	.10000E+01	.10000E+01	.10000E+01	.10000E+01	.10000E+01	.10000E+01	.10000E+01
5.0E-04	.99999E+00	.10000E+01	.10000E+01	.10000E+01	.10000E+01	.10000E+01	.10000E+01
1.0E-03	.99998E+00	.99998E+00	.10000E+01	.10000E+01	.10000E+01	.10000E+01	.10000E+01
2.0E-03	.99996E+00	.99996E+00	.99999E+00	.10000E+01	.10000E+01	.10000E+01	.10000E+01
5.0E-03	.99990E+00	.99990E+00	.99998E+00	.99999E+00	.10000E+01	.10000E+01	.10000E+01
1.0E-02	.99980E+00	.99980E+00	.99996E+00	.99998E+00	.99999E+00	.10000E+01	.10000E+01
2.0E-02	.99961E+00	.99960E+00	.99992E+00	.99996E+00	.99998E+00	.99999E+00	.10000E+01
5.0E-02	.99903E+00	.99951E+00	.99981E+00	.99990E+00	.99995E+00	.99998E+00	.10000E+01
1.0E-01	.99812E+00	.99905E+00	.99962E+00	.99981E+00	.99991E+00	.99995E+00	.99998E+00
2.0E-01	.99640E+00	.99819E+00	.99927E+00	.99964E+00	.99982E+00	.99993E+00	.99996E+00
5.0E-01	.99208E+00	.99602E+00	.99840E+00	.99922E+00	.99960E+00	.99984E+00	.99992E+00
1.0E+00	.98672E+00	.99331E+00	.99731E+00	.99865E+00	.99933E+00	.99973E+00	.99987E+00
2.0E+00	.97944E+00	.98962E+00	.99583E+00	.99791E+00	.99895E+00	.99958E+00	.99979E+00
5.0E+00	.96022E+00	.98267E+00	.99309E+00	.99653E+00	.99827E+00	.99931E+00	.99965E+00
1.0E+01	.95211E+00	.97558E+00	.99012E+00	.99504E+00	.99751E+00	.99901E+00	.99950E+00
2.0E+01	.93290E+00	.96552E+00	.98590E+00	.99295E+00	.99646E+00	.99863E+00	.99929E+00
5.0E+01	.89677E+00	.94613E+00	.97788E+00	.98884E+00	.99440E+00	.99775E+00	.99888E+00
1.0E+02	.85857E+00	.92506E+00	.96891E+00	.98420E+00	.99208E+00	.99662E+00	.99831E+00
2.0E+02	.80915E+00	.89653E+00	.95645E+00	.97784E+00	.98882E+00	.99501E+00	.99775E+00
5.0E+02	.72366E+00	.84394E+00	.93247E+00	.96530E+00	.98241E+00	.99231E+00	.99644E+00
1.0E+03	.64384E+00	.79041E+00	.90629E+00	.95148E+00	.97526E+00	.98999E+00	.99498E+00
2.0E+03	.55354E+00	.72360E+00	.87180E+00	.93246E+00	.96530E+00	.98609E+00	.99290E+00
5.0E+03	.44270E+00	.61570E+00	.80902E+00	.89646E+00	.94599E+00	.97703E+00	.98802E+00
1.0E+04	.33621E+00	.52316E+00	.74656E+00	.85648E+00	.92496E+00	.96807E+00	.98424E+00

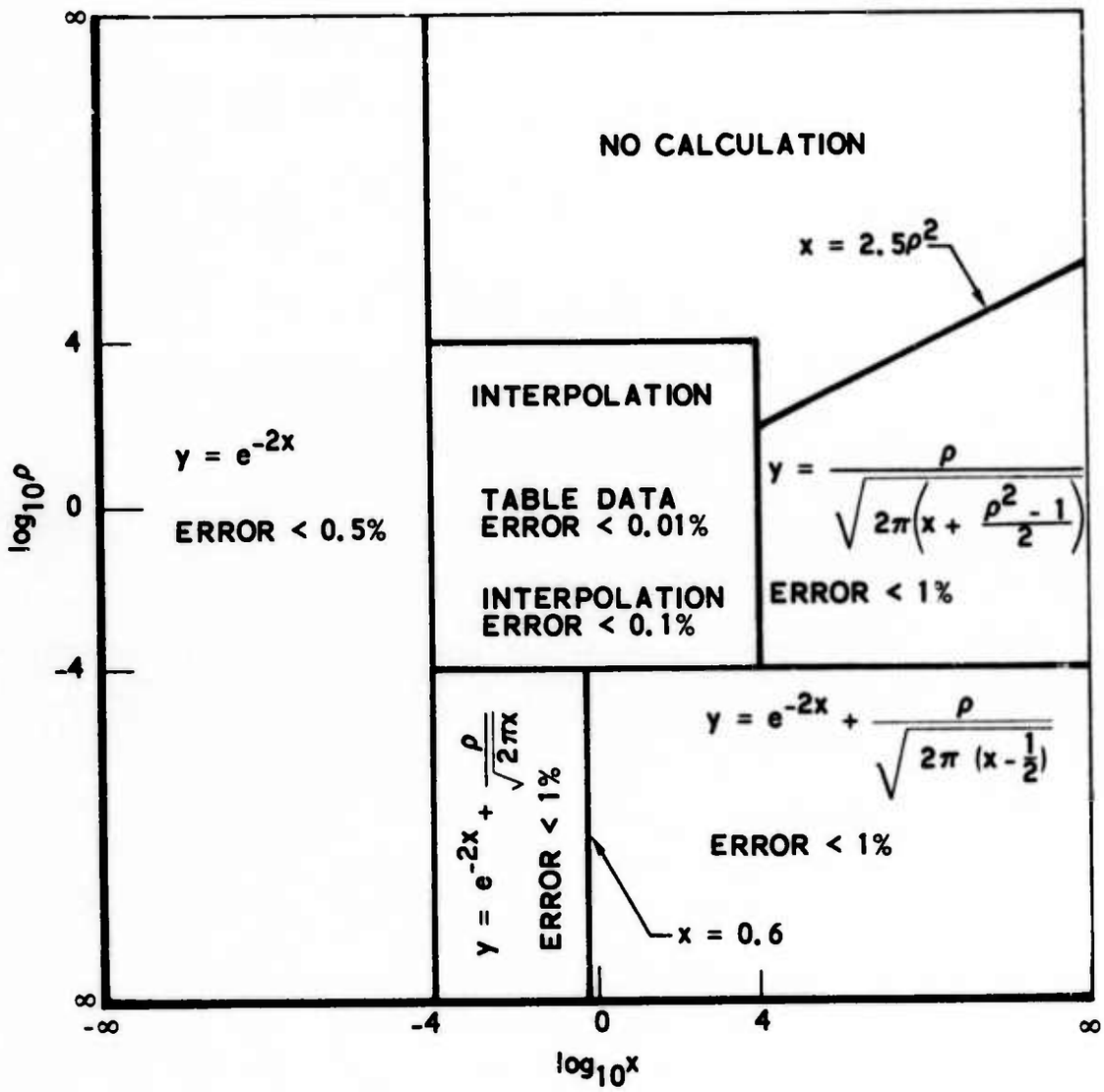

Fig. 4. Summary of y(x, ρ) Calculation in the Lindquist-Simmons Approximation

III. BAND MODEL PARAMETERS

The basic data required for performing band model calculations are the band model parameters $\bar{k}$ and β (or, equivalently for β, the average line width parameter $\bar{\gamma}$ and the mean line spacing parameter δ since $\beta \equiv 2\pi\bar{\gamma}/\delta$). These parameters must, of course, be consistent with the band model formulation used. Three sets of these parameters are presently in use.

A. GENERAL DYNAMICS PARAMETERS

A set of band model parameters that was generated by General Dynamics and intended primarily for use in high-temperature applications has been in existence for several years. The most recent publication of these parameters is given by Ludwig et al.[2] For both CO_2 and H_2O, the listed variables are $\bar{k}$ and δ and are appropriate for use in the statistical band model formulation with an exponential line intensity distribution.

The data for CO_2 are the result of theoretical calculations based on the known quantum mechanical properties of linear triatomic molecules. Results obtained using these data are generally conceded to be in good agreement with experimental results. The $\bar{k}$ parameter for CO_2 is complete for both the 4.3-μm and 2.7-μm bands for temperatures between 300 and 3000°K. The δ data for the 4.3-μm band are also complete for the temperature range of 300 to 3000°K. However, for the 2.7-μm band, δ data are given only up to 1800°K. Both the $\bar{k}$ and δ data are given at spectral intervals of 5 or 10 cm^{-1} and presumably reflect values appropriate to spectral resolution intervals of about the same size.

General Dynamics data for H_2O are derived almost exclusively from experimental measurements. Because of the nonlinearity of H_2O, the exact theoretical calculation of band model parameters is extremely complicated and difficult, particularly at high temperatures. The bulk of the H_2O data

above ~1200°K were obtained in a consistent manner from emission/absorption measurements made on very long strip-burner H_2/O_2 flames. Data below ~1200°K are based on extrapolations from these high-temperature data and on the analysis of published low-temperature H_2O spectra. Recommended values are given in 25 cm^{-1} steps over the spectral region from 50 to 9300 cm^{-1} for $\bar{k}$ and 1150 to 7500 cm^{-1} for δ. The spectral resolution width is also 25 cm^{-1}. The $\bar{k}$ data are given for the temperature range from 300 to 3000°K, but the δ data are given from only 600 to 3000°K.

The generation of β data from the General Dynamics δ data is effected using the line width parameters given in Table 4 (which has been taken from Ref. 2). The line width (half-width at half-height) for the species i is computed from these parameters by

$$\gamma_i(T) = \sum_j \left\{ (\gamma_i^j)_0 \, p_j \left(\frac{273}{T}\right)^{n_j} \right\} + (\gamma_i^*)_0 \, p_i \left(\frac{273}{T}\right)^{n_i^*} \qquad (40)$$

The summation term accounts for foreign gas broadening ($j \neq i$) and nonresonant self-broadening ($j = i$) contributions to the line width. The second term accounts for the resonant self-broadening effects which occur for H_2O. The term p_i is the partial pressure of the ith species. Data for $\bar{k}$, δ, and γ have been used to generate a card file of $\bar{k}(\nu, T)$ and $\beta_0(\nu, T)$ data for H_2O and CO_2. The units of $\bar{k}$ are cm^{-1}/atm and were obtained by multiplying the General Dynamics data by 273/T. The units of β_0 are atm^{-1} for nonresonant self-broadening only. Simple semilogarithmic linear extrapolations were used to generate δ values for H_2O at temperatures below 600°K and for CO_2 at temperatures both above 1800°K and below 300°K.

Although the General Dynamics data are presumably appropriate for the statistical band model with the assumption of an exponential intensity distribution, these data are actually quite suitable for use with the assumption

Table 4. General Dynamics Line Width Parameters

Molecule (i)	Broadener (j)	$(\gamma_i^j)_0$ (cm^{-1}/atm)	n_j	$(\gamma_i^*)_0$ (cm^{-1}/atm)	n_i^*
H_2O	H_2O	0.09	1/2	0.44	1
	CO_2	0.12	1/2		
	N_2	0.09	1/2		
	O_2	0.04	1/2		
CO_2	CO_2	0.09	1/2	0	NA
	H_2O	0.07	1/2		
	N_2	0.07	1/2		
	O_2	0.06	1/2		

$$\gamma_i(T) = \sum_j \left\{ (\gamma_i^j)_0 \, p_j \left(\frac{273}{T}\right)^{n_j} \right\} + (\gamma_i^*)_0 \, p_i \left(\frac{273}{T}\right)^{n_i^*}$$

Nonresonant self-broadening and foreign gas broadening

Resonant self-broadening

of a constant line intensity distribution. The conventional curve of growth for the exponential distribution function is

$$\frac{W}{\delta} = \beta \frac{x}{\sqrt{1 + 2x}} \tag{41}$$

In order for this function to assume the correct form in the limit of strong absorption, the parameter β has to be defined as $4/\pi$ times the parameter β consistent for use with the constant line intensity curve of growth. The constant line intensity β-parameter can be used with the exponential distribution curve of growth if this factor $4/\pi$ is absorbed into the functional dependence of W/δ. When this functional transformation is performed, the resulting exponential distribution curve of growth becomes

$$\frac{W}{\delta} = \beta \frac{x}{\sqrt{1 + \frac{\pi x}{2}}} \tag{42}$$

Since this is the curve of growth function recommended for use with the General Dynamics band model parameters, it is concluded that the General Dynamics parameters are suitable for use with the constant line intensity distribution curve of growth also.

B. LINE-AVERAGED PARAMETERS

The second and third sets of band model parameters were generated from the comprehensive line compilation atlas compiled by AFCRL.[6] This data set provides line data for each of over 100,000 lines for seven atmospheric absorbing species including H_2O and CO_2. The data given for

[6] R. A. McClatchey, W. S. Benedict, S. A. Clough, D. E. Burch, R. F. Calfee, K. Fox, L. S. Rothman, and J. S. Garing, AFCRL Atmospheric Absorption Line Parameters Compilation, AFCRL-TR-73-006, Air Force Cambridge Research Laboratories, Mass. (25 January 1973).

each line include the line position $\nu(cm^{-1})$, the line strength S (cm^{-1}/molecule cm^{-2} at 296°K), the line half-width parameter γ (cm^{-1}/atm for air broadening at 296°K), and the energy of the lower level of the transition E (cm^{-1}). Two approaches have been taken in averaging these line data over small spectral intervals to provide band model parameters. The first approach is the straightforward interpretation that the appropriate averages are given simply by

$$\bar{k} = \frac{1}{\Delta\nu}\sum_{i=1}^{N} S(i) \tag{43}$$

and

$$\beta_0 = \frac{2\pi\bar{\gamma}_0}{\delta} \tag{44}$$

where

$$\bar{\gamma}_0 = \frac{1}{N}\sum_{i=1}^{N} \gamma_0(i) \tag{45}$$

In these expressions, $\Delta\nu$ is the width of the spectral interval, N is the number of lines in the interval, and δ is the mean line spacing $\delta = \Delta\nu/N$. The zero subscript on β and γ indicate values per unit pressure. The second approach provides for an exact fit in the weak line and strong line limits between the general statistical band model formulation and the statistical band model in which the constant line intensity distribution function is assumed. This development is outlined by Goody.[4] In the general statistical

band model, the average integrated absorptance for a band of isolated spectral lines is

$$\bar{A} = \frac{1}{\Delta\nu} \sum_{i=1}^{N} W(i) \tag{46}$$

where W(i) is the equivalent width for the ith line in the inverval. For a Lorentzian line and homogeneous path,

$$W(i) = 2\pi\, \gamma(i)\, f(x) \tag{47}$$

where f(x) is the Ladenburg-Reiche function, x is the dimensionless optical depth parameter $x = S(i)\, u/2\pi\gamma(i)$, and u is the optical depth. Thus, in the general statistical band model formulation, $\bar{A}$ is given explicitly in terms of the line data S(i), $\gamma(i)$. When the constant line intensity distribution is applied to the statistical band model, the average integrated absorptance appropriate to the interval $\Delta\nu$ for a band of isolated spectral lines is

$$\bar{A} = \beta\, f(x) \tag{48}$$

where

$$x = \frac{\bar{k}u}{\beta} \tag{49}$$

In this case, the average integrated absorptance is given in terms of the band model parameters $\bar{k}$ and β. In the weak line limit, as $x \to 0$ and $f(x) \to x$, the equating of $\bar{A}$ given by Eqs. (46) and (48) then results in an expression for $\bar{k}$ that is the same as Eq. (43). In the strong line limit,

as $x \to \infty$ and $f(x) \to \sqrt{2x/\pi}$, the equating of $\bar{A}$ given by Eqs. (46) and (48) leads to the result given by Eq. (44) except that $\bar{\gamma}_0$ is now given by the expression

$$\bar{\gamma}_0 = \frac{1}{N} \frac{\left[\sum_{i=1}^{N} \sqrt{S(i)\ \gamma_0(i)}\right]^2}{\sum_{i=1}^{N} S(i)} \tag{50}$$

The essential difference between these two approaches is that the second approach applies a line-strength dependent weighting operation to the line widths. This second approach is significant in that it imparts a temperature dependence (through the temperature dependence of S) to $\bar{\gamma}_0$ other than just the normal $T^{-1/2}$ dependence that is applied in the first approach.

These line-averaging calculations are performed by the computer program LINAVE, which reads in the AFCRL line data and performs the averaging calculations in specified spectral intervals over a specified temperature range. The line strengths S(i) are computed from the value given at the standard temperature $T_0 = 296^\circ K$ by

$$S_i(T) = S_i(T_0)\ \frac{Q_R(T_0)}{Q_R(T)}\ \frac{Q_V(T_0)}{Q_V(T)} \left[\frac{1 - e^{-\nu(i)/kT}}{1 - e^{-\nu(i)/kT_0}}\right] \exp\left[\frac{-E(i)}{k}\left(\frac{1}{T} - \frac{1}{T_0}\right)\right] \tag{51}$$

The factors Q_R and Q_V are the rotational and vibrational partition functions respectively. The exponential term accounts for the Boltzmann distribution population of molecules in the energy level E(i), and the term in brackets

accounts for stimulated emission effects. The ratio of rotational partition functions is given by

$$\frac{Q_R(T_0)}{Q_R(T)} \simeq \left(\frac{T_0}{T}\right)^m \tag{52}$$

where m = 1 for H_2O (H_2O is assumed to be a nearly symmetric-top molecule) and m = 3/2 for CO_2. The molecular vibrational partition function is assumed to be the product of simple harmonic oscillator partition functions for each vibrational mode of the molecule,

$$Q_V(T) = \left[1 - e^{-\nu_1/kT}\right]^{-d_1} \left[1 - e^{-\nu_2/kT}\right]^{-d_2} \left[1 - e^{-\nu_3/kT}\right]^{-d_3} \tag{53}$$

where ν_1, ν_2, and ν_3 are the fundamental oscillatory frequencies of the molecule and d_1, d_2, and d_3 are the degeneracies associated with these modes. For CO_2, $\nu_1 = 1388.17\ cm^{-1}$, $\nu_2 = 667.40\ cm^{-1}$, and $\nu_3 = 2349.16\ cm^{-1}$. For H_2O, $\nu_1 = 3657.0\ cm^{-1}$, $\nu_2 = 1594.7\ cm^{-1}$, and $\nu_3 = 3755.7\ cm^{-1}$. The degeneracies for all modes of both CO_2 and H_2O are unity, except for the doubly degenerate bending mode ν_2 in the linear CO_2 molecule for which $d_2 = 2$. The value $1/k = 1.439\ cm\ ^\circ K$ is used throughout.

The temperature variation given in Eq. (51) accounts for the change in the population of absorbers in the energy level E(i) with temperature. Another temperature variation must be included to convert S_i from the AFCRL units of cm^{-1}/(molecule cm^{-2}) to the standard units used in this work, i.e., cm^{-2}/atm. This conversion is effected by multiplying $S_i(T)$ obtained from Eq. (51) by the conversion factor

$$2.480 \times 10^{19} \left(\frac{296^\circ K}{T}\right) \frac{\text{molecules}}{\text{atm cm}^3} \tag{54}$$

The line broadening parameters included in the AFCRL line atlas are, presumably, the broadening parameters appropriate to foreign gas (air) broadening. The line width data of Table 4 have been used to convert these parameters to reflect values appropriate to nonresonant self-broadening. Note that only the ratios of the line width parameters from Table 4 are used and not the line width parameters themselves. The $\gamma_0(i)$ values used in Eqs. (45) and (50) are thus determined from the AFCRL values by multiplying the latter by the factor

$$c\sqrt{\frac{273}{T}} \tag{55}$$

where $c = 1.186$ for H_2O and $c = 1.382$ for CO_2.

The LINAVE Program computes $\bar{k}(\nu, T)$ and $\beta_0(\nu, T)$ where $\bar{k}$ has units (cm^{-1}/atm) and β_0 has units (atm^{-1} for nonresonant self-broadening). Most of the work presently being done uses $\bar{k}$ and β_0 values computed for $\Delta\nu = 25\ cm^{-1}$ that have been computed for wave number steps of $5\ cm^{-1}$ between $2500\ cm^{-1}$ and $4400\ cm^{-1}$ for H_2O and between $3075\ cm^{-1}$ and $3875\ cm^{-1}$ for CO_2 for 14 temperatures between 100°K and 3000°K.

C. COMPARISON OF PARAMETER SETS

The $\bar{k}$ value for CO_2 at the 2.7-μm band center position $\nu = 3700\ cm^{-1}$ is shown in Fig. 5. In this comparison, the General Dynamics set and the line-averaged set are seen to agree well up to a temperature of ~1000°K. A comparison of β_0 parameters for the same condition is shown in Fig. 6 where good agreement between the General Dynamics parameter and the line-averaged parameter computed from Eq. (50) is evident up to a temperature of ~600°K. However, a substantial difference may be seen to occur between the line-averaged β_0 values computed from Eqs. (45) and (50). The discrepancy between $\bar{k}$ and β_0 from Eq. (50) for temperatures higher than ~600°K can probably be explained by the fact that the AFCRL line compilation

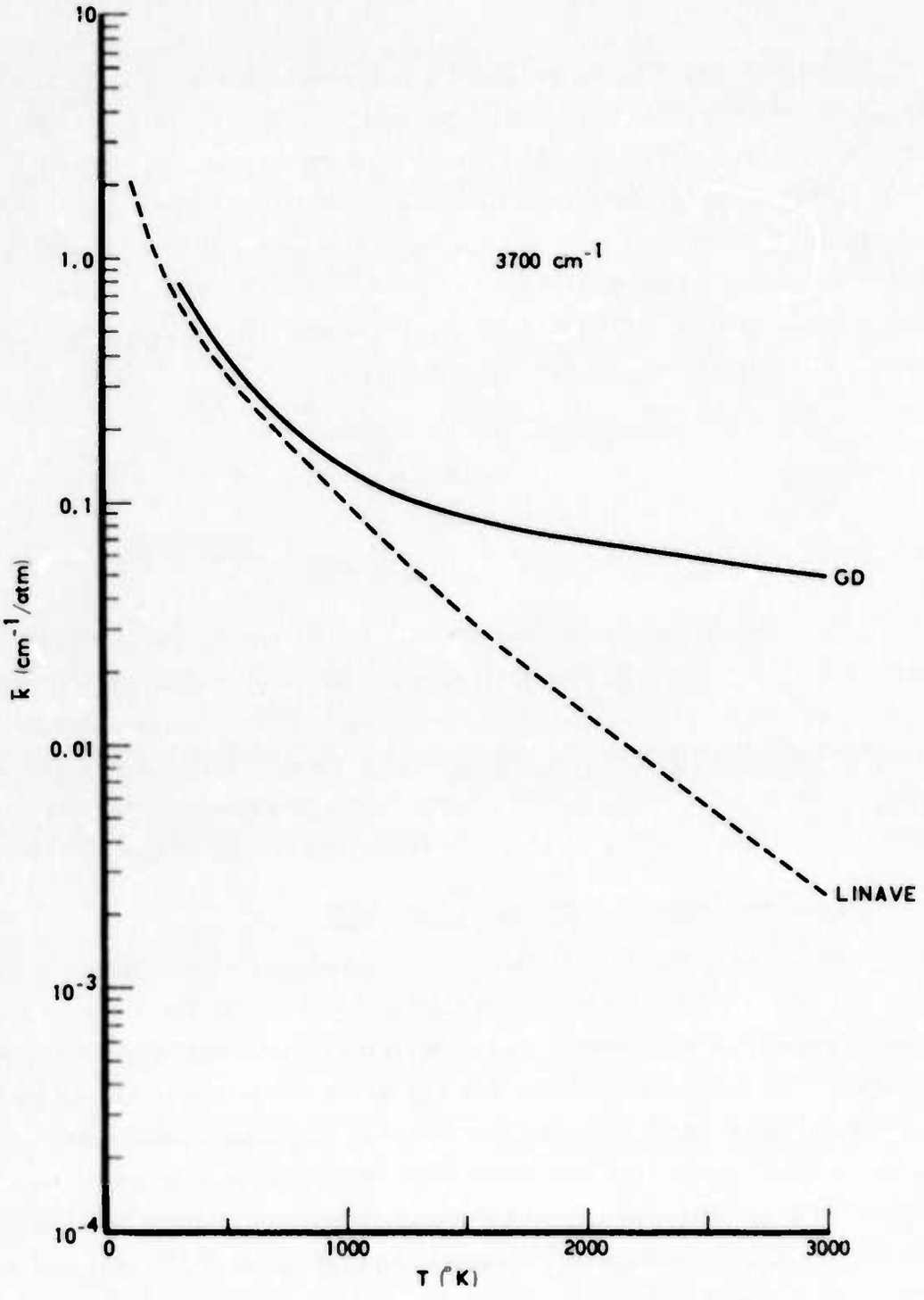

Fig. 5. CO_2 Mean Absorption Coefficient

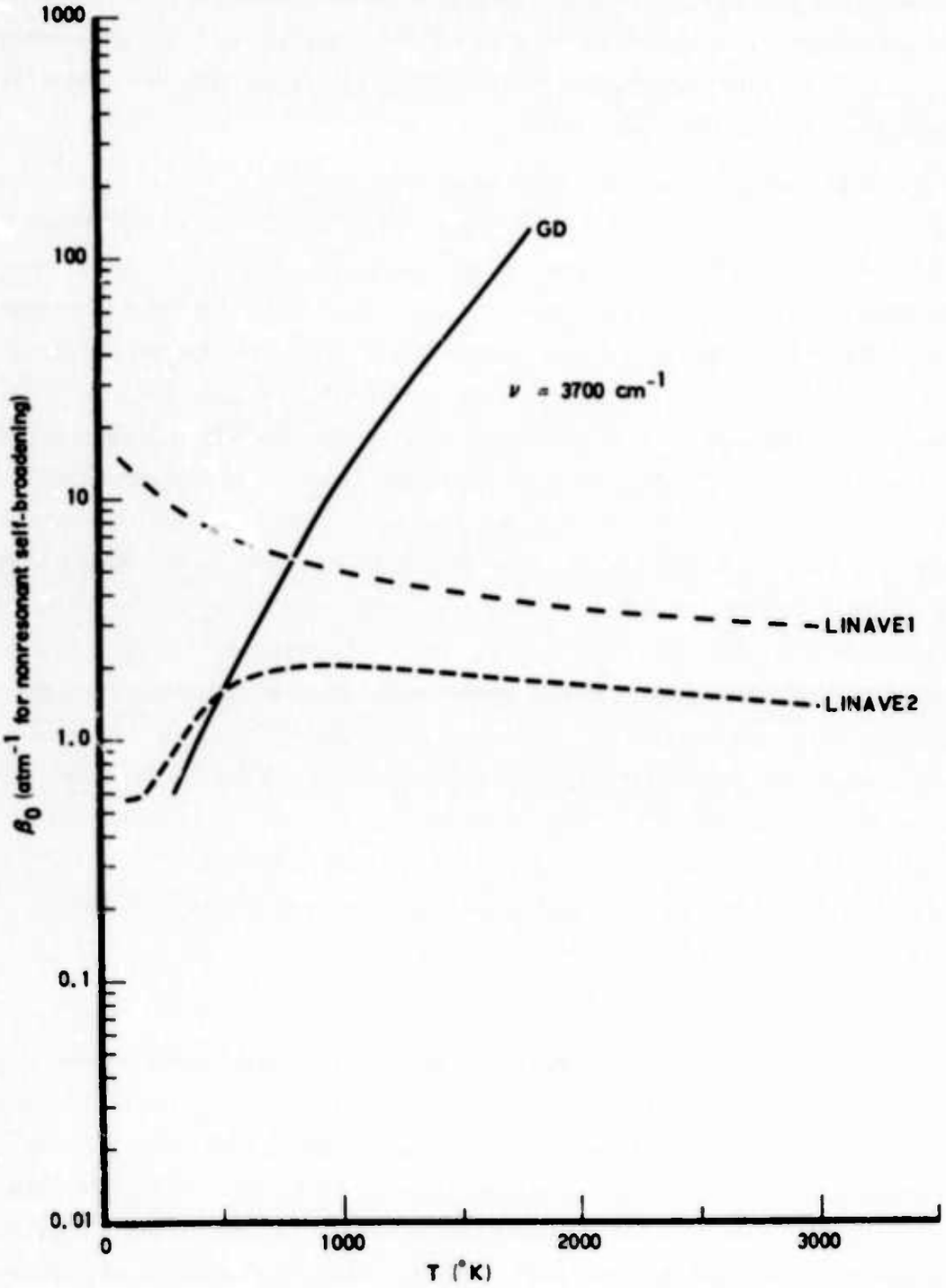

Fig. 6. CO_2 Line Width/Spacing Parameter

was generated primarily for calculations involving atmospheric slant paths where maximum temperatures of only ~350°K are likely to be encountered. Therefore, lines that become important only at higher temperatures have not been included in the compilation.

Similar comparisons for H_2O at wave numbers ν = 3600 cm^{-1} (near the 2.7-μm band center) and ν = 3200 cm^{-1} (in the 2.7-μm band wing) are shown in Figs. 7 and 8. The values of $\bar{k}$ from the two sets for the band center region (Fig. 7) are also seen to compare well. In the band wing position, however, there is little resemblance between the temperature variations of $\bar{k}$ from the two sets. For temperatures less than ~1000°K, the most probable cause of the discrepancy in the wing is the experimental error involved in attempting to measure very small absorptance values. For the higher temperatures, the most probable cause of the discrepancy is again the lack of inclusion of high-temperature lines in the AFCRL line compilation. These same arguments can also be applied to the β_0 comparison shown in Fig. 8(a) for H_2O in the 3200 cm^{-1} region. In the 3600 cm^{-1} region, illustrated in Fig. 8(b), a reasonably good transition from the low-temperature line-averaged β_0 computed from Eq. (50) to the high-temperature General Dynamics β_0 is evident in the region of 1250°K. A detailed investigation of the matching of the low-temperature line-averaged parameters and the high-temperature empirical General Dynamics parameters for H_2O will be the subject of future work. At present, one or the other of these parameter sets is used at all temperatures.

D. BROADENING EFFECTS

The basic band model parameter data input used in the transmittance calculations are the $\bar{k}$ and β_0 data just discussed. The β_0 parameters are the intrinsic values for nonresonant self-broadening with units of atm^{-1}. The actual value of the band model parameter β depends on the particular species composition existing at the point where β is calculated. For both atmospheric paths and hot gas source paths, the only species considered to

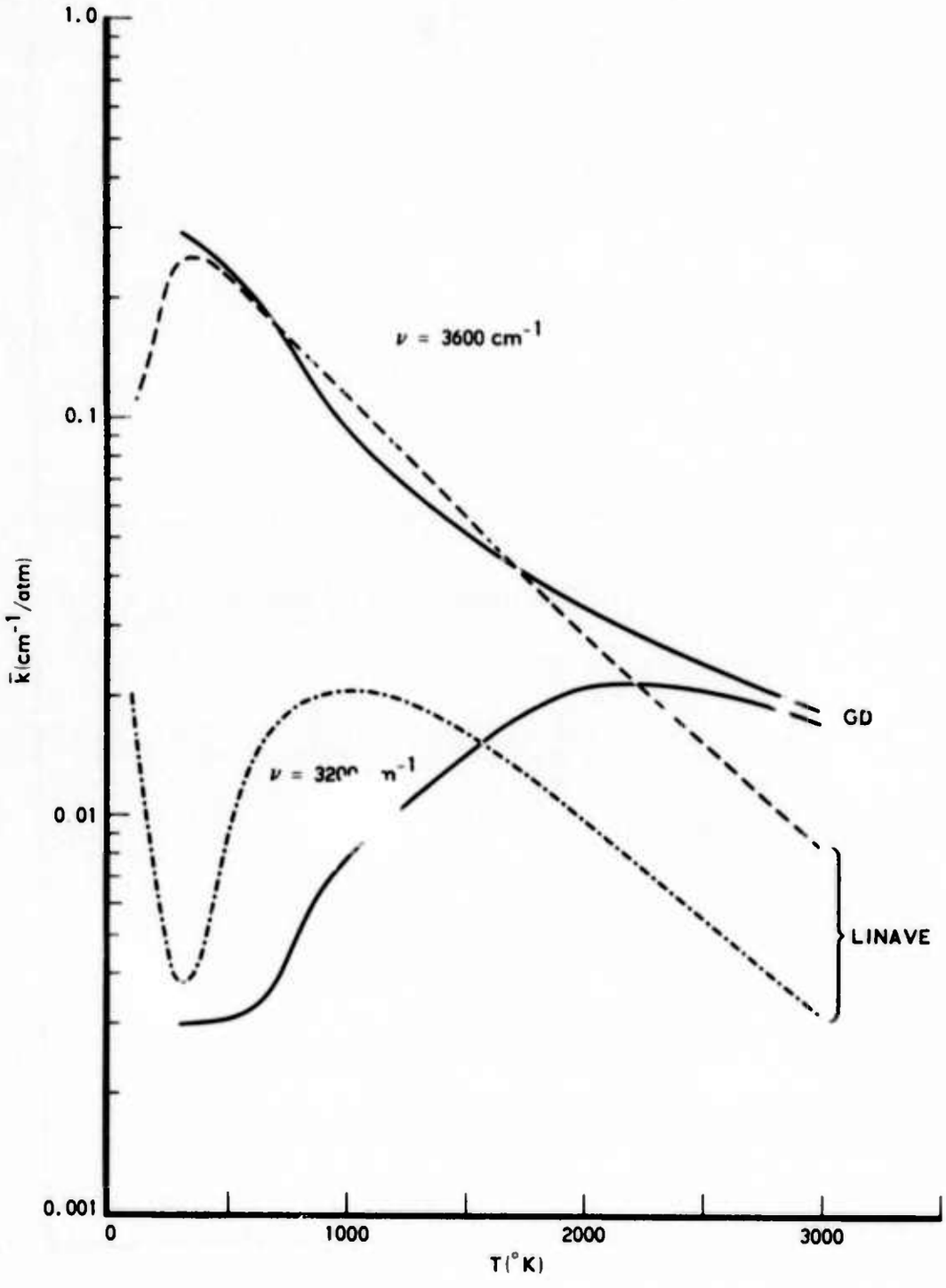

Fig. 7. H_2O Mean Absorption Coefficient

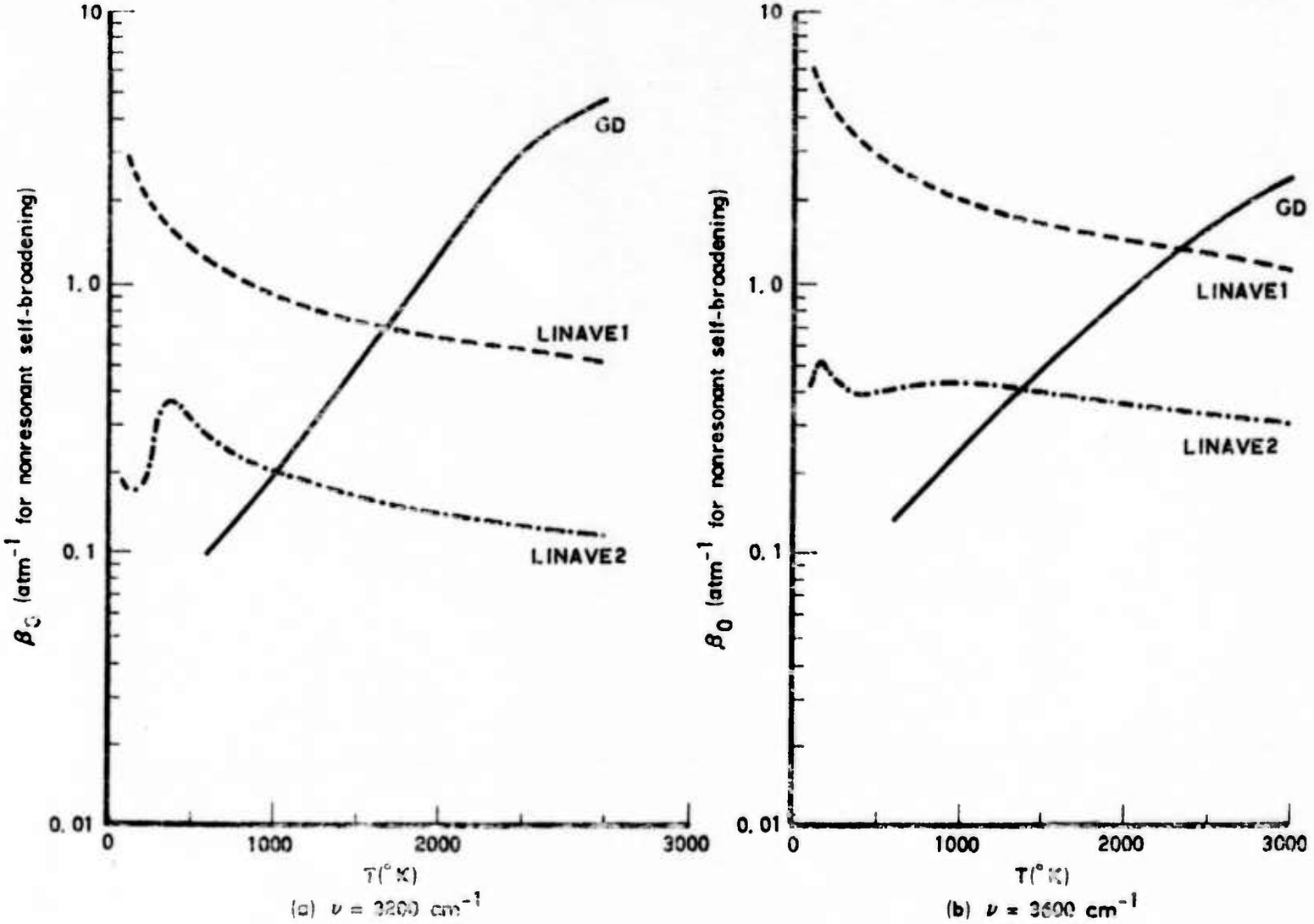

Fig. 8. H_2O Line Width/Spacing Parameter

be present are CO_2, H_2O, and air (78 percent N_2 and 22 percent O_2 by pressure). From Eq. (40) and the ratio of line width parameters given in Table 4, the parameter β can be computed in terms of the nonresonant self-broadening parameter β_0. For H_2O and CO_2, the resulting equations are, respectively:

$$\beta_{H_2O}(T) = \beta_0^{H_2O}(T)\, p \left[0.878 + 0.456\, c_{CO_2} + \left(0.122 + 4.89\sqrt{\frac{273}{T}}\right) c_{H_2O}\right] \tag{56}$$

$$\beta_{CO_2}(T) = \beta_0^{CO_2}(T)\, p \left[0.753 + 0.247\, c_{CO_2} + 0.0244\, c_{H_2O}\right] \tag{57}$$

where p is the total pressure in atmospheres and c_{CO_2} and c_{H_2O} are the mole fractions of CO_2 and H_2O respectively. For atmospheric paths, only the first term in the brackets is significant in each case. These terms are simply the inverse of the c-factors appearing in Eq. (55).

IV. COMPUTER CODE (ATLES)

A computer program has been generated to handle the computation of atmospheric transmittance to line emission sources. This code is called ATLES (Atmospheric Transmittance to Line Emission Sources) and is written in FORTRAN IV compatible with The Aerospace Corporation CDC 7600 computer and operating system. A simplified flow diagram for this program is shown in Fig. 9. The following listing is a brief discussion of each of the numbered blocks on the flow chart.

1. Each run of the program requires a set of data cards to control the calculational mode of the program. Pertinent data entered in this set include:
   a. The number of equal length intervals that the atmospheric path (NAPATH) and source path (NSPATH) are divided into for numerical integration over these paths.
   b. The type of source being viewed. (Present capability provides for a constant continuum source, a single line-of-sight path, and an axisymmetric cylindrical plume source. For the latter source, the number of intervals is also entered into which the axial and transverse coordinates of the projected area of the plume are divided for numerical integration over the plume.)
   c. The viewing geometry of the sensor/source configuration. (These data include sensor and source altitudes, zenith angles, and ranges as required.) A spherical earth geometry is used, but atmospheric refraction effects are not included.
   d. The spectral data for the minimum (ν_{min}) and maximum (ν_{max}) wave number and the number of spectral intervals (NSPEC) to be considered.
   e. A series of parameters that direct the program to read in new large blocks of data or to repeat the data used in the previous run (if there was one), and a set of parameters that direct the program to print out or suppress the printout at intermediate calculation stages.

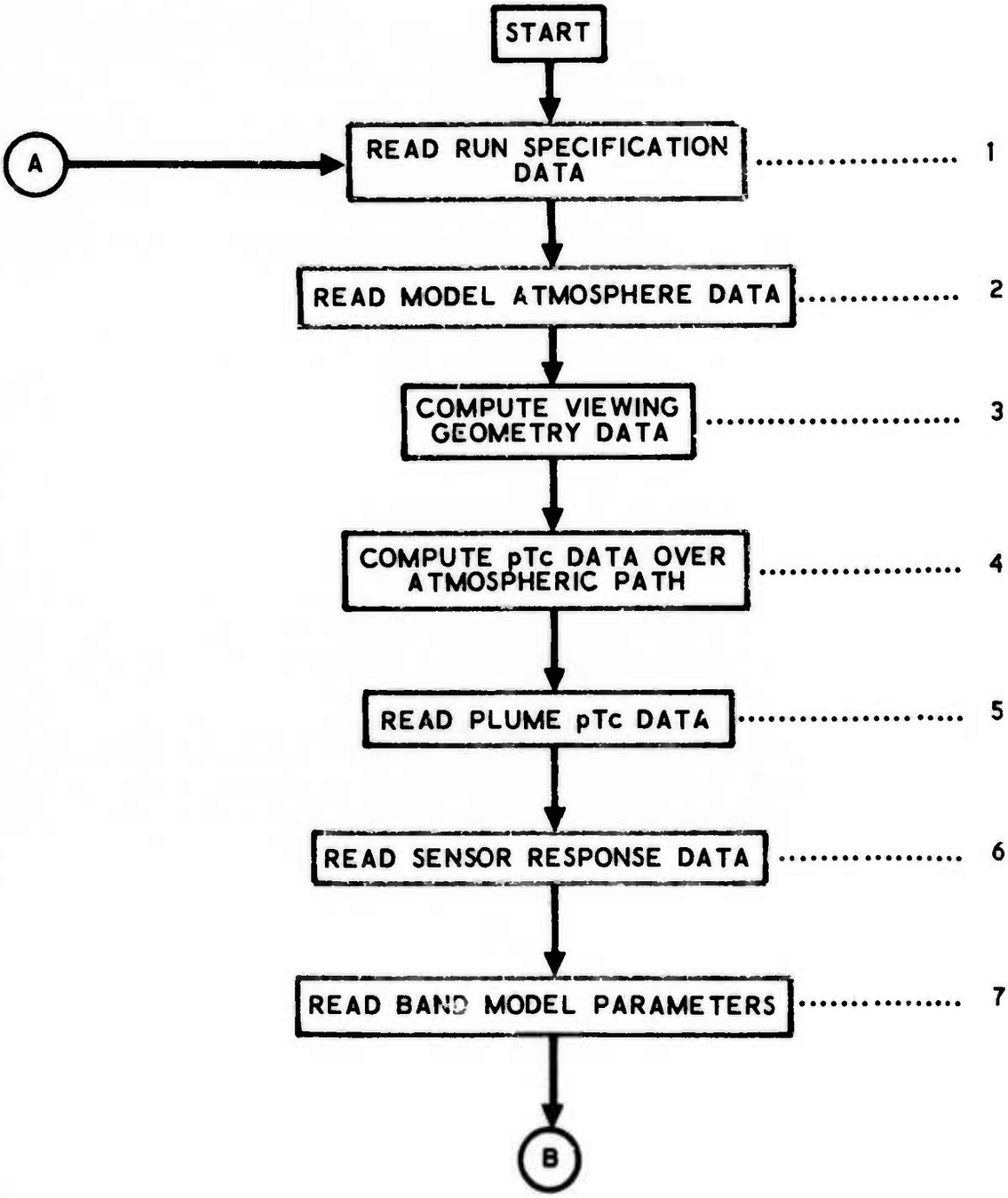

Fig. 9. Flow Diagram of ATLES Program

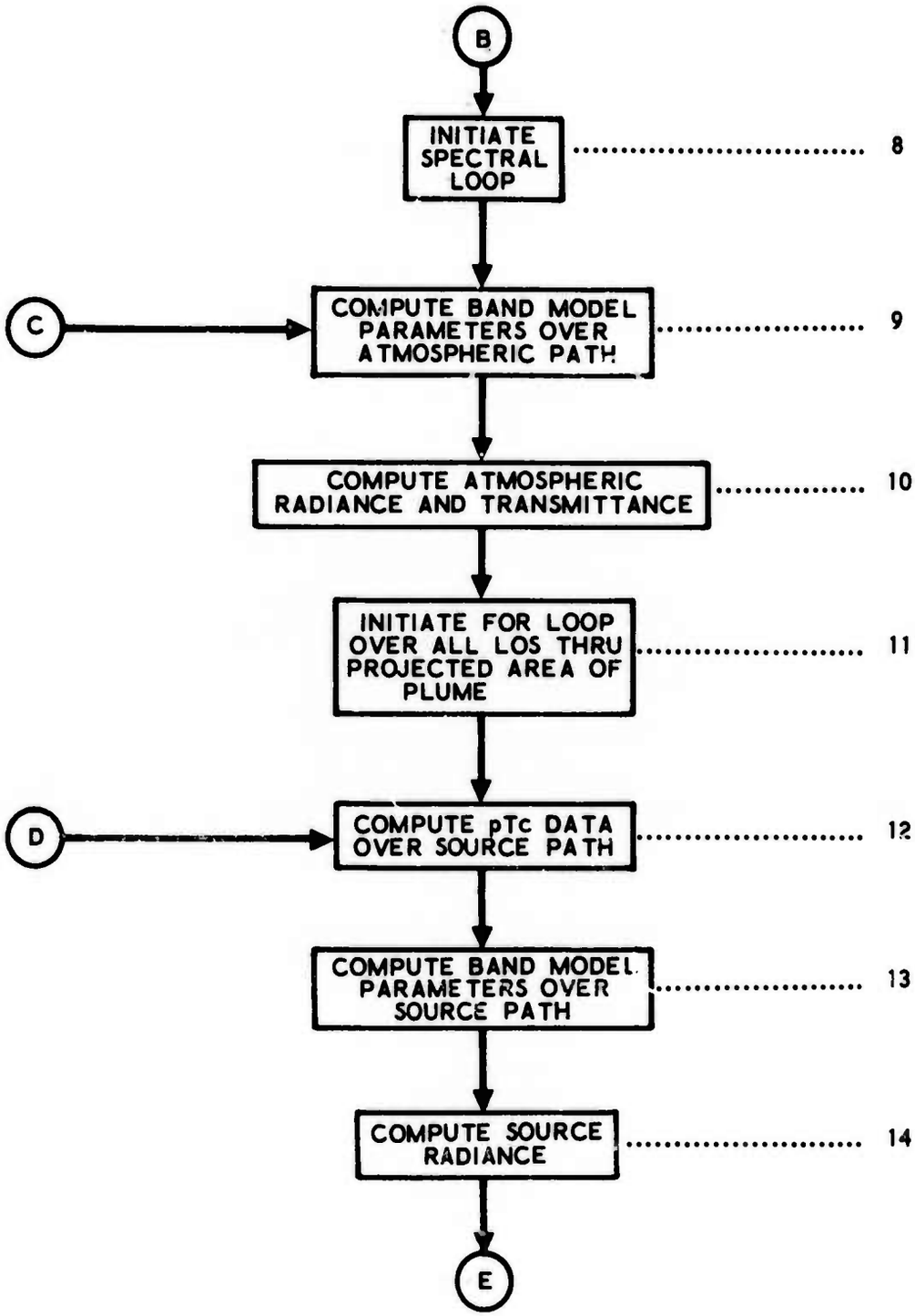

Fig. 9. Flow Diagram of ATLES Program (Continued)

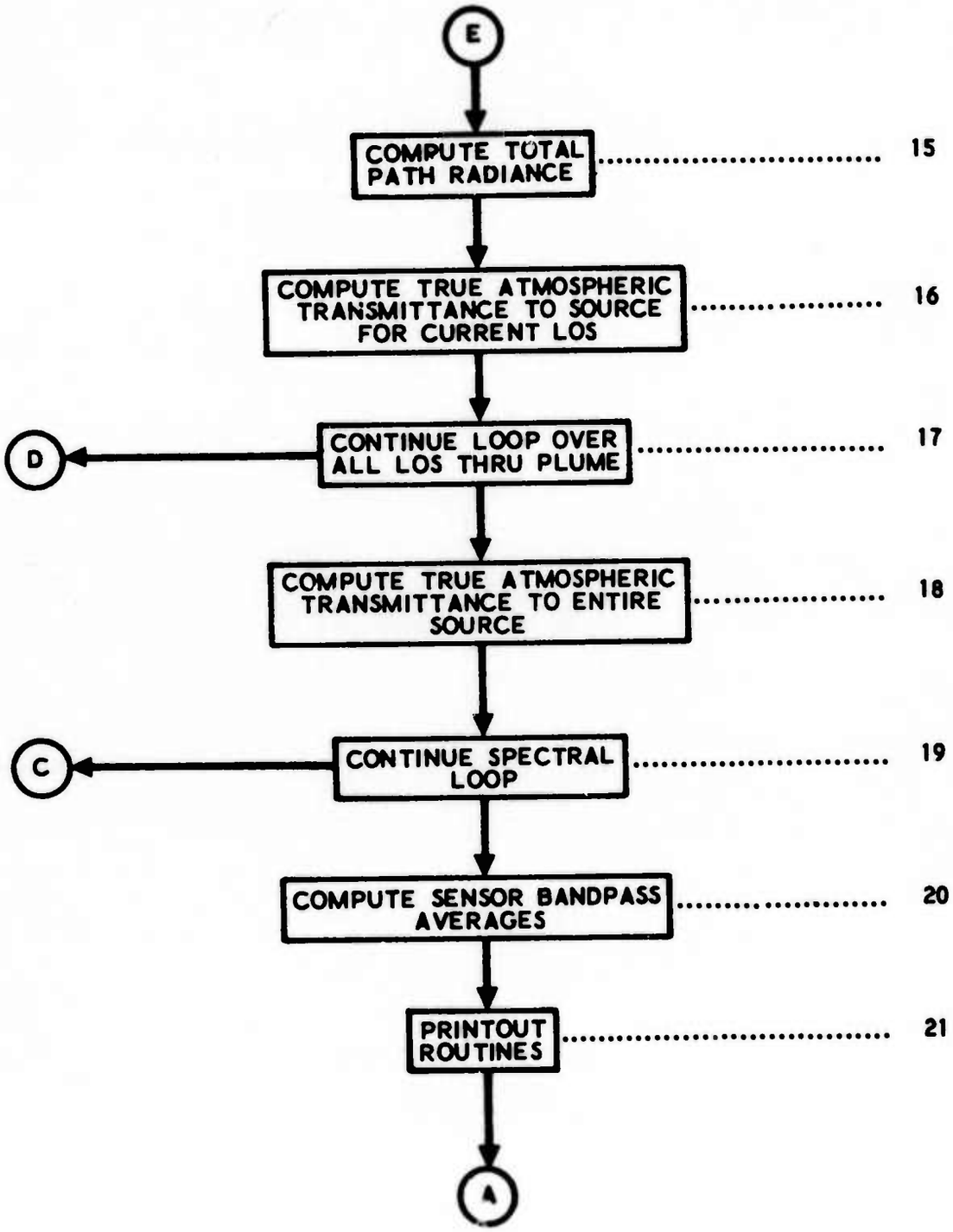

Fig. 9. Flow Diagram of ATLES Program (Concluded)

2. The data defining the model atmosphere to be used in the calculations are read in by subroutine MODATM. The format for these data provides for the entering of atmospheric pressure, temperature, H_2O concentration, and aerosol concentration at altitudes of 0, 1, 2, 3, . . . 24, 25, 30, 35, . . . 50, 70, and 100 km. This altitude format is consistent with the model atmospheres presented by McClatchey et al.,[7] that have been used for all computations. The McClatchey data are converted to units consistent with the operational units of the program. Pressure is converted from millibars to atmospheres via

$$p(\text{atm}) = \frac{p(\text{millibar})}{1.013 \times 10^3}$$

H_2O vapor concentration is converted from density in gm/m^3 to mole fraction via

$$c_{H_2O} = 4.559 \times 10^{-6} \frac{\rho_{H_2O}\ (gm/m^3)\ T(^\circ K)}{p(\text{atm})}$$

CO_2 concentration is set at $c_{CO_2} = 0.00033$.

The data entered at altitudes specified above are used to construct an altitude interpolation table with the thermodynamic variables given at each 1-km step between 0 and 100 km.

3. Subroutine VIEW uses the viewing geometry entered in Step 1 to compute the altitude variation along the line of sight from the sensor to the source at NAPATH + 1 equally spaced points along the path. Portions of a path above 100-km altitude (or an entered limit ZMAX) are not considered.

---

[7] R. A. McClatchey, R. W. Fenn, J. E. A. Selby, F. E. Volz, and J. S. Garing, Optical Properties of the Atmosphere (Revised), AFCRL-71-0279, Air Force Cambridge Research Laboratories, Mass. (10 May 1971).

4. Subroutine APATH uses the altitudes derived in Step 3 and the model atmosphere interpolation table set up in Step 1 to compute pressure, temperature, and concentrations (pTc data) at the NAPATH + 1 points along the atmospheric path.

5. This step is skipped if calculations for a constant continuum source are being made. If a single line of sight (LOS) is being considered, the pTc data at selected positions along the source path are read in by subroutine PLUME1. If a cylindrical plume is being considered, the pTc data at selected radial/axial grid points are read in by subroutine PLUME2. These data constitute interpolation arrays for subsequent calculations.

6. The sensor spectral response function is read in by subroutine SENSOR.

7. The band model parameters $\bar{k}$ and β_0 for both H_2O and CO_2 are read in by subroutine BAND. This set consists of a wave number array, a temperature array, and a two-dimensional array of $\bar{k}$ and β_0 for the temperature and wave numbers of the first two arrays. These data also constitute interpolation tables for subsequent calculations.

   A header card on this data block identifies the parameters so that conversion routines can be applied to the data to provide a set of parameters with consistent units. The standard unit for $\bar{k}$ is cm^{-1}/atm and the standard unit for β_0 is atm^{-1} for nonresonant self-broadening.

8. The ν_{min}, ν_{max} and NSPEC data entered in Step 1 are used to initiate a spectral loop over the NSPEC + 1 equally spaced wave numbers between ν_{min} and ν_{max}. If NSPEC = 0, calculations at ν_{min} only are performed.

9. From the temperature variation over the atmospheric path computed in Step 4 and the wave number set by Step 8, subroutine KBPATH computes $\bar{k}_{CO_2}$, $\beta_0{}^{CO_2}$, $\bar{k}_{H_2O}$, and $\beta_0{}^{H_2O}$ over the atmospheric path by interpolation on the data tables generated in Step 7. These β_0 values are further processed using the pTc data from Step 4 in subroutine BETA to yield the final band model parameter β at each point along the atmospheric path.

10. Using the $\overline{k}\beta$ values generated in Step 9 and with the pTc data of Step 4, subroutine DELTRAN computes the transmittance $\overline{\tau}_i$ and the transmittance derivative $d\overline{\tau}_i/ds$ along the atmospheric path for i = H_2O and CO_2 individually in both the Curtis-Godson and Lindquist-Simmons approximations. The function $y(x,\rho)$ required in the Lindquist-Simmons approximation is computed in the function subprogram YLS. The transmittance variables are then used in subroutine RADNCE to compute the radiance of the atmospheric path. Subroutine RADNCE also returns the path ending values of the total transmittance $\overline{\tau}H_2O \times \overline{\tau}CO_2$, which is the atmospheric transmittance appropriate for a constant continuum source.

11. If a constant continuum source is being considered, a skip to Step 19 now takes place. Otherwise, subroutine SGRID is called. This subroutine calculates the appropriate looping parameters required to effect a two-dimensional integration loop over the projected area of a cylindrical source plume. For each LOS passing through the plume, Steps 12 through 17 are performed. If only a single LOS is being considered, the loop is gone through just once.

12. Using the looping parameters from Step 11 and the viewing geometry data read in at Step 1 (principally, the viewing aspect angle), subroutine SPATH2: (a) computes the geometry of intersection between the LOS and the plume, (b) computes the axial and radial coordinates (in the coordinate system of the plume) for each of NSPATH + 1 equally spaced points along the portion of the LOS within the plume, and (c) uses these axial/radial parameters to effect an interpolation on the pTc data table read in by subroutine PLUME2 (Step 5) to arrive at the pTc variation over the source path.

13. This step computes the $\overline{k}\beta$ parameters over the established source path in the same manner as these parameters were evaluated for the atmospheric path except that the pTc data from Step 12 are used.

14. Again, this step is similar to the calculations of Step 10 except that the data appropriate to the source path are used.

15. Step 14 computes the radiation characteristics over the source path portion of the LOS only. In Step 15, the radiation properties of the total path (i.e., the combined atmospheric path plus source path) are computed. This step is essentially the same as Step 14 except that different

initial conditions at the source path starting point are imposed. These initial conditions are, in fact, the ending path conditions computed for the atmospheric path in Step 10. The imposition of these conditions accounts for the absorption effects of the intervening atmosphere. The atmospheric contribution to the total radiance could be accounted for by adding the source path radiance computed with these initial conditions to the atmospheric path radiance computed in Step 10. In practice, the atmospheric radiance from Step 10 is not included in the total path radiance. The atmospheric radiance calculation accounts for only the atmospheric path between the sensor and the source. Thus, inclusion of this term would represent an incomplete account of the atmospheric radiance since the contributions from the atmospheric path beyond the source (and also any other background beyond the source) would not be included. The complete neglect of the atmospheric radiance contributions to the total path radiance makes the calculated results analogous to (and comparable with) experimental measurements for which background signals have been subtracted.

16. The true atmospheric transmittance for the source path defined for the current LOS is computed by dividing the total path radiance (minus the atmospheric and background contributions) computed in Step 15 by the source path radiance computed in Step 14.

17. The loop over all LOS through the projected area of the plume is continued. Within this loop, an integration over the entire projected area of the plume is effected to arrive at the total source and sensor radiance.

18. The effective atmospheric transmittance of the entire source is computed by dividing the total source radiance by the total sensor radiance.

19. The loop over all wave numbers between ν_{min} and ν_{max} is continued.

20. The generated spectral transmittance and radiance data are averaged over the sensor response function read in by subroutine SENSOR. This averaging is performed by subroutine BNDPASS. Bandpass transmittances for line emission sources are computed by dividing bandpass averaged radiances and <u>not</u> by averaging the computed spectral transmittance. The bandpass averaged transmittance for a continuum source <u>is</u> computed by averaging the spectral transmittance.

21. A final summary of the various spectral radiance and transmittance calculations, bandpass averages, and input data identification codes is printed out. An option allows for a punched deck output for use in plotting routines.

All of the input data and the results of the computations at each major computation step can be printed out at option. Such printouts are indispensable for program checkout and detailed analysis of selected runs. In the normal operating mode, however, these printouts are suppressed as many of them are located within imbedded loops and would involve unmanageable volumes of paper.

As presently written, this code should be considered primarily as a research tool. It was written to enable the analysis of the many facets of the general problem of transmittance calculation. The general calculational approach is geared to this purpose rather than to the efficient calculation that would be required for a production analysis tool, although this code is certainly much more efficient than codes performing high-resolution monochromatic calculations. Because of this approach, the code is generally in a state of continual modification, but only minor future modifications (e.g., input/output formats) are envisioned. Because of this, a detailed description and listing of the code have not been included.

V. RESULTS AND DISCUSSIONS

A. HOMOGENEOUS PATHS

Comparisons of band model spectra and experimental spectra for homogeneous hot gas optical paths were made in order to assess the degree of accuracy with which the LINAVE parameters (computed from the AFCRL atmospheric line atlas) could predict hot gas spectra. Comparisons were made with an experimental CO_2 spectrum of Burch and Gryvnak,[8] a CO_2 spectrum of Simmons et al.,[9] and an H_2O spectrum of Simmons et al.[10] The experimental conditions appropriate to these three spectra are listed in Table 5.

Table 5. Homogeneous Hot Gas Spectra Experimental Conditions

Reference	Gas	p (atm)	T (°K)	L (cm)
Burch and Gryvnak[8]	pure CO_2	0.997	1200	7.75
Simmons et al.[9]	pure CO_2	2.03	1146	60
Simmons et al.[10]	pure H_2O	0.937	1040	60

[8] D. E. Burch and D. A. Gryvnak, Infrared Radiation Emitted by Hot Gases and Its Transmission Through Synthetic Atmospheres, U-1929, Aeronutronic Division, Ford Motor Company, Newport Beach, Calif. (31 October 1962).

[9] F. S. Simmons, H. Y. Yamada, and C. B. Arnold, Measurement of Temperature Profiles in Hot Gases by Emission-Absorption Spectroscopy, NASA CR-72491, National Aeronautics and Space Administration (April 1969).

[10] F. S. Simmons, C. B. Arnold, and D. H. Smith, Studies of Infrared Radiative Transfer in Hot Gases, I: Spectral Absorptance Measurements in the 2.7μ H_2O Bands, 4613-91-T, Willow Run Laboratories (August 1965).

Results for the CO_2 spectrum of Burch and Gryvnak[8] are illustrated in Fig. 10. The band model results shown in Fig. 10(a) were computed with LINAVE parameters generated for a resolution of 25 cm^{-1} and at wave number steps of 25 cm^{-1}. The results given in Fig. 10(b) were generated with parameters of the same resolution but at steps of only 5 cm^{-1}. Comparison of the experimental result with the band model result computed with the General Dynamics band model parameters has been discussed by Ludwig et al.[2] Agreement of the experimental spectrum with those computed using the LINAVE parameters is surprisingly good; between 3550 and 3800 cm^{-1} (the band center), the degree of agreement is about as good as that obtained using the General Dynamics parameters. In the wing region below approximately 3450 cm^{-1}, however, the results for the LINAVE parameters fall seriously short of the experimental curve. Comparison with the CO_2 spectrum of Simmons et al.[9] (Fig. 11) displays the same features just discussed, particularly the vast underestimating of the radiance in the wing region by the band model results using the LINAVE parameters. (Note that the actual experimental curve is not shown in Fig. 11 since it is negligibly different from the band model results obtained using the General Dynamics parameters.) The most probable explanation, as mentioned earlier in paragraph III.C, is the lack of inclusion of hot line data in the AFCRL line compilation.

Comparisons of the band model results computed with the LINAVE2 parameters and the results obtained from a monochromatic line-by-line calculation[11] for these two CO_2 spectra are presented in Figs. 10(b) and 11(b). The line-by-line results were computed on a spectral scale of 0.02 cm^{-1} and then convoluted with a 20-cm^{-1}-wide rectangular slit function for comparison with the band model results. Line data required for the monochromatic calculations were obtained from the same data set[6] from

---

[11] C. M. Randall, Monochromatic Transmittance/Radiance Computations, TR-0075(5647)-3, The Aerospace Corporation, El Segundo, Calif. (31 December 1974).

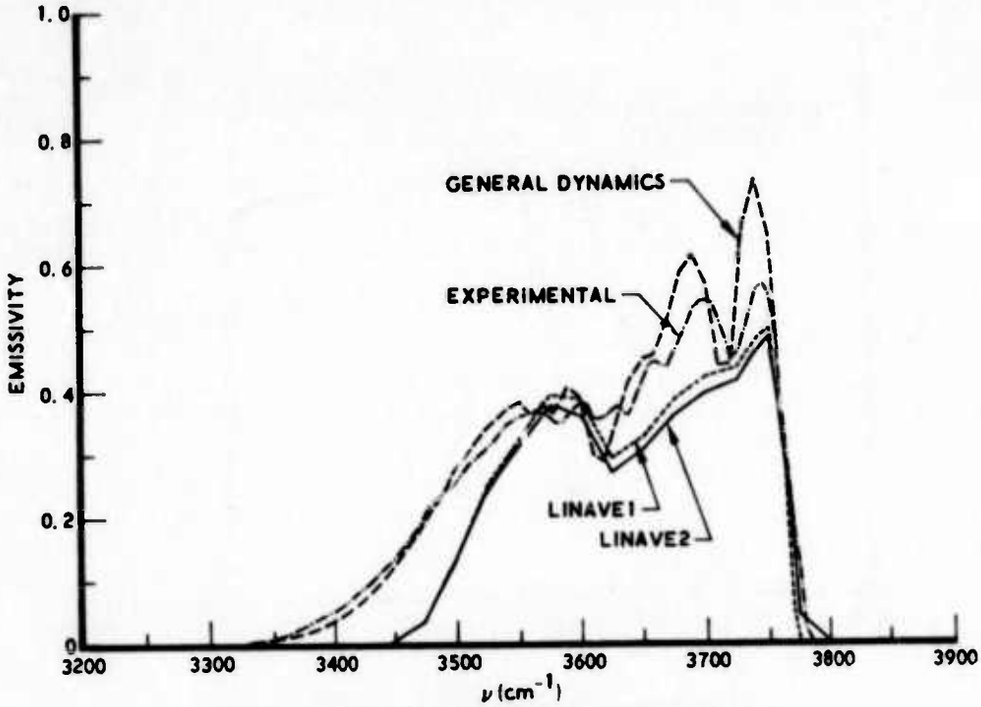

(a) Comparison of Band Model and Experiment Results

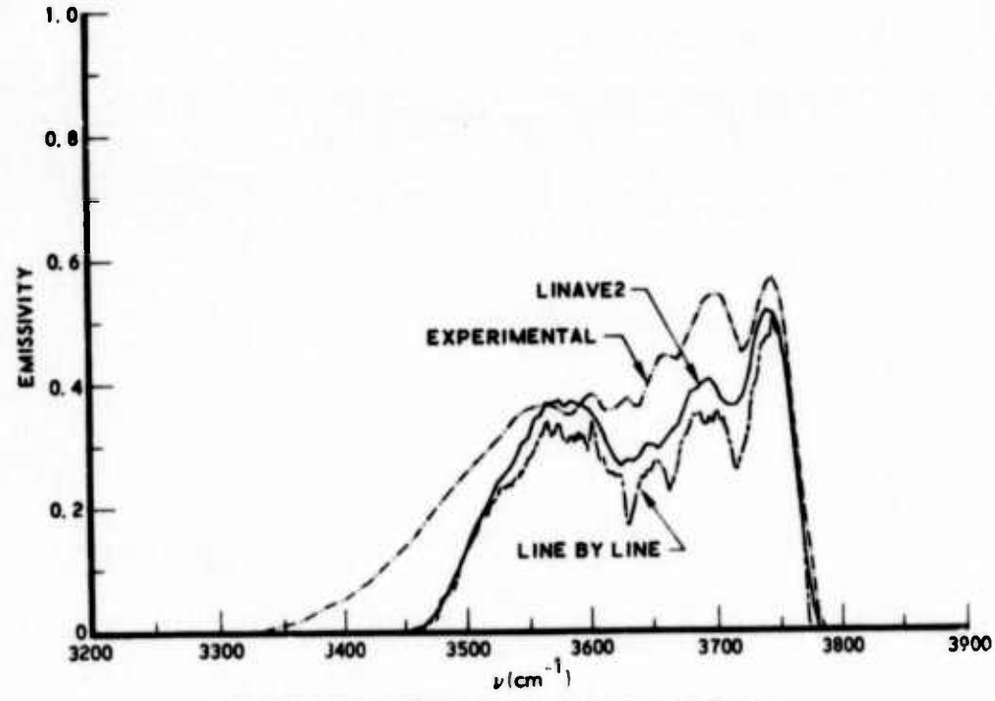

(b) Comparison of Band Model and Line by Line Results

Fig. 10. Comparisons of Band Model, Line-by-Line,[8] and Experimental Results of Burch and Gryvnak for CO_2

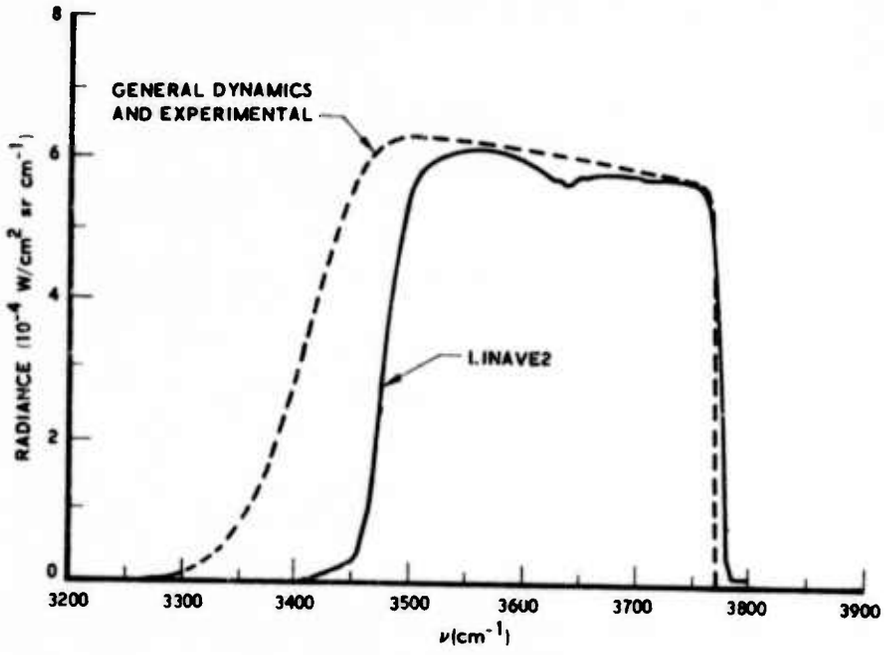

(a) Comparison of LINAVE2 Results with General Dynamics Results and Experiment

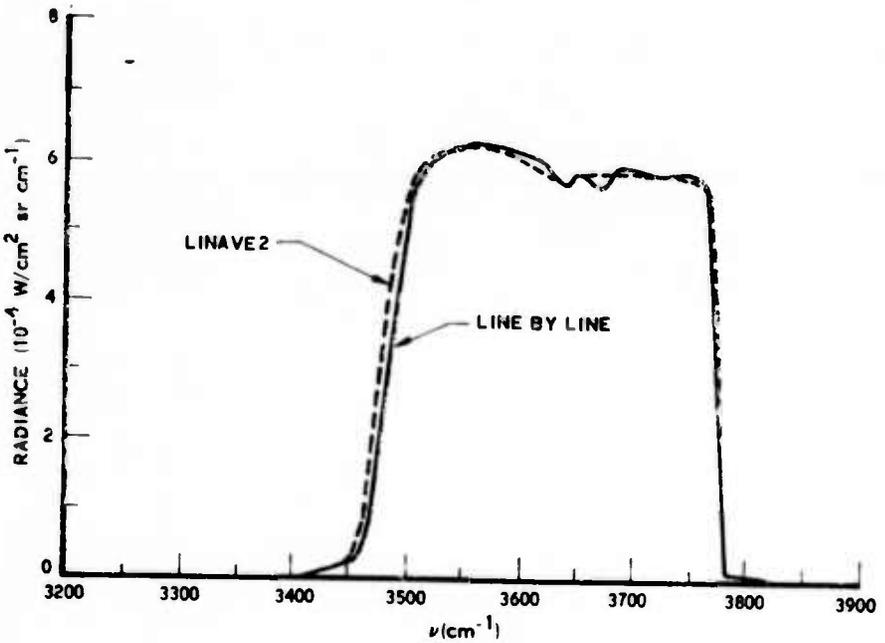

(b) Comparison of LINAVE2 Results with Line by Line Results

Fig. 11. Comparisons of Band Model, Line-by-Line, and Experimental Results of Simmons et al.[9] for CO_2

which the LINAVE band model parameters were derived. Although agreement between the band model and line-by-line spectra is quite good, the band model results do yield a consistently higher degree of absorptance. Two causes may be responsible for this effect. First, the constant line intensity distribution used within the statistical band model is the distribution that results in the most absorption. If the intensity distribution were altered to allow more weak lines (e.g., an exponential distribution), the absorptance would become less[2] and agreement with the line-by-line results would become better. Although the alteration of the intensity distribution to allow weak lines increases the number of strong lines also (so that the mean line strength remains constant), the reduced absorption by the weak lines outweighs the increased absorption of the strong lines. In reference to the choice of band model, note that the statistical band model, regardless of intensity distribution, is generally not applied to CO_2 absorption. Most often, a regular line spacing model (e.g., the Elsasser model) is applied.[1] However, since the regular model does not allow for the possibility of large gaps between lines (as is allowed in the statistical model), the absorptance for the regular model is greater than that given by the statistical model. Thus, the use of a regular line spacing model would lessen the agreement with the line-by-line results.

Secondly, the line-by-line results are computed in a procedure whereby the exact monochromatic transmittance is first computed and then averaged (convolved with the slit function) over a spectral region $\Delta\nu$. The band model approach, on the other hand, first performs the averaging procedure within $\Delta\nu$ (the generation of the band model parameters) and then generates the transmittance spectrum. There is no reason to believe that the two mathematical operations of generating the spectrum and averaging are commutative.

The comparison of the band model calculations using the LINAVE parameters and the H_2O spectrum of Simmons et al.[10] is shown in Fig. 12. The band model parameters were calculated for a 25-cm^{-1} resolution and

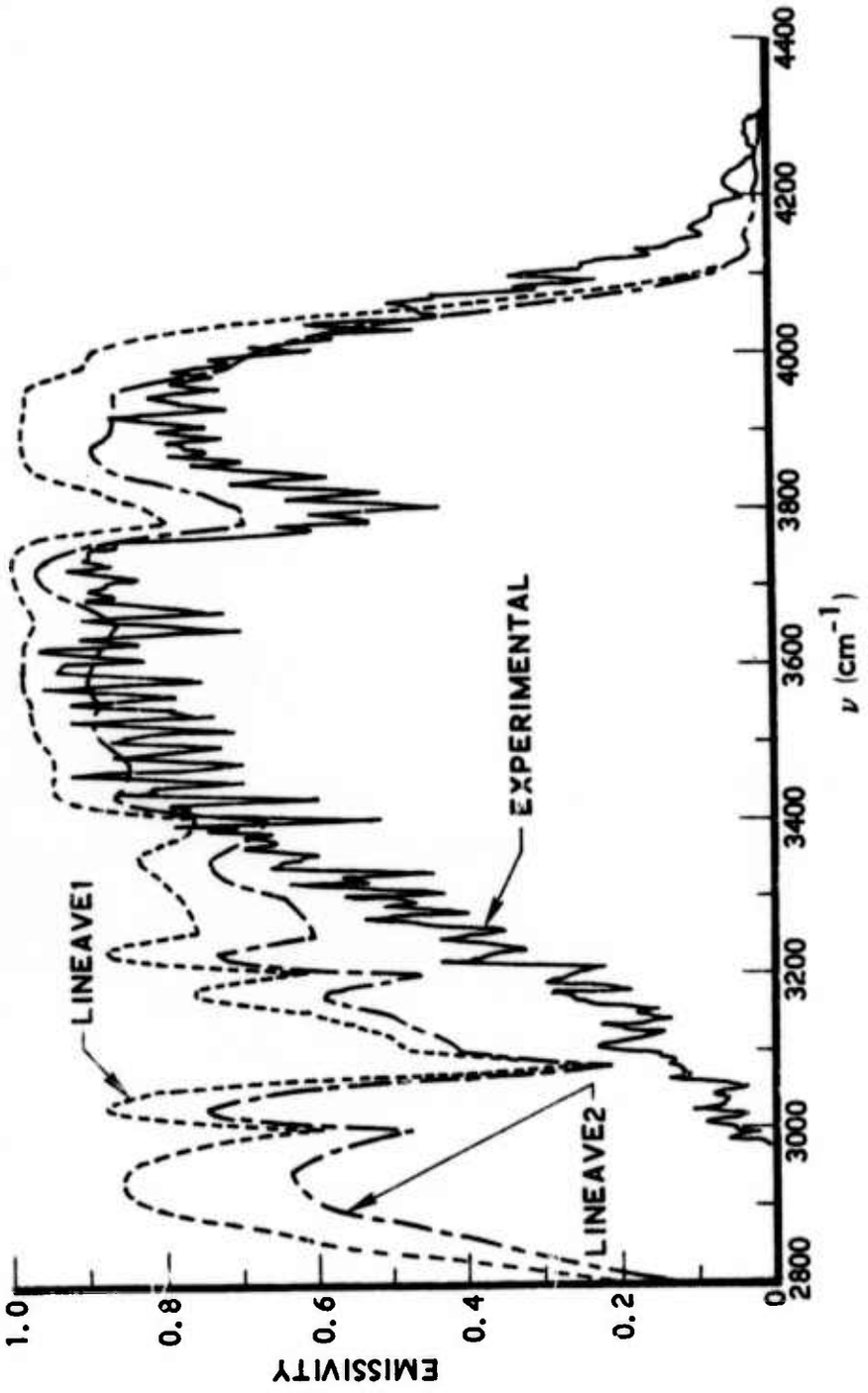

Fig. 12. Comparison of Band Model Results Using LINAVE Parameters and Experimental Results of Simmons et al.[10] for H_2O

at steps of 25 cm^{-1}. Agreement of the results for the LINAVE2 parameters and the experimental result is quite good above about 3400 cm^{-1}. However, agreement of the results for the LINAVE1 parameters is less marked. The biggest apparent discrepancy between the emissivity results computed using the LINAVE1 and LINAVE2 parameters occurs for those conditions where the optical path is not thin ($\epsilon \gtrsim 0.2$) but is not large enough to force the emissivity in either calculation to unity. Since most of this H_2O spectrum is not thin, the LINAVE2 parameters would be expected to yield the better results since these parameters were derived to give the correct answer in the strong line limit. For both CO_2 and H_2O, the LINAVE2 parameters are used throughout the remainder of the calculations presented in this report. Results of the band model calculation using a LINAVE2 parameter set computed for a resolution of 25 cm^{-1}, but at steps of only 5 cm^{-1}, is shown in Fig. 13 along with the experimental spectrum and the band model result obtained using the General Dynamics parameters.

The most surprising result obtained for the H_2O comparison is the very large discrepancy occurring in the band model calculations using the LINAVE parameters for the wing region below 3300 cm^{-1}. This result can be traceable only to the fundamental line data from which the LINAVE parameters were derived, a conclusion that is confirmed by the nearly monochromatic line-by-line result shown in Fig. 14. This spectrum was computed[11] from the same basic line data from which the LINAVE parameters were derived and also shows the enhanced features in the wing. The error in the line data tabulation in this case is obviously not an omission of lines (as for CO_2) but either an inclusion of lines that do not belong or an error in the data for lines that do occur there. Fortunately, for most of the work of concern in this report, only the spectral region above 3300 cm^{-1} is important. The LINAVE2 parameters can thus be considered to be reasonably accurate up to at least 1050°K.

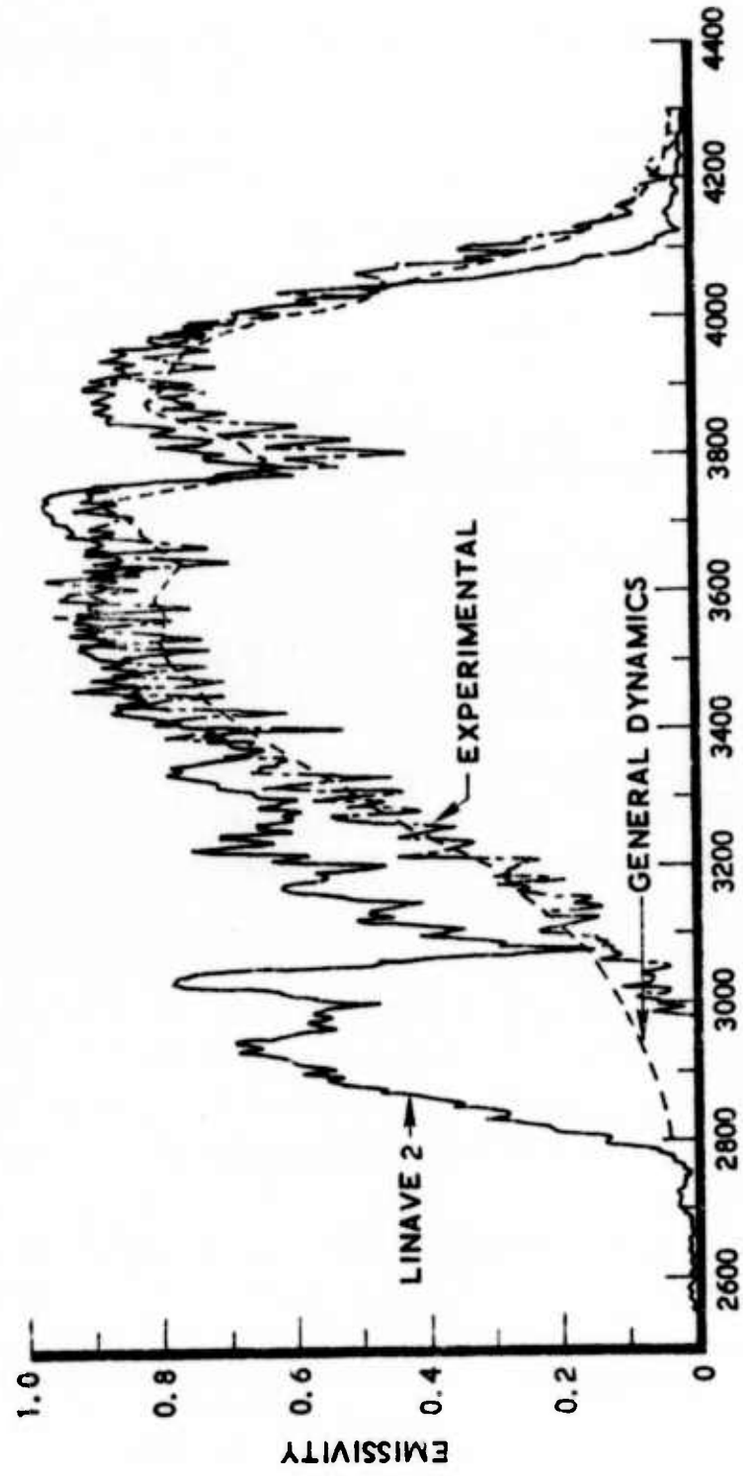

Fig. 13. Comparison of Band Model Results and Experimental Results of Simmons et al.[10] for H_2O

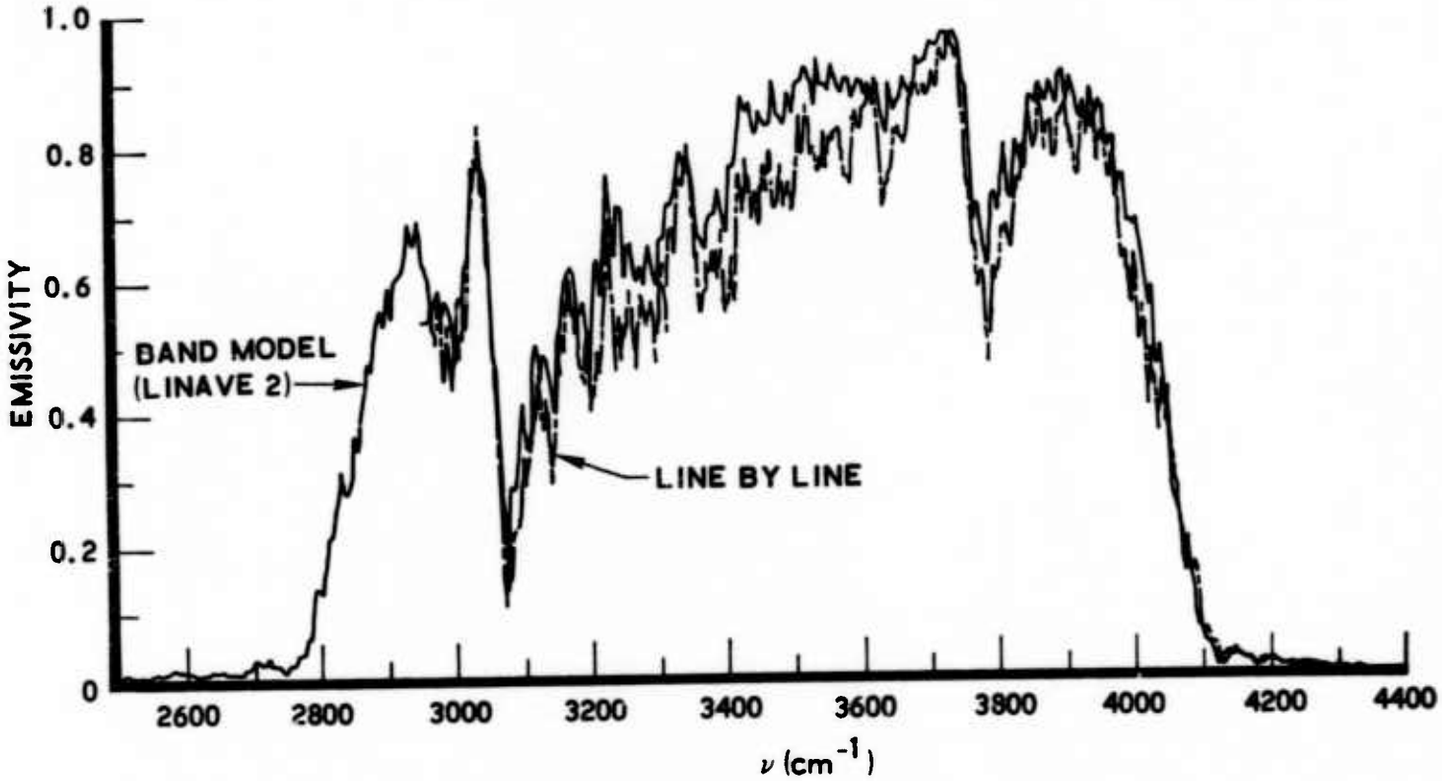

Fig. 14. Comparison of Band Model Results Using LINAVE2 Parameters and Monochromatic Line-by-Line Results for the Experimental Conditions of Simmons et al.[10] H_2O Spectrum

Figure 14 contains a comparison of the band model calculations and the nearly monochromatic line-by-line calculations for the H_2O spectrum. As in the case for CO_2, the band model calculation yields a consistently higher degree of absorptance than does the line-by-line calculation. The discussion of this effect given for CO_2 applies here also. A confirmation of the better agreement that would exist for a band model employing a line intensity distribution that allows weak lines is given by the work of Goldman and Kyle.[12] Agreement to better than 5 percent between monochromatic line-by-line calculations and band model calculations employing an exponential-tailed, inverse line strength distribution was achieved by these workers.

B. ATMOSPHERIC SLANT PATHS

Detailed calculations for the radiative transfer along two atmospheric paths representative of geometries appropriate to satellite-borne and aircraft-borne sensor measurements programs were performed. The path appropriate for a space sensor geometry extends from the source altitude of 20 km to space at a zenith angle of 75 deg. The path appropriate to aircraft-borne sensor field measurements programs consists of a 100-km-long horizontal path situated at an altitude of 20 km. The hot gas target source used for these calculations was based on a right circular cylinder, homogeneous and isothermal plume model given by Thomas.* The plume dimensions, temperature, and species concentrations for plume altitudes between 1 and 60 km are listed in Table 6. For the source altitude of 20 km, L = 238 m, r = 3.87 m, T = 1250°K, $c_{H_2O} = 0.253$, and $c_{CO_2} = 0.0371$. The tropical atmospheric model given by McClatchey[7] was used in these calculations. This atmosphere is listed in Table 7. Results were calculated using both the LINAVE2 band model parameter set ($\Delta\nu$ = 25 cm^{-1}, step size = 5 cm^{-1}) and the General Dynamics parameter set.

*D. D. Thomas, The Aerospace Corporation, private communication, 1974.

[12] A. Goldman and T. G. Kyle, "A Comparison between Statistical Model and Line-by-Line Calculations with Application to the 9.6μ Ozone and the 2.7μ Water Vapor Bands," Applied Optics 7, 1167 (1968).

Table 6. Homogeneous and Isothermal Plume Model

z (km)	r (m)	L (m)	p (atm)	T (°K)	c_{H_2O}	c_{CO_2}
1	1.534	20.50	0.8924	2139.0	0.2533	0.03714
5	1.718	37.64	0.5518	1867.4		
10	2.170	71.35	0.2823	1625.2		
15	2.870	133.9	0.1303	1417.8		
20	3.865	237.9	0.05577	1249.4		
25	5.197	409.5	0.02537	1107.1		
30	6.897	704.1	0.01204	975.8		
35	8.918	1.260(3)	5.923(-3)	844.4		
40	11.29	2.237(3)	3.011(-3)	723.5		
45	14.09	3.789(3)	1.570(-3)	622.5		
50	17.54	5.944(3)	8.430(-4)	545.6		
55	22.46	9.817(3)	4.574(-4)	478.7		
60	29.41	1.444(4)	2.382(-4)	441.5		

z = source altitude

r = plume radius

L = plume length

p = pressure (ambient atmospheric at z)

T = plume temperature

c_{H_2O} = H_2O mole fraction

c_{CO_2} = CO_2 mole fraction

Table 7. Model Tropical Atmosphere[7]

Altitude (km)	Pressure (atm)	Temperature (°K)	$^{c}H_2O$
0	1.0000	300.0	2.599(-2)
1	0.8924	294.0	1.953(-2)
2	0.7947	288.0	1.537(-2)
3	0.7058	284.0	8.624(-3)
4	0.6249	277.0	4.447(-3)
5	0.5518	270.0	3.347(-3)
6	0.4857	264.0	2.107(-3)
7	0.4265	257.0	1.292(-3)
8	0.3731	250.0	7.638(-4)
9	0.3248	244.0	4.111(-4)
10	0.2823	237.0	1.914(-4)
11	0.2438	230.0	7.312(-5)
12	0.2103	224.0	2.915(-5)
13	0.1797	217.0	9.914(-6)
14	0.1540	210.0	6.218(-6)
15	0.1303	204.0	5.426(-6)
16	0.1096	197.0	5.247(-6)
17	9.250(-2)	195.0	5.383(-6)
18	7.789(-2)	199.0	5.825(-6)
19	6.575(-2)	203.0	6.899(-6)
20	5.577(-2)	207.0	7.616(-6)
21	4.738(-2)	211.0	1.036(-5)
22	4.038(-2)	215.0	1.238(-5)
23	3.455(-2)	217.0	1.547(-5)
24	2.962(-2)	219.0	2.023(-5)
25	2.537(-2)	221.0	2.661(-5)
30	1.204(-2)	232.0	3.162(-5)
35	5.923(-3)	243.0	2.058(-5)
40	3.011(-3)	254.0	1.654(-5)
45	1.507(-3)	265.0	1.463(-5)
50	8.430(-4)	270.0	9.201(-6)
70	5.716(-5)	219.0	2.446(-5)
100	2.962(-7)	210.0	3.244(-5)

The radiance spectra computed for the homogeneous source alone and for the sensor position are plotted in Figs. 15 and 16 for the slant path and horizontal path respectively. These radiance spectra as well as all the results presented in Figs. 15 through 24 were computed for a single line of sight that intersects the equivalent cylindrical plume at a 90-deg aspect angle (measured from nose-on) and at the full diameter position. Thus, the source is a simple homogeneous path $2r = 774$ cm in length.

For the LINAVE2 parameters, the sensor radiance spectra computed using the CG and the LS approximations are nearly identical. The reason for this result is that the LINAVE2 parameters do not produce a serious inhomogeneity when passing from the cool atmosphere (~200°K) into the hot source (~1200°K). It may be seen from Fig. 6 that for CO_2 at 3700 cm^{-1}, ρ would in fact obtain a value of only about 3 during the transition, and for H_2O (Fig. 8), ρ changes very little during the transition. For the General Dynamics parameters, on the other hand, the difference in the results when using the CG approximation or the LS approximation is dramatically evident. Here, the variation of the band model parameter β (see Figs. 6 and 8) with temperature is rapid enough to provide a very strong inhomogeneity during the transition from the atmosphere into the source ($\rho \simeq 100$ for CO_2 and $\rho \simeq 5$ for H_2O). The serious breakdown of the CG approximation is evident in its prediction of a sensor radiance that is larger than the source radiance itself at some spectral positions. This physically impossible result does not occur in the LS approximation.

Results for the atmospheric transmittance $\bar{\tau}$ appropriate for a continuum emission source are presented in Figs. 17 and 18 for the slant and horizontal atmospheric paths respectively. Comparisons are shown of the band model results generated using the LINAVE2 parameters and the General Dynamics parameters as well as results computed on a monochromatic line-by-line basis[11] and results obtained using the LOWTRAN band

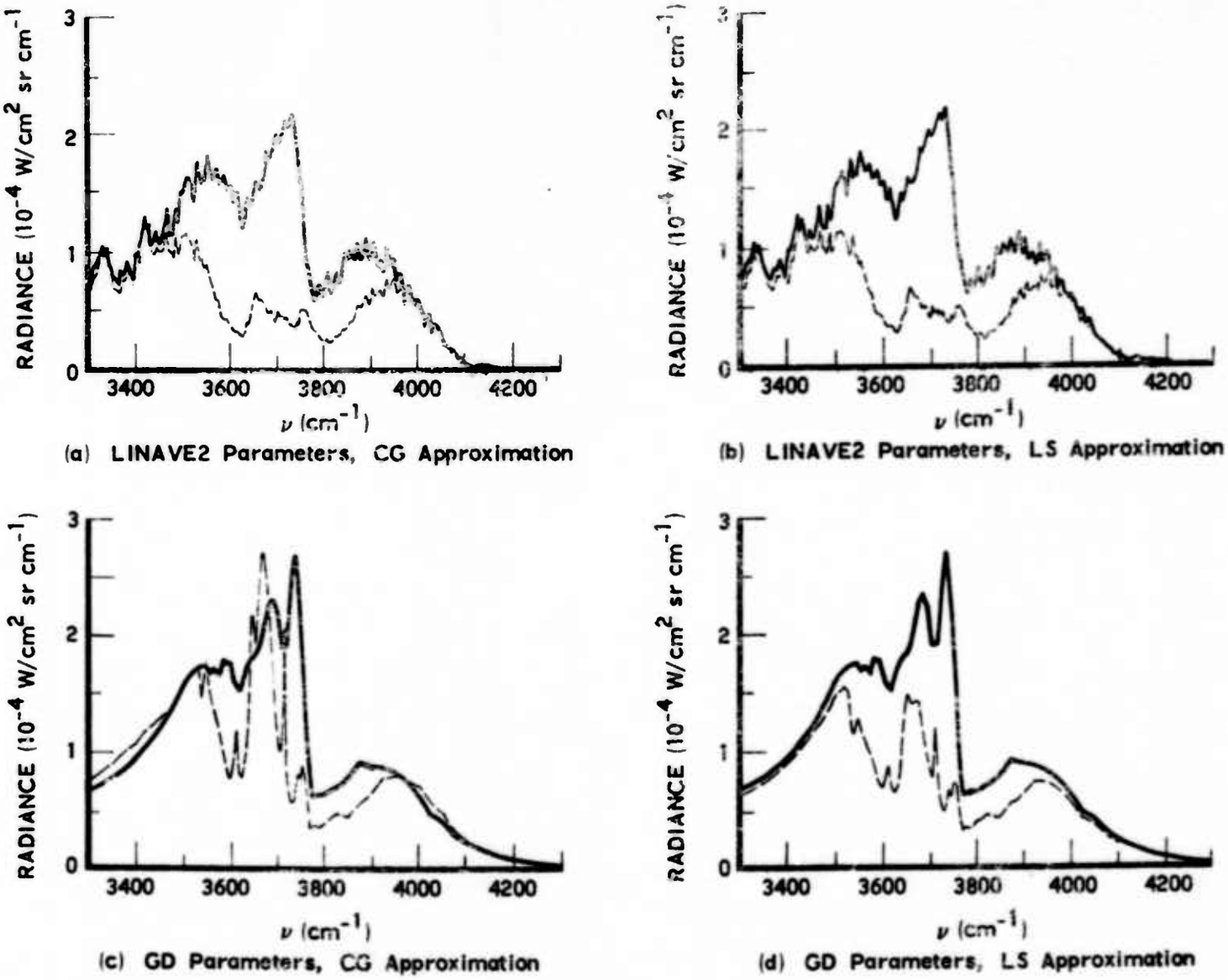

Fig. 15. Source and Sensor Radiances for Slant Path

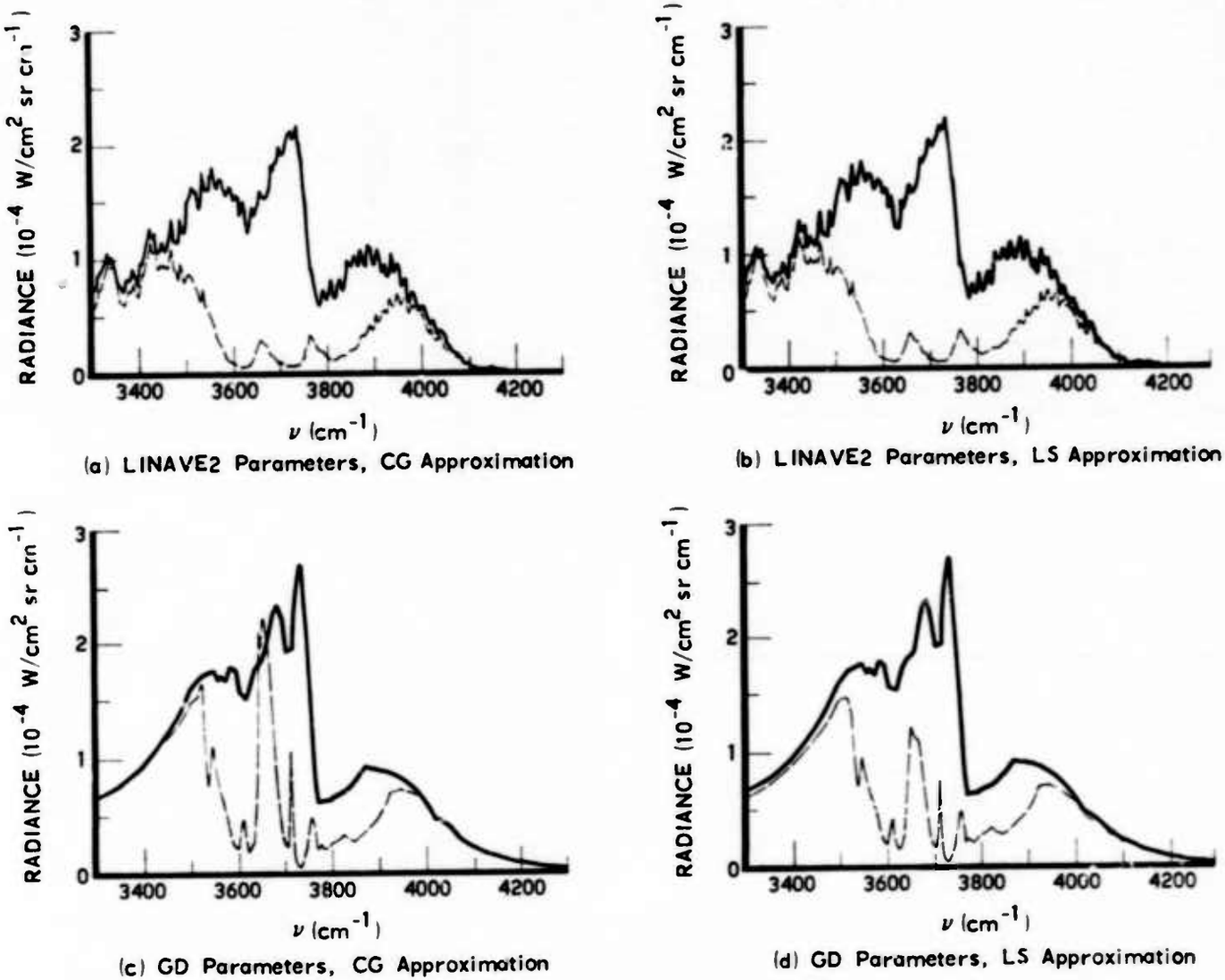

Fig. 16. Source and Sensor Radiances for Horizontal Path

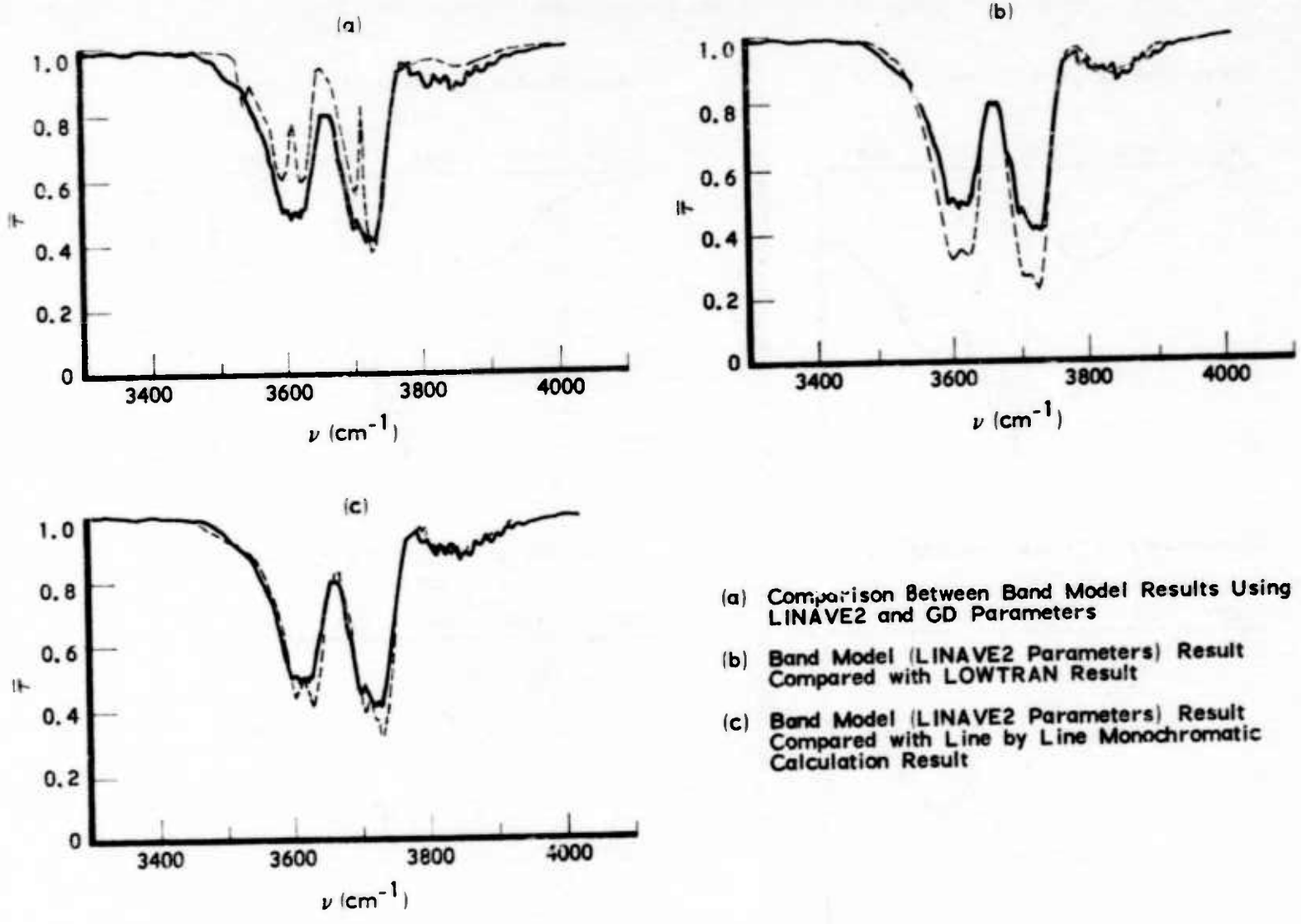

(a) Comparison Between Band Model Results Using LINAVE2 and GD Parameters

(b) Band Model (LINAVE2 Parameters) Result Compared with LOWTRAN Result

(c) Band Model (LINAVE2 Parameters) Result Compared with Line by Line Monochromatic Calculation Result

Fig. 17. Comparison of T Results for Slant Path

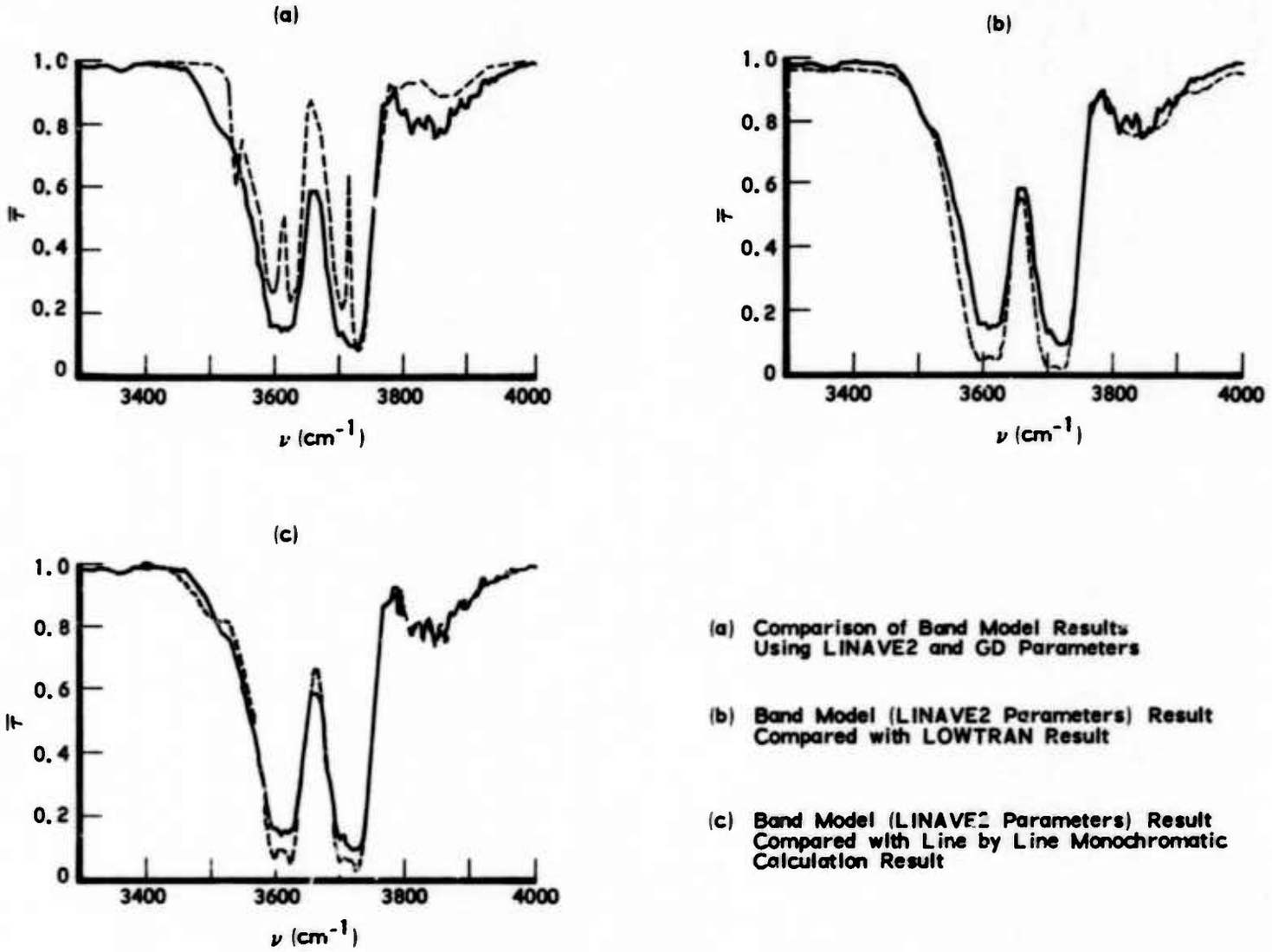

(a) Comparison of Band Model Results Using LINAVE2 and GD Parameters

(b) Band Model (LINAVE2 Parameters) Result Compared with LOWTRAN Result

(c) Band Model (LINAVE2 Parameters) Result Compared with Line by Line Monochromatic Calculation Result

Fig. 18. Comparison of $\bar{\tau}$ Results for Horizontal Path

model[13] routine. In general, the results obtained with the LINAVE2 parameters, the line-by-line calculations, and the LOWTRAN Program agree quite well. The causes of some of the differences that do occur between the LINAVE2 band model results and the line-by-line results, particularly in the regions of strongest absorption, are probably the same as those responsible for the discrepancies in the homogeneous path spectra discussed in paragraph V.A. Another possible cause lies in the fact that the band model results were performed under conditions for which necessary numerical integrations along the optical path were confirmed to be accurate (see paragraph V.C). However, for the sake of reducing computer processing time, the line-by-line calculations were performed by dividing the atmosphere into only 5 to 10 equivalent homogeneous layers. This number of layers may not be sufficient to obtain high accuracy for the path integration portions of the calculations.

Comparisons of $\bar{\tau}$ and the transmittance appropriate to the attenuation of hot gas line emission $\bar{\tau}_e$ are shown in Figs. 19 through 22. The large difference between $\bar{\tau}$ and $\bar{\tau}_e$ caused by the effect of line correlation between the emission and absorption spectra is evident in all cases. A transmittance ratio of nearly 4 is displayed at 3850 cm^{-1} for the horizontal path. The largest differences between $\bar{\tau}$ and $\bar{\tau}_e$ generally occur in the regions of strongest absorption. As was the case for $\bar{\tau}$, the difference in $\bar{\tau}_e$ between calculations involving the CG and LS approximations is very small when the LINAVE2 parameters are employed. When the General Dynamics parameters are used, however, the LS approximation yields a decidedly more realistic result. The breakdown of the CG approximation is manifested by yielding effective atmospheric transmittance values ($\bar{\tau}_e$) greater than unity. The spectral regions of breakdown are regions of small absorption. This is just

[13] J. E. A. Selby, Atmospheric Transmittance from 0.25 to 28.5 μm: Computer Code LOWTRAN2, AFCRL-72-0745, Air Force Cambridge Research Laboratories, Mass. (29 December 1972).

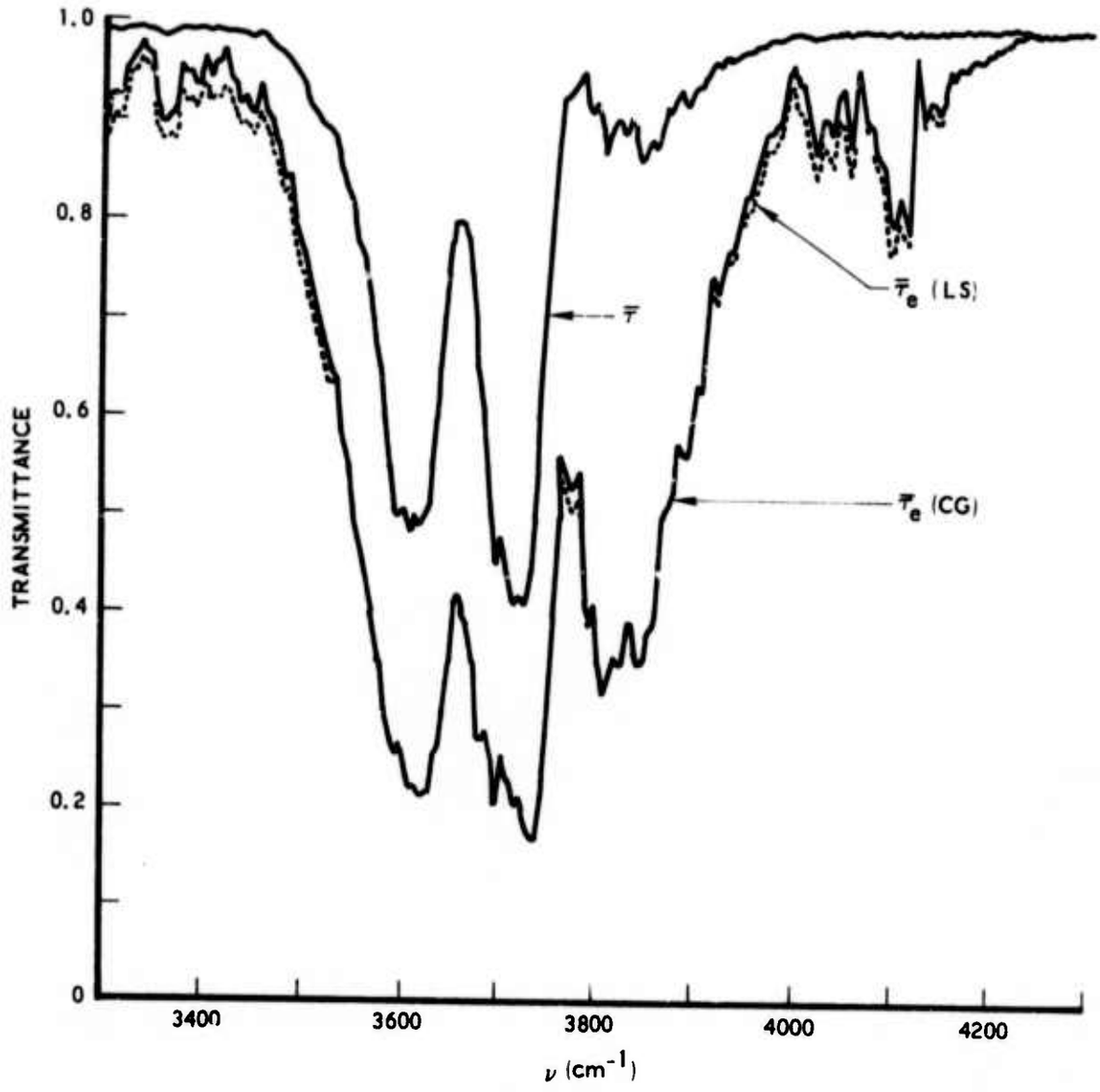

Fig. 19. Band Model Transmittance Results for Slant Path Using LINAVE2 Parameters

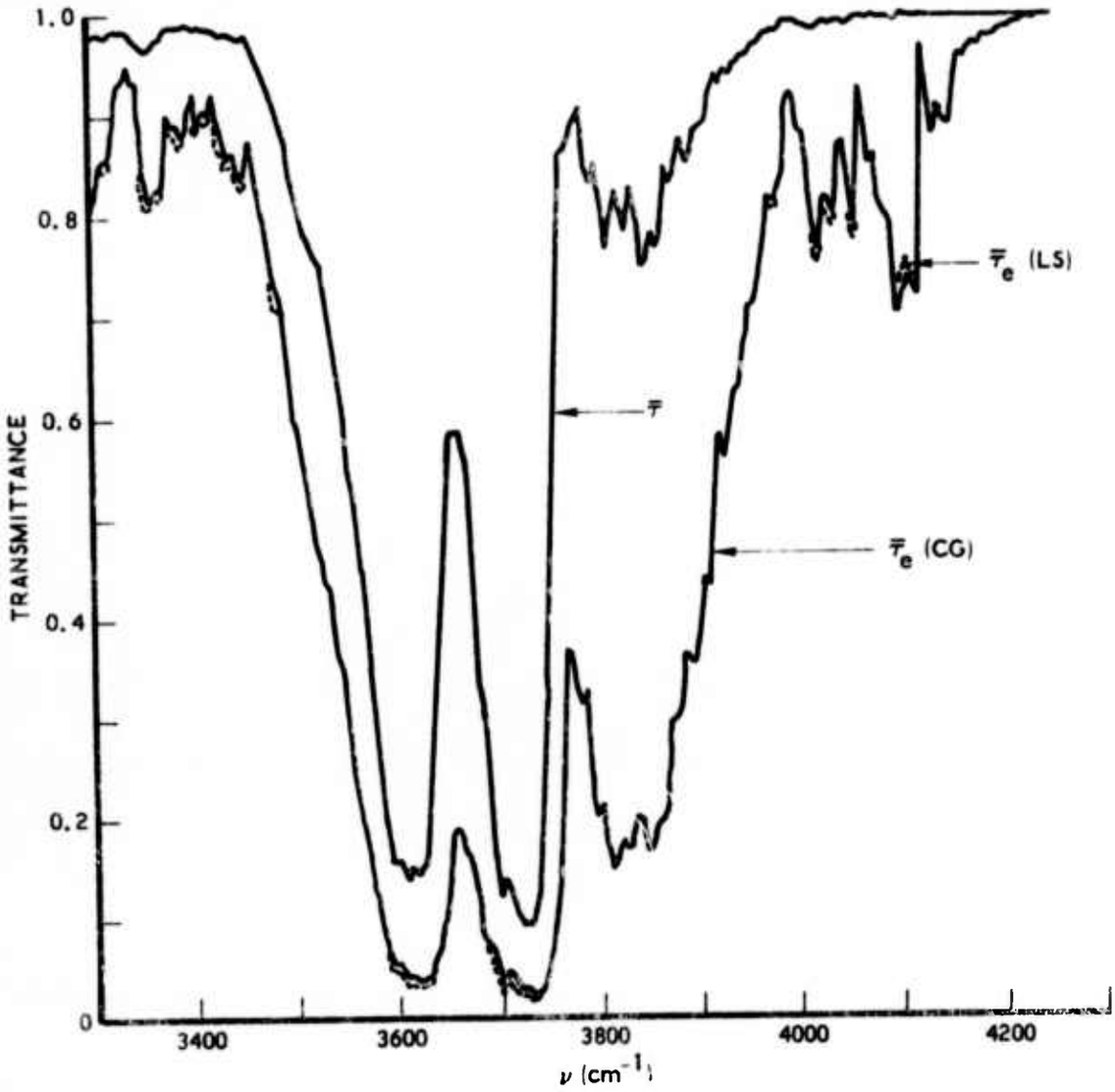

Fig. 20. Band Model Transmittance Results for Horizontal Path Using LINAVE2 Parameters

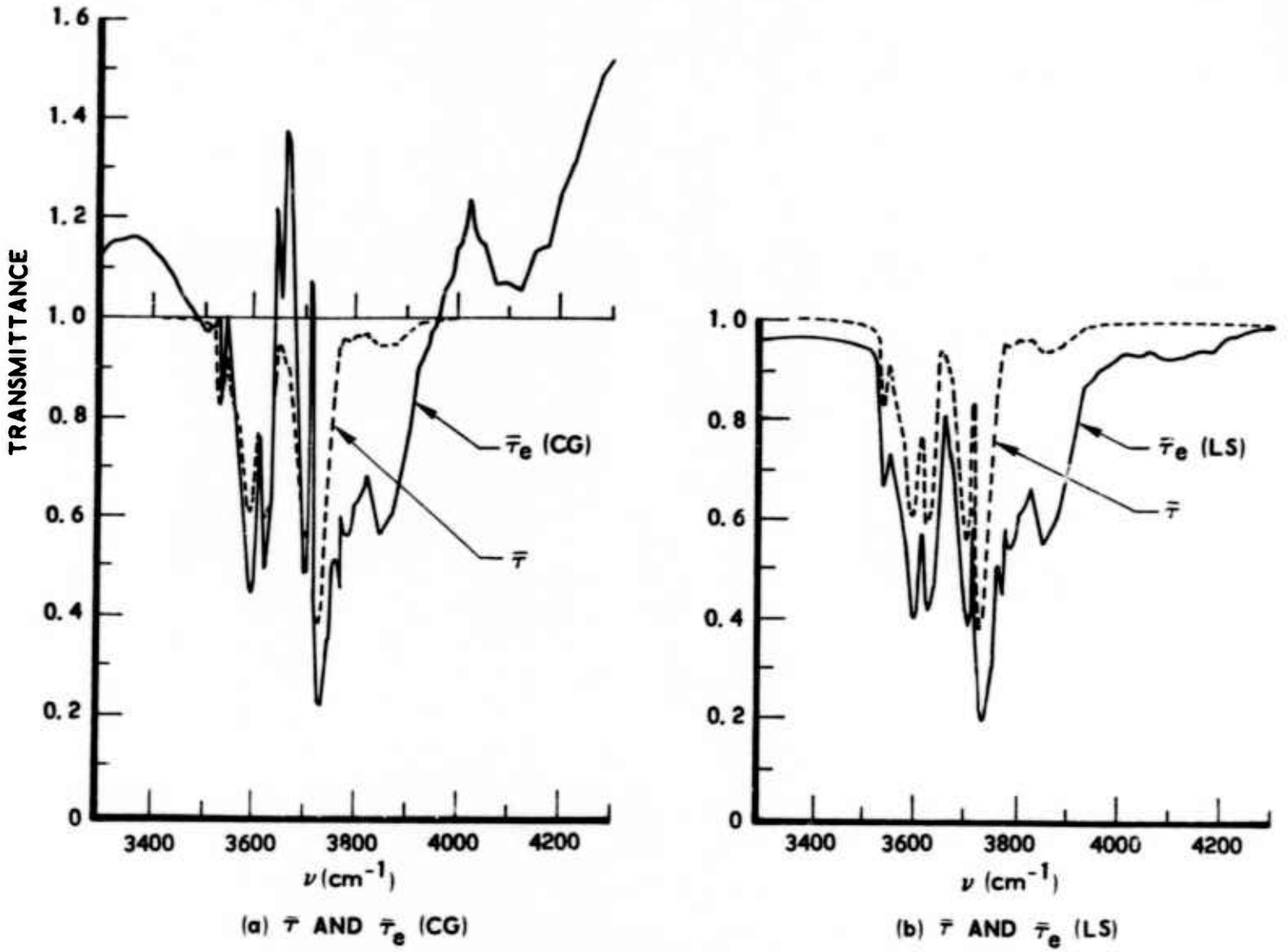

Fig. 21. Band Model Transmittance Results for Slant Path Using General Dynamics Parameters

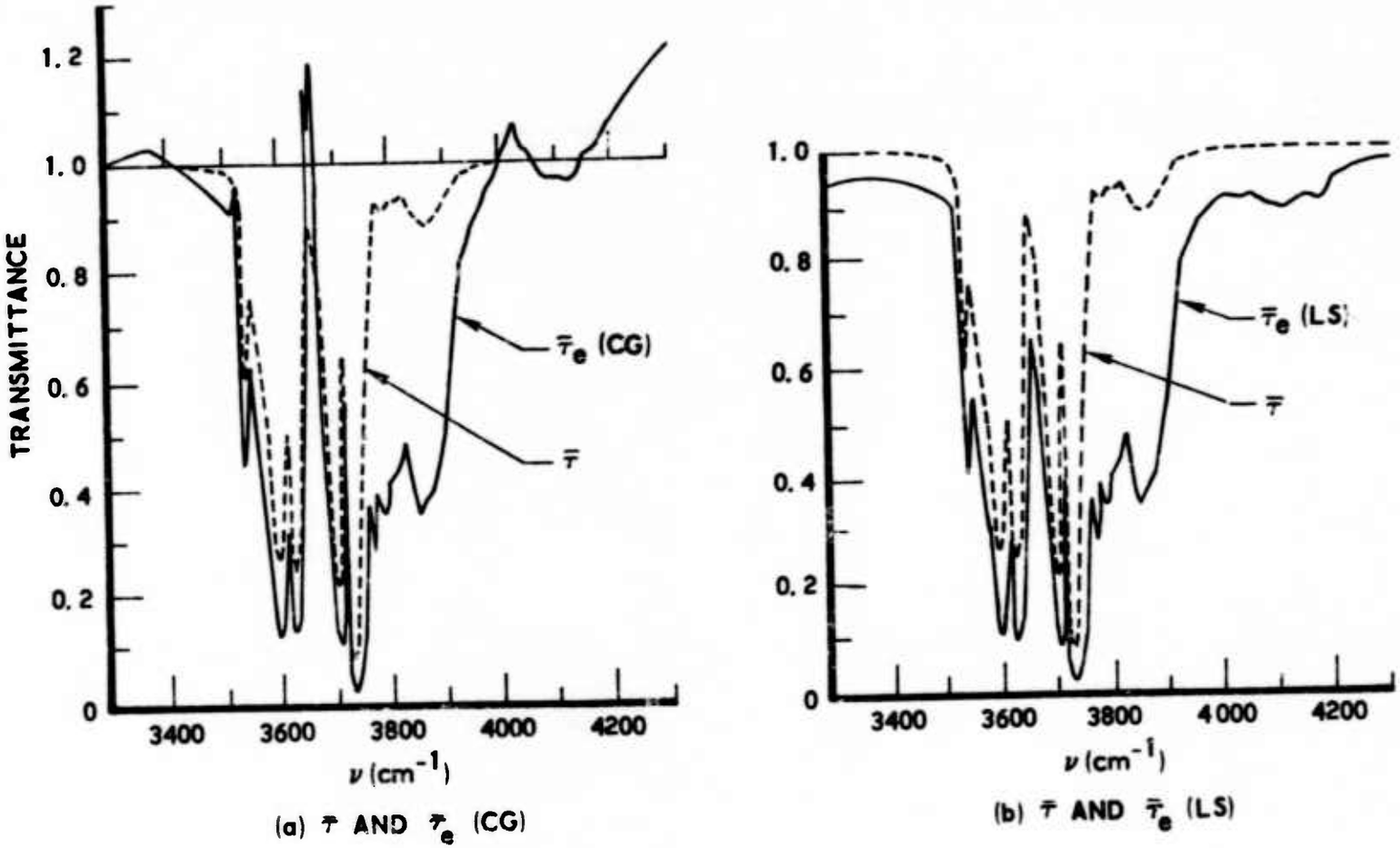

Fig. 22. Band Model Transmittance Results for Horizontal Path Using General Dynamics Parameters

the condition for which the CG approximation was predicted (paragraph II. D) to fail most noticeably.

A comparison of the band model and line-by-line results for $\bar{\tau}_e$ is given in Fig. 23 for the slant path and Fig. 24 for the horizontal path. The agreement is not quite so good as that obtained for $\bar{\tau}$ although the reasons for the discrepancies are probably the same.

The results described so far pertain to a single line of sight that passes perpendicularly through a diameter position of the equivalent homogeneous cylindrical plume. Application of transmittance results to the analysis of data from real systems, however, would, in many cases, require the average results for the effects of the entire plume. For the cylindrical plume being considered, there is no axial variation of the plume properties and the average effect of the whole source can be obtained by an analysis of the effects caused by moving the line of sight off the diameter position. Since the temperature and species concentrations are also homogeneous, the net result of this variation is to shorten the length of the hot source path. Results of such an off-axis variation at $\nu = 3700\ cm^{-1}$ for the slant path viewing geometry are given in Fig. 25. The effect of displacing the line of sight off axis (decreasing the source path length) is to make $\bar{\tau}_e$ smaller; the value of $\bar{\tau}_e$ at the diameter position is 0.205 while near the edge its value is only 0.100. The average transmittance of the atmosphere to the entire source is 0.190, which is a difference of only about 6 percent from the value for the diameter position alone. The transmittance value for the atmosphere alone ($\bar{\tau}$) is 0.456. It is evident from this result that the effects of line correlation between emitter and absorber become more important as the source becomes more optically thin. This tendency is consistent in that, as the optical depth of the source is increased, line broadening and overlap would cause the source radiation to become more and more continuum in nature and $\bar{\tau}_e$ would approach $\bar{\tau}$.

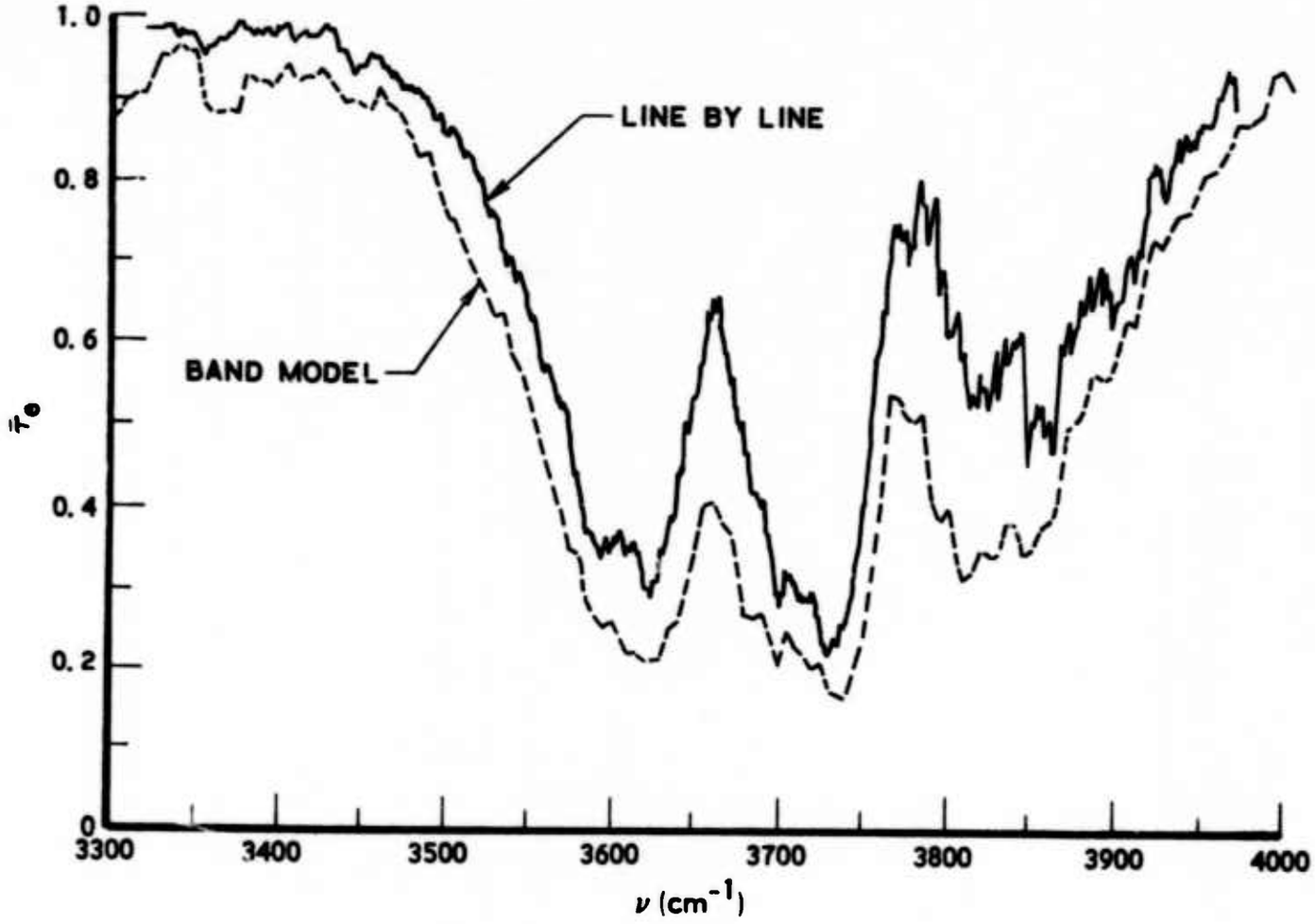

Fig. 23. Band Model and Line-by-Line $\bar{\tau}_e$ Results for Slant Path

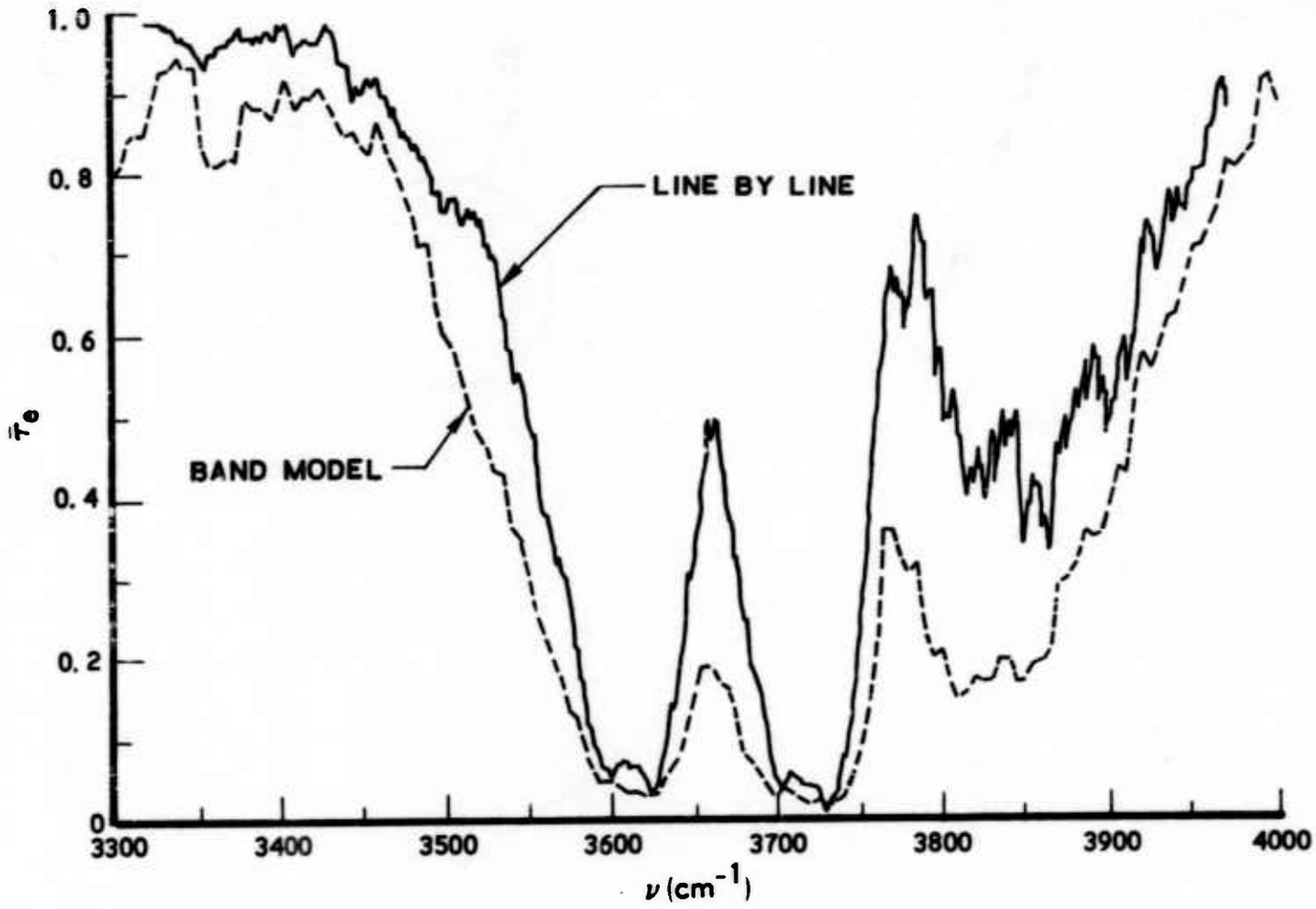

Fig. 24. Band Model and Line-by-Line $\bar{\tau}_e$ Results for Horizontal Path

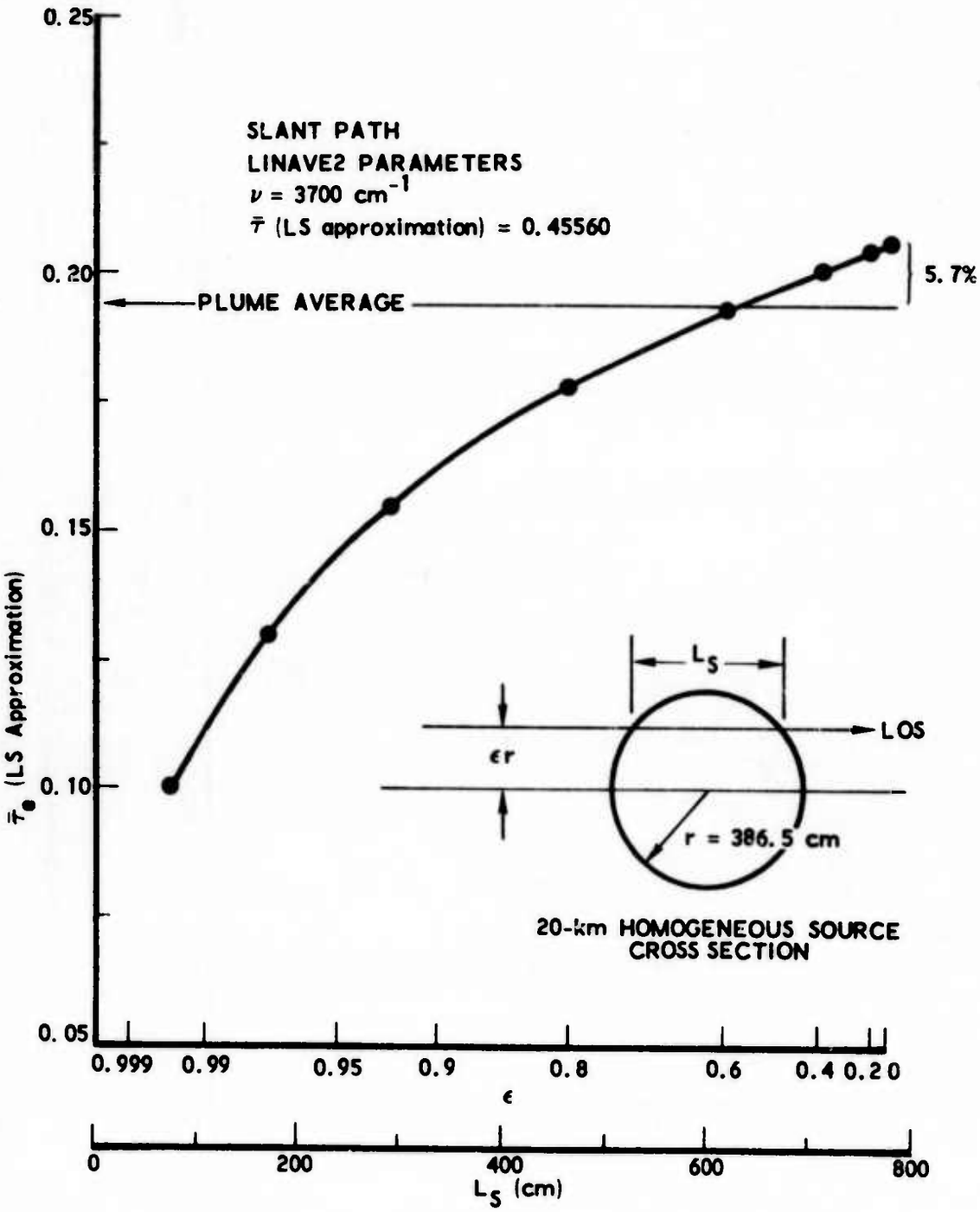

Fig. 25. Variation of $\bar{\tau}_e$ for Off-Axis Variation of Line of Sight through Cylindrical Plume

The effect of line correlation on the transmittance appropriate to wide spectral bandpasses was determined for both the slant and horizontal paths. The 2.7-μm spectral region was divided (somewhat arbitrarily) into three relatively distinct subregions. The bandpass between 3350 and 3575 cm^{-1} represents the low wave number band wing, the bandpass between 3575 and 3725 cm^{-1} represents the band center, and the bandpass between 3725 and 3950 cm^{-1} represents the high wave number band wing. In each of these bandpasses, the average values of $\bar{\tau}$ and $\bar{\tau}_e$ were computed from

$$T = \frac{1}{\nu_2 - \nu_1} \int_{\nu_1}^{\nu_2} \bar{\tau}(\nu)\, d\nu$$

and

$$T_e = \int_{\nu_1}^{\nu_2} R_{sensor}(\nu)\, d\nu \Big/ \int_{\nu_1}^{\nu_2} R_{source}(\nu)\, d\nu$$

respectively. The integration limits ν_1 and ν_2 are the lower and upper wave number values for the bandpass respectively, and R_{sensor} and R_{source} are the sensor and source radiance spectra respectively. For continuum emitters, the expression for T_e reduces to that for T if R_{source} does not vary much with ν between ν_1 and ν_2. The results for T and T_e along with the ratio T/T_e are listed in Table 8. For both the slant and horizontal paths, the largest discrepancy between T and T_e occurs in the band center region although the effect is nearly as great in the high wave number region. In the latter region, the emission/transmission phenomena are controlled almost exclusively by the H_2O content of the optical path, and, although the absolute amount of water vapor in either of the paths is small, the effect of line correlation is pronounced (e.g., a factor of nearly 3 for the horizontal path).

Table 8. Results for Average Transmittance in Selected Bandpasses of the 2.7-μm Atmospheric Absorption Band

$\nu_1 \rightarrow \nu_2$ (cm^{-1})	SLANT PATH			HORIZONTAL PATH		
	T	T_e	T/T_e	T	T_e	T/T_e
3350 - 3575	0.9377	0.7534	1.245	0.8666	0.6324	1.370
3575 - 3725	0.5832	0.2745	2.125	0.2695	0.08103	3.326
3725 - 3950	0.8704	0.4321	2.014	0.7693	0.2602	2.957

SLANT PATH = 20 km → SPACE, $\theta = 75^\circ$

HORIZONTAL PATH = 100-km LENGTH AT 20-km ALTITUDE

C. INTEGRAL CONVERGENCE CRITERIA

The radiance and transmittance calculations for atmospheric paths presented in this report rely on a numerical integration over both the atmospheric portion and the source portion of the total optical path. The principal integrations required are those necessary to compute the path-averaged variables x_e and β_e [Eqs. (16) and (17) respectively] , the transmittance $\bar{\tau}_i$ in the LS approximation [Eq. (26)] , and the radiance $\bar{L}$[Eq. (7)] for both the source path and the total path. All of these integrations are performed using a modified Simpson integration routine. The principal variable contributing to the accuracy of the integrations is the number N of intervals into which the integration path is divided. Present calculations have been executed by dividing the integration paths into equal size geometric intervals. The general criterion for computational accuracy is that the size of the integration interval Δs should be smaller than or of about the same magnitude as the scale length for significant change in the variables being integrated.

The calculations for x_e and β_e require evaluation of the two integrals

$$I_1(s) = \int_0^s \bar{k}(s')\, c(s')\, p(s')\, ds'$$

$$I_2(s) = \int_0^s \bar{k}(s')\, c(s')\, p(s')\, \beta(s')\, ds'$$

If the atmosphere is approximated as plane-parallel, isothermal, and exponential and if β is written as $\beta = \beta_0 p$, then

$$I_1(s) = \bar{k}\, p_1 \int_0^s c(s')\, e^{-s' \cos\theta/h}\, ds'$$

$$I_2(s) = \bar{k}\,\beta_0 p_1^2 \int_0^s c(s')\, e^{-2s' \cos\theta/h}\, ds'$$

where p_1 is the pressure at $s = 0$, θ is the zenith angle to the positive s direction, and h is the exponential scale height. For the case where c(s) is nearly constant (e.g., for CO_2), the scale lengths for significant variations of the integrands of I_1 and I_2 are h secθ and (h/2) secθ respectively. In order to satisfy the more stringent of the two convergence criteria implied, the condition $\Delta s \lesssim (h/2)\sec\theta$ should be met. The path length in a plane parallel atmosphere between altitudes z_1 and z_2 ($z_2 \geq z_1$) is simply $S = (z_2 - z_1)\sec\theta$. The number of intervals into which the path should be divided to satisfy $\Delta s \lesssim (h/2)\sec\theta$ is thus

$$N \gtrsim \frac{2(z_2 - z_1)}{h}$$

For most of the calculations presented here, the atmosphere is assumed to end at an altitude of 100 km. For the 75-deg zenith angle path originating at z = 20 km, then, N should be greater than about 25 if a scale height of $h \simeq 6.5$ km is assumed.

For the case where c(s) is not constant, a scale length can still be estimated by approximating c(s) in an exponential form. For example, in the first 12 km of the tropical model atmosphere of McClatchey et al.,[7] c(s) for H_2O can be approximated as

$$c_{H_2O}(z) \simeq c_{H_2O}(0)\, e^{-z/2.17\ \text{km}}$$

Thus, the scale length for the integrand of I_2 becomes $(2/h + 1/2.17\ \text{km})^{-1}$ secθ. For slant paths originating near ground level ($z_1 \simeq 0$), the scale

length then is about 1.3 km and N should be greater than about 77. More rapid variations in c_{H_2O} are sometimes present at higher altitudes, but the absolute value of c_{H_2O} is so low that little error can result by not integrating through these regions with the required interval size. For horizontal (θ = 90 deg) atmospheric paths, the scale lengths become infinite and imply that no integration is necessary.

Integration of Eqs. (26) and (7) involves spatial variation of the transmittance derivative. The local scale length for variation of this parameter is $(\bar{k}\ c\ p)^{-1}$. For atmospheric paths, $\bar{k}$ can change greatly with wave number, and c and p can again change with path position. A worst case estimate of the required number of intervals required for an accurate integration can be obtained by computing the largest value of $\bar{k}\ c\ p$ occurring along a path. For slant paths, this occurs at the lower altitude level where p is largest (and usually c also) and for the spectral position of strongest absorption. For example, for the 75-deg slant path originating at 20 km, the conditions for CO_2 absorption are $p \simeq 0.0558$ atm, $c_{CO_2} \simeq 0.00033$, $\bar{k}$ (207°K, 3700 cm^{-1}) $\simeq 1.10\ cm^{-1}$/atm so that $(\bar{k}\ c\ p)^{-1} \simeq 0.49$ km. Thus, the number of intervals should be about 160. For the 100-km-long horizontal path situated at 20-km altitude, N should be greater than 200. The value of N = 160 for the slant path is a worst case estimate, while the value of N = 200 for the horizontal path is near accurate.

The actual convergences displayed by numerical calculations using ATLES are presented in Figs. 26 and 27 for the slant and horizontal paths considered thus far. For these calculations, values of N for the atmospheric path (NAPATH) of 10, 20, 30, 50, 100, 150, and 200 (the limit of the computer program) were used. For the source portion of the path, N was held constant at NSPATH = 30. This value of NSPATH is easily sufficient to provide less than 1 percent accuracy for calculations within the source. For the slant path (Fig. 26), both $\bar{\tau}$ and $\bar{\tau}_e$ are seen to converge at NAPATH $\simeq$ 30. This value is about what would be expected on the basis of

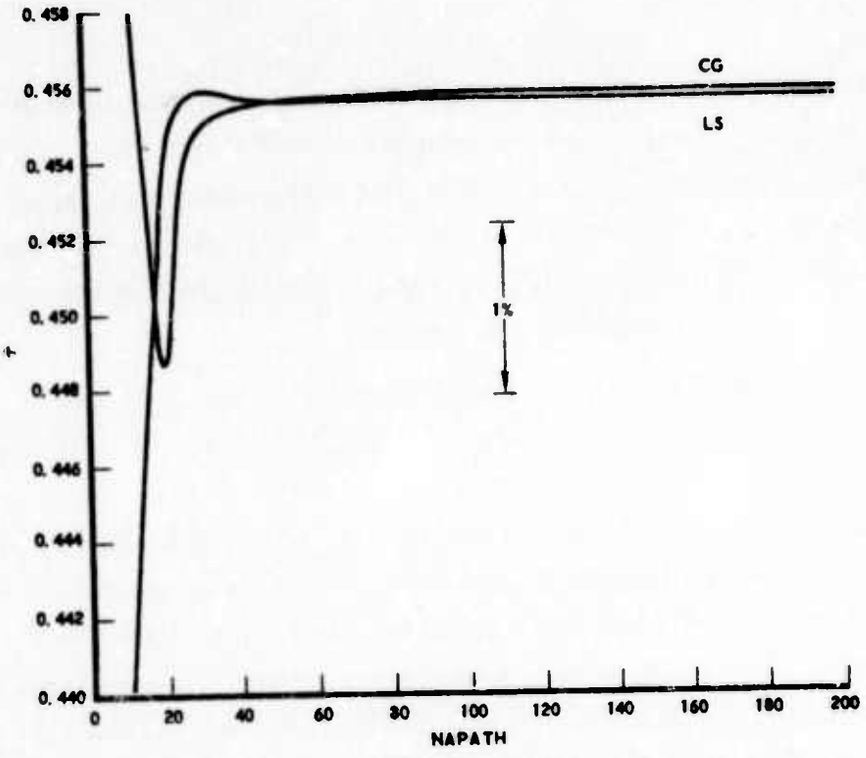

(a) CONVERGENCE OF $\bar{\tau}$

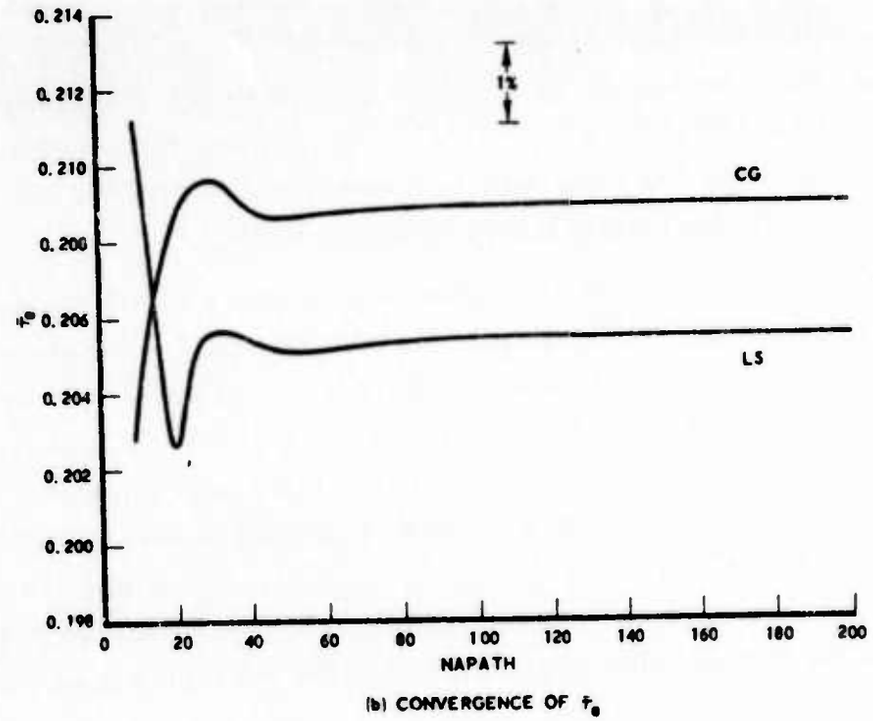

(b) CONVERGENCE OF $\bar{\tau}_\theta$

Fig. 26. Transmittance Convergence for Slant Path

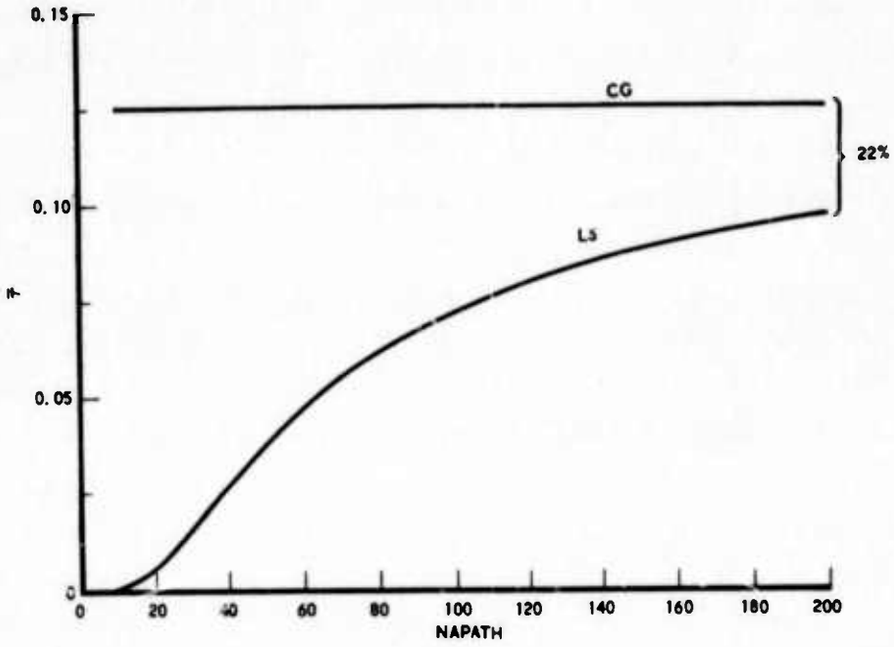

(a) CONVERGENCE OF $\bar{\tau}$

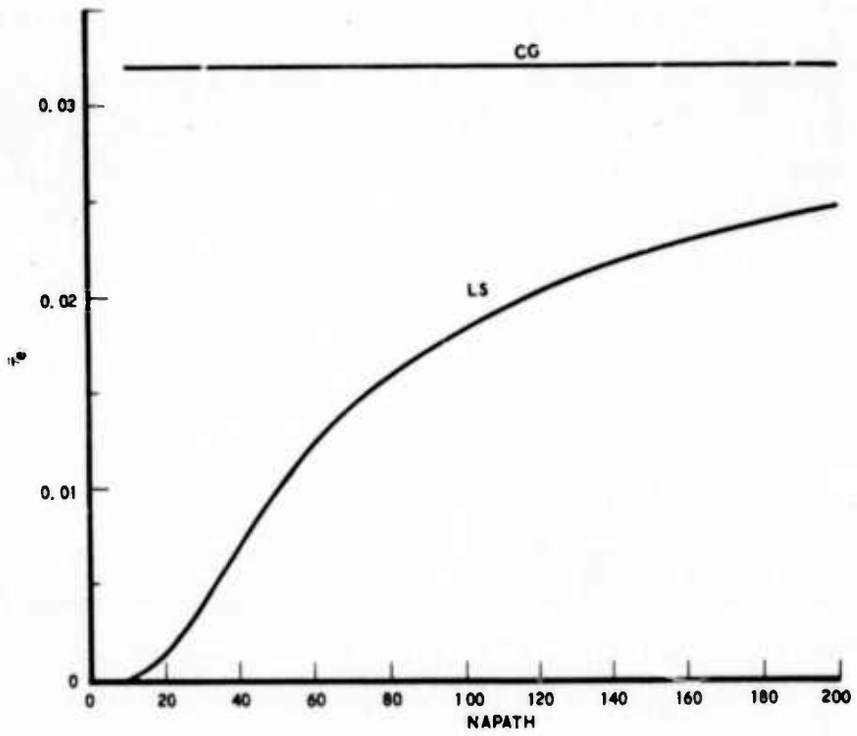

(b) CONVERGENCE OF $\bar{\tau}_\theta$

Fig. 27. Transmittance Convergence for Horizontal Path

the criterion required for the calculation of x_e and β_e (~25), but is much less than that estimated for the convergence of the radiance and transmittance equations (~160). This result confirms the worst case nature of the estimate. For the horizontal path, a quite different convergence characteristic is evident (Fig. 27). The results for $\bar{\tau}$ and $\bar{\tau}_e$ using the CG approximation are accurate for even the smallest NAPATH value used (NAPATH = 5) while the results, at least for $\bar{\tau}$, using the LS approximation are still in error by more than 20 percent at the largest value of NAPATH used (NAPATH = 200). These results are explainable with the estimations presented earlier. For a horizontal path, little consideration has to be given to the convergence of x_e and β_e since the path is nearly homogeneous and the evaluation of these parameters simply involves multiplication. Also, in the CG approximation, the transmittance is given by an analytical function [Eq. (18)] so that no integration is involved here either. Only for the numerical calculation of the transmittance in the LS approximation [Eq. (26)] is an integration involved. The previous estimate for this integration to be accurate at 3700 cm^{-1} was in fact NAPATH > 200. Thus, the estimation technique is confirmed.

A serious problem is presented here. For calculations over very long, nearly horizontal atmospheric paths within the LS approximation, the number of intervals into which the path should be divided to obtain accurate results may be prohibitively large. The solution used in the present work has been to dispense with the calculation of the strictly atmospheric transmittance properties in the LS approximation and use only the results of the CG approximation. This can be done with quite good accuracy since the degree of inhomogeneity of the atmosphere is not too large to be handled adequately by the CG approximation. Results obtained for various atmospheric paths in both the CG and LS approximations (and under conditions where the results of the latter approximation were confirmed to be accurate) have never shown a difference of more than 1 percent between the two approximations. Calculations using the LS approximation have been excluded

when necessary in the computation of strictly atmospheric radiance/transmittance results, but the approximation is always retained for computations involving the whole (atmosphere plus hot source) optical path.

VI. SUMMARY

A. SUMMARY OF PRESENT WORK

A band model formulation designed for computing the effective transmittance of the atmosphere to hot H_2O/CO_2 plume emission sources has been presented and discussed in detail. This model is formulated within the confines of the statistical band model for a random array of pressure-broadened Lorentzian lines of equal strength and width. The effects of line correlation between the plume emission spectrum and the atmospheric H_2O/CO_2 absorption spectrum are accounted for by treating the entire optical path extending from the sensor position through the intervening atmosphere and including the hot emission source as a single radiating/absorbing entity. The high degree of inhomogeneity and non-isothermality of such an optical path are accounted for by either the Curtis-Godson or Lindquist-Simmons approximation. In addition, the inhomogeneity conditions for which the Curtis-Godson approximation is likely to fail are determined. Procedures are presented for the efficient application of the Lindquist-Simmons approximation (which does not display the faults of the Curtis-Godson approximation).

Calculations within this formulation and appropriate to the viewing geometries of satellite surveillance systems and aircraft-to-aircraft field measurements programs have been performed. For selected wide spectral bandpass regions, the effect of line correlation is shown to result in discrepancies of as much as a factor of 3 between currently calculated and correctly calculated average transmittance values.

B. FUTURE WORK AREAS

The course of the present work has indicated three general areas in which future work would be highly desirable. The first area concerns the band model formulation itself. This model was developed within the

statistical band model of equal-strength Lorentzian lines primarily so that the Lindquist-Simmons approximation, as developed by Lindquist and Simmons[3], could be incorporated directly. Although the statistical model is applicable to the consideration of absorption by H_2O, its application to CO_2 may not be as accurate as the application of a regular-line band model. Work on the development of an approximation analogous to the Lindquist-Simmons approximation but applicable to band models other than the statistical model for equal-intensity Lorentzian lines is thus indicated. A generalization to line shapes other than simple Lorentzian would also be highly desirable.

The second area concerns the band model parameters $\bar{k}$ and β_0 used with the band model. Adequate band model parameter sets exist for the high-temperature regions applicable to combustion gas plumes and for the low-temperature regions applicable to atmospheric absorption paths. If the problem of atmospheric transmittance could be treated in a manner in which the source emission and atmospheric absorption were discoupled processes, these existing parameter sets would be all that is needed to handle the transmittance calculations. Correct computation, however, requires the entire optical path to be treated as a coupled system. Thus, a consistent set of band model parameters applicable to the entire temperature range from atmospheric temperatures to combustion gas temperatures is required. Here, the term "consistent" implies not only that a realistic temperature variation for $\bar{k}$ and β_0 be found, but also that these parameters have the same meaning at all temperatures. For example, $\bar{k}$ and β_0 derived from the AFCRL line compilation have explicit meanings by virtue of their specific defining equations (Eqs. [43] and [50] respectively). They are, respectively, the mean absorption coefficient in $\Delta\nu$ and the mean line width to spacing ratio in $\Delta\nu$ (for nonresonant self-broadening). The quantities from the General Dynamics tabulation, at least for H_2O, which bear the same symbolic names are, however, simply empirically measured constants which best fit the band model representation chosen to analyze the data,

although the correspondence of the General Dynamics $\bar{k}$ to the mean absorption coefficient and the General Dynamics β_0 to the mean-line-width-to-spacing ratio is probably quite close. The fact remains that a set of experimentally derived $\bar{k}$ and β_0 values can yield highly accurate transmittance results and yet not correspond to their intuitive physical meaning. Hence, the generation of consistent band model parameter sets for H_2O and CO_2 that cover the entire temperature range required for the calculations of atmospheric transmittances to hot gas emission sources should be given serious consideration.

The third general area is simply one of completeness. The present work has considered only the emission/absorption effects of CO_2 and H_2O within both the source and the absorbing atmosphere. The effects of radiation and absorption by minor molecular constituents as well as the effects of particulate emission in the source (e.g., carbon) and particulate extinction (absorption or scattering) in the atmosphere should be included to give a more complete description of the problem. Consideration of background signals (e.g., earth, sky, and missile engine hot parts) should also be undertaken

LABORATORY OPERATIONS

The Laboratory Operations of The Aerospace Corporation is conducting experimental and theoretical investigations necessary for the evaluation and application of scientific advances to new military concepts and systems. Versatility and flexibility have been developed to a high degree by the laboratory personnel in dealing with the many problems encountered in the nation's rapidly developing space and missile systems. Expertise in the latest scientific developments is vital to the accomplishment of tasks related to these problems. The laboratories that contribute to this research are:

Aerophysics Laboratory: Launch and reentry aerodynamics, heat transfer, reentry physics, chemical kinetics, structural mechanics, flight dynamics, atmospheric pollution, and high-power gas lasers.

Chemistry and Physics Laboratory: Atmospheric reactions and atmospheric optics, chemical reactions in polluted atmospheres, chemical reactions of excited species in rocket plumes, chemical thermodynamics, plasma and laser-induced reactions, laser chemistry, propulsion chemistry, space vacuum and radiation effects on materials, lubrication and surface phenomena, photosensitive materials and sensors, high precision laser ranging, and the application of physics and chemistry to problems of law enforcement and biomedicine.

Electronics Research Laboratory: Electromagnetic theory, devices, and propagation phenomena, including plasma electromagnetics; quantum electronics, lasers, and electro-optics; communication sciences, applied electronics, semiconducting, superconducting, and crystal device physics, optical and acoustical imaging; atmospheric pollution; millimeter wave and far-infrared technology.

Materials Sciences Laboratory: Development of new materials; metal matrix composites and new forms of carbon; test and evaluation of graphite and ceramics in reentry; spacecraft materials and electronic components in nuclear weapons environment; application of fracture mechanics to stress corrosion and fatigue-induced fractures in structural metals.

Space Physics Laboratory: Atmospheric and ionospheric physics, radiation from the atmosphere, density and composition of the atmosphere, aurorae and airglow; magnetospheric physics, cosmic rays, generation and propagation of plasma waves in the magnetosphere; solar physics, studies of solar magnetic fields; space astronomy, x-ray astronomy; the effects of nuclear explosions, magnetic storms, and solar activity on the earth's atmosphere, ionosphere, and magnetosphere; the effects of optical, electromagnetic, and particulate radiations in space on space systems.

THE AEROSPACE CORPORATION
El Segundo, California